

CHARACTERIZATION OF THE IMPULSIVE JET  
PRODUCED FROM A DOLPHIN'S BLOWHOLE

By

CJ BARTON

Bachelor of Science in Mechanical Engineering

University of Tulsa

Stillwater, OK

2018

Submitted to the Faculty of the  
Graduate College of the  
Oklahoma State University  
in partial fulfillment of  
the requirements for  
the Degree of  
MASTER OF SCIENCE  
December, 2020

CHARACTERIZATION OF THE IMPULSIVE JET PRODUCED FROM A  
DOLPHIN'S BLOWHOLE

Thesis Approved:

Dr. R. J. Gaeta

---

Thesis Adviser

Dr. Jamey Jacob

---

Dr. Arvind Santhanakrishnan

---

Dr. Jason Bruck

---

Name: CJ BARTON

Date of Degree: DECEMBER, 2020

Title of Study: CHARACTERIZATION OF THE IMPULSIVE JET PRODUCED  
FROM A DOLPHIN'S BLOWHOLE

Major Field: MECHANICAL AND AEROSPACE ENGINEERING

Abstract: The health of bottlenose dolphins can be monitored by marine biologists through the analysis of their exhaled breath. Unique concepts to capture this breath in the wild include flying an Unmanned Aerial System (UAS) through this exhaled breath to capture the key hormone cortisol. The breath is multiphase by nature, consisting of unknown quantities of particles (e.g., mucus, water) and air. In order to help design such a UAS, a multi-phase jet is designed to simulate a dolphin's breath through its blowhole, which has been established in the literature to be 20-140 liters/s in 0.26-0.31 seconds. A 3D printed replication of dolphin's nasal passage is made using a CT Scan of a real dolphin to more accurately produce the resulting flow field, or "blowfield". This paper details the fluid dynamic characterization of this blowfield. Measurements of the blowfield's plume evolution with high-speed photography, instantaneous velocity with Particle Image Velocimetry (PIV) and with high frequency response pressure sensors are made. The three-dimensional nature of the jet is quantified with velocity (via pressure) measurements and the high-speed photography. These data qualitatively show the extent above the blow hole the solid particles and air reach. This is helpful data for the design of a special UAS needed to capture the cortisol. Finally, integration of the velocity field near the blowhole exit is used to determine the momentum flux. These data are compared to existing data of real dolphins where flow rates were measured, and In-Situ PIV measurements were made. The impulsively started round conventional nozzle follows characteristics similar to steady jets while the dolphin nasal passage shares trends from well-mixed nozzles. The simulator is shown to produce nominal exhaled dolphin flow rates and will be used for future work to simulate the exhaled breath of a dolphin that is swimming, resulting in a jet in cross flow.

## TABLE OF CONTENTS

Chapter	Page
I. INTRODUCTION.....	1
Motivation.....	2
Existing Flow Rate Data.....	3
Initial In-Situ Data of Dolphin Chuff Blowfield.....	3
Blowhole Simulator.....	4
Research Questions.....	5
Study Overview.....	6
II. LITERATURE REVIEW.....	7
Classification of Jets.....	7
Volumetric Flux.....	8
Momentum Flux.....	9
Impulsively Started Jets.....	10
Multiphase-flow.....	13
Qualitative Characteristics of Jets in Cross Flows.....	18
Jet Penetration into Cross Flows.....	19
III. EXPERIMENTAL METHODS.....	23
Design & Manufacturing of ChuffSim.....	23
Data Acquisition of ChuffSim.....	25
Pressure & Velocity Measurements.....	25
Converting Pressure to Velocity.....	27
Turbulence Intensity.....	27
Blowfield Self-Similarity.....	30
Pressure Measurement Technique.....	31
Jet Centerline Measurements.....	34
Flow Visualization/Instantaneous Velocity with PIV.....	35
Dolphin In-Situ PIV.....	37
Laboratory Flow Visualization.....	41
Blowfield Splatter Test.....	41

Chapter	Page
IV. RESULTS & DISCUSSION .....	43
Velocity Data .....	43
Turbulence Intensity Data.....	50
Self-Similarity Plots.....	54
ChuffSim PIV Data.....	55
Flow Visualization .....	57
Blowfield Splatter Results .....	60
Comparison of Respiratory Data .....	63
Results from Bermuda In-Situ PIV .....	66
Jet Penetration in Cross Flow .....	70
V. CONCLUSION.....	72
Answering Research Questions .....	72
Limitations .....	73
Future Work and Recommendations .....	73
REFERENCES .....	75
APPENDICES .....	78
APPENDIX A.....	79
APPENDIX B .....	82
APPENDIX C .....	84
APPENDIX D.....	87
APPENDIX E .....	88
APPENDIX F.....	89

## LIST OF TABLES

Table	Page
F1. Expanded Uncertainties for a 95% Confidence Interval .....	89

## LIST OF FIGURES

Figure	Page
1. UAS Capturing Blow from Dolphin .....	2
2. Table of Respiratory Specifications .....	3
3. a/b: Blowhole Simulator .....	4
4. a/b: DNPN Relation to Dolphin Head Schematic & CT Scan .....	5&17
5. Anatomy of a Jet .....	7
6. a/b: ZNMF Jet (a) versus Continuous Jet (b) .....	10
7. Normalized Profiles of Axial Velocity @ $x/D = 60$ .....	11
8. Laser Induced Fluorescence Images of Impulsively Started Jets .....	13
9. a/b/c: Human Respiratory Flow Visualization .....	14
10. Visualization of the Turbulent Round Starting and Interrupted Jets .....	15
11. Time Resolved Sneeze Evolution .....	16
12. Mean Flow for an Incompressible Transverse Jet .....	18
13. Evolution of out-of-plane velocity into CVP .....	19
14. Predicted Trajectories for Jets Penetrating into a Circular Cylinder .....	21
15. ChuffSim CAD Assembly with Labels .....	24
16. Integration of CT Scan into ChuffSim .....	24
17. 3D Printed Round Conventional Nozzle & Dolphin Nasal Passage .....	25
18. Pitot Tube Calibration Apparatus .....	26
19. Laminar versus Turbulent Flow Regimes .....	28
20. Example of a Free Shear Layer in a Jet .....	30
21. DNPN Centerline Velocity Trace @ $x/D = 0$ .....	31
22. Pressure Transducer Grid-Survey Apparatus .....	32
23. Coordinate System for Grid-Survey .....	32
24. Grid-Survey Methodology with Velocity Profile Example .....	34
25. a/b: Calculated Flow Rate & Velocity Uncertainty .....	35
26. PIV Acquisition Set Up .....	37
27. Top View of Dolphin Quest Dockyard .....	38
28. Dolphin Quest Bermuda Dockyard .....	38
29. Dock-Side PIV Set Up .....	39
30. In-Situ PIV Field of View from Caliban @ 4500 fps .....	40
31. Splatter Test Example .....	42
32. Control Nozzle vs Dolphin Nasal Passage Velocity Evolution, $x/D = 0-4$ .....	44
33. Normalized Velocity Decay vs $x/D$ .....	45
34. Normalized $x/D$ vs Normalized $y/D$ .....	47

Figure	Page
35. Detailed View of DNPN Orifice.....	48
36. Dolphin Blowhole Shape.....	48
37. DNPN SolidWorks CAD with Free-Handed Flow Vectors .....	49
38. a/b: Mean Velocity in Potential Core vs. Mean Velocity in Shear Layer.....	50
39. a/b: Z-plane Turbulence Intensity plots for RCN & DNPN @ x/D=3 .....	51
40: a/b: Y-plane Turbulence Intensity plots for RCN & DNPN @ x/D=3.....	52
41: Z-plane Self-Similarity plots for x/D=0-4 .....	53
42. Y-plane Self-Similarity plots for x/D=0-4 .....	54
43. DNPN Instantaneous PIV comparison to Averaged Unsteady Press. Transd. ....	55
44. RCN & DNPN Starboard-Side Extent.....	57
45. RCN & DNPN Head-Side Extent.....	58
46. RCN & DNPN Extent Larger FOV .....	59
47. Splatter Tests 4 feet above RCN & DNPN.....	60
48. Diameter Evolution versus x-axis for DNPN & RCN.....	61
49. Flow Rate Trace of Voluntary versus Maximal Respiratory Effort .....	62
50. Example of Velocity Trace from RCN Potential Core .....	63
51. DNPN Instantaneous Origin Flow Rate versus Time @ x/D=0 .....	64
52. RCN Instantaneous Origin Flow Rate versus Time @ x/D=0.....	64
53. Bermuda PIV Volumetric Flow Rate Plot .....	65
54. ChuffSim Averaged Velocity and Bermuda In-Situ PIV Comparison.....	67
55. Cross-Flow Illustration .....	69
56. Dolphin Chuff Blowing Researcher's Hair.....	70
57. Ymax/D vs. Momentum Flux Ratio for Jets in a Cross-Flow .....	71
A1. Labview Calibration and Logging Program.....	79
A2. Digital Pitot Tube Gauge Pressure vs. Endevco Pressure Transducer Voltage ..	80
B1. Endevco Pressure Transducer Size Specifications Sheet.....	82
B2. Endevco Pressure Transducer General Specification Sheet.....	83
C1. Voluntary & Forceful Exhalation Flow Rates.....	84
C2. Tidal Volume of Voluntary & Maximal Respiratory Efforts.....	85
C3. Pneumotachometer Apparatus and Test Set-up .....	86
D1. MATLAB PIVlab Measure Tool .....	87
E1. General Bermudian Dolphin Information .....	88
F1. Mathematica Code for Uncertainty in Velocity Calculation .....	90
F2. Piezo-Resistive Pressure Transducer Uncertainty in Calibration Method .....	92
F3. Mathematica Code for Uncertainty in Calibration .....	93



## CHAPTER I

### INTRODUCTION

Studying marine wildlife as land dwelling mammals can be difficult, especially while trying to mitigate our impact to the inhabitants of marine ecosystems. Such is the case with the field of marine biology where biologists are interested in monitoring wild dolphins stress levels, reproductive health, and overall well-being while mitigating the effects of handling. One solution is to design an unmanned aerial system (UAS) to capture hormone-laden mucus from dolphins' respiratory exhalations. In open ocean swimming, dolphins breach the surface of the water for a breath of fresh air through their blowholes. When this happens, the dolphin forcefully expels nearly all the contents of its lungs in roughly a quarter of a second before taking a fresh new breath [13]. The result is a violent multi-phase jet consisting of mucus, air, and sea water. This is referred to as a "chuff" where its contents are called "blow". The mucus in blow is what biologists hope to analyze to quantify the parameters named above. High stress-levels, similarly to humans, are attributed to high levels of cortisol that can be found in mucus samples. Data obtained from this study will help to build and design a UAS for biologists to quantify dolphin pods that contain high levels of cortisol and thus, improve the quality of life of marine mammals.

## *Motivation*

In order to gather data In-Situ from a dolphin's chuff in the open ocean, a UAS must be designed to collect blow samples without having an impact on the health of the dolphin. Thus, an understanding of what noise and visual stimuli will affect the animals is needed. Moreover, an understanding of the jet dynamics of the chuff is needed to help design a specialized UAS to collect the data. The development of the UAS is necessary to understand the motivation of this study, however, it is not within its scope. Before a concept of operations (CONOPs) can be developed for the UAS, a better understanding of the extent of Dolphins' chuff flow field or "blowfield" is necessary.

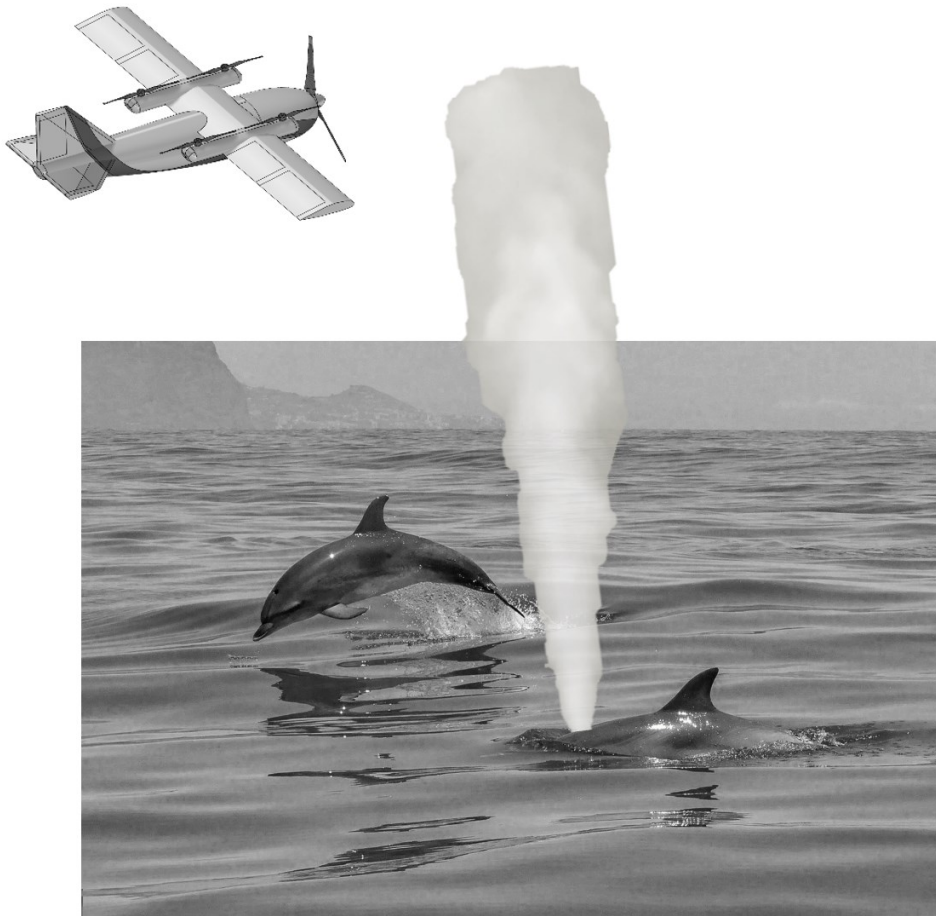


**Figure 1: UAS Capturing Blow from Dolphin [3]**

## Existing Flow Rate Data

In order to match the parameters of a dolphin's blowhole existing respiratory data was used as a benchmark for this current study. Fahlman et Al. (2017) presents data for dolphin lung flowrates and efflux times for various sea mammals [13]. Fahlman indicates that during a maximal respiratory effort (chuff) flowrates can reach up to 140 liters/seconds at a duration range of 0.26-0.31 seconds (efflux time). This is adequate for designing a system to simulate this phenomenon consistently. However, due to limited information in this field, validation of these figures is necessary.

Animal	Body mass (kg)	Length (cm)	Age (years)	Rest		Maximum respiratory flow (l s <sup>-1</sup> )		Irving et al., 1941; Ridgway et al. 1969; Fahlman et al	<i>n</i>
				<i>f<sub>R</sub></i> (breaths)	Respiratory duration (s)				
Atlantic bottlenose	140–250	5–10	3.4	0.26–0.31	0.43–0.66	20–140	15–33		
Hoku	182.5	252.0	12	3	0.857±0.103	0.695±0.148	0.80±0.08	9 (9)	
Kolohe	195.8	260.4	8	3	1.185±0.345	0.832±0.268	0.70±0.06	37 (29)	
Liho	158.4	237.5	18	2	0.892±0.131	0.589±0.044	0.67±0.15	12 (8)	
Liko	167.5	254.0	8	5	1.060±0.363	0.851±0.310	0.80±0.04	62 (12)	
Lono	249.5	273.1	6	3	0.970±0.387	0.777±0.266	0.81±0.04	24 (19)	
Nainoa	178.3	245.9	2	4	1.050±0.336	0.852±0.269	0.81±0.06	50 (36)	

Body mass, approximate age at time of study, number of metabolic measurements (*N*), oxygen consumption ( $\dot{V}_{O_2}$ ) and carbon dioxide production rates ( $\dot{V}_{CO_2}$ ), respiratory exchange ratio (RER), number of breaths analyzed (*n*), with the number of voluntary breaths in parentheses.

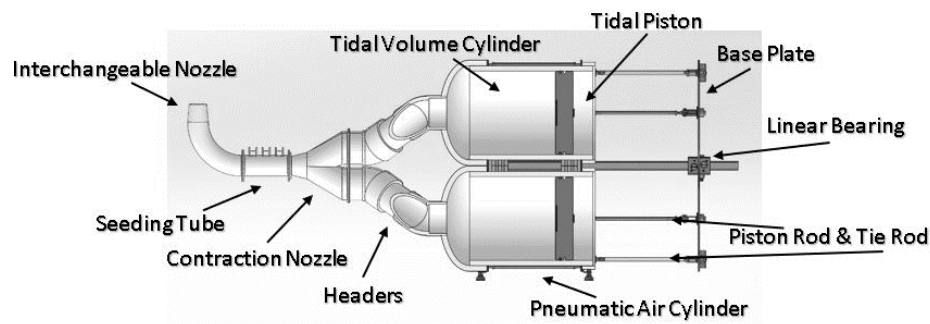
**Figure 2: Table of Respiratory Specifications [13]**

## Initial In-Situ Data of Dolphin Chuff Blowfield

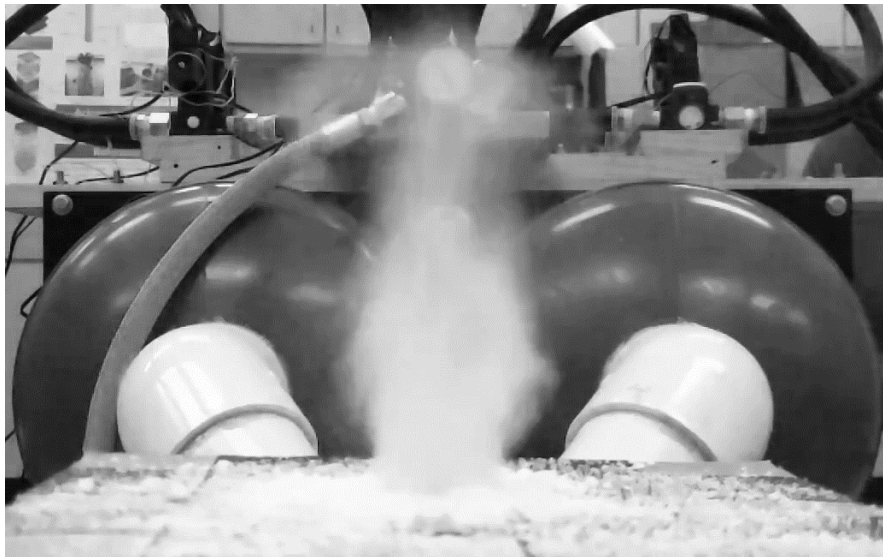
In an effort to support the existing flow rate data an interdisciplinary study was conducted with the help of biologists and engineers from Oklahoma State University. Data sets are obtained from dolphins in human care that participated in the study. Using Particle Image Velocimetry (PIV), flowrates from three dolphins of different age, weight, and size were approximated. Due to the difficulty of focusing on a plane in the flow structure and inconsistent seeding, the data sets were not adequately resolved. The raw data by itself is still useful since it gives unprecedented insight to the extent of dolphins' blowfield.

### Blowhole Simulator

To study the blowfield in a controlled manner, a consistent method for producing an impulsive jet was necessary. A simulator was designed and built, using the figures described from literature provided by Fahlman et Al. (2015), to be tested in a controlled environment [13]. The use of a simulator helps to ensure repeatability while mitigating the necessity of difficult In-Situ field research. The Dolphin Blowhole Simulator (*ChuffSim*) used for the present work is designed to achieve an impulsive maximum flowrate of ~140 liters/second. This was not achieved due to tolerance considerations and pipe resistance. However, the machine delivers an impulsive jet resembling a forceful breath that dolphins produce during exhalation.



(a)



(b)

**Figure 3: Blowhole Simulator**

A basic schematic of ChuffSim's internal passages is shown in Figure 3a while Figure 3b illustrates Chuffsim in mid-chuff. Figure 4 shows how the nasal passage CT scan is configured relative to a dolphin's anatomy. This CT scan, taken by Haley D. O'Brien from the Center of Health Sciences at OSU, was taken from a one-year old cadaver dolphin named Lilley [31]. This scan was obtained for the current study thanks to the help of the NSF (Grant #1725925).



**Figure 4a: DNPN Relation to Dolphin Head Schematic & CT Scan**

Using this geometry, time-dependent pressure measurements are made to develop a fluidic understanding of the impulsive jet produced by a dolphins' chuff.

### *Research Questions*

This thesis attempted to ask two basic questions: Can we reproduce a dolphins' exhalation mechanically and how does simulating a dolphins' blowfield compare to a conventional round jet? Furthermore, the device designed and tested in this thesis can be used to provide data for numerical simulations and useful in designing a UAS capable of acquiring blow samples in the wild.

## *Study Overview*

The second chapter will consist of a literature review that will contain an overview of past work on jets. More specifically, it will cover the classification of jets along with nomenclature, definitions of volumetric and momentum flux, previous work from human respiratory functions, and existing work on impulsively started jets.

Experimental methods will be covered in the third chapter. The pressure transducer calibration process, data acquisition process, flow visualization and particle image velocimetry methods, grid-survey and velocity decay techniques are all explained in detail. Turbulence intensity and self-similarity basics are explored in addition to how the pressure measurements are equated to velocity.

The fourth chapter will discuss the results from data acquired using techniques outlined in the third chapter.

Finally, the thesis will conclude in chapter 5 with conclusions and future work. The appendices will include the uncertainty calculation method, calibration method & plots, relevant figures for existing dolphin data, images corresponding to diameter evolution, data acquisition method, and pressure transducer specifications.

## CHAPTER II

### LITERATURE REVIEW

#### *Classification of Jets*

It is instructive to examine jet theory in an effort to understand the mechanics of a dolphin blowfield. Jets can be classified into three main categories: free, wall-bounded, and surface-bounded. These three categories can be broken down into many subcategories, however, the category this current study will be focusing on will be a wall-bounded (baffled) impulsively started turbulent jet. This descriptor is the most analogous to human respiratory functions such as coughs and sneezes and will also be applied to a dolphin chuff throughout this thesis.

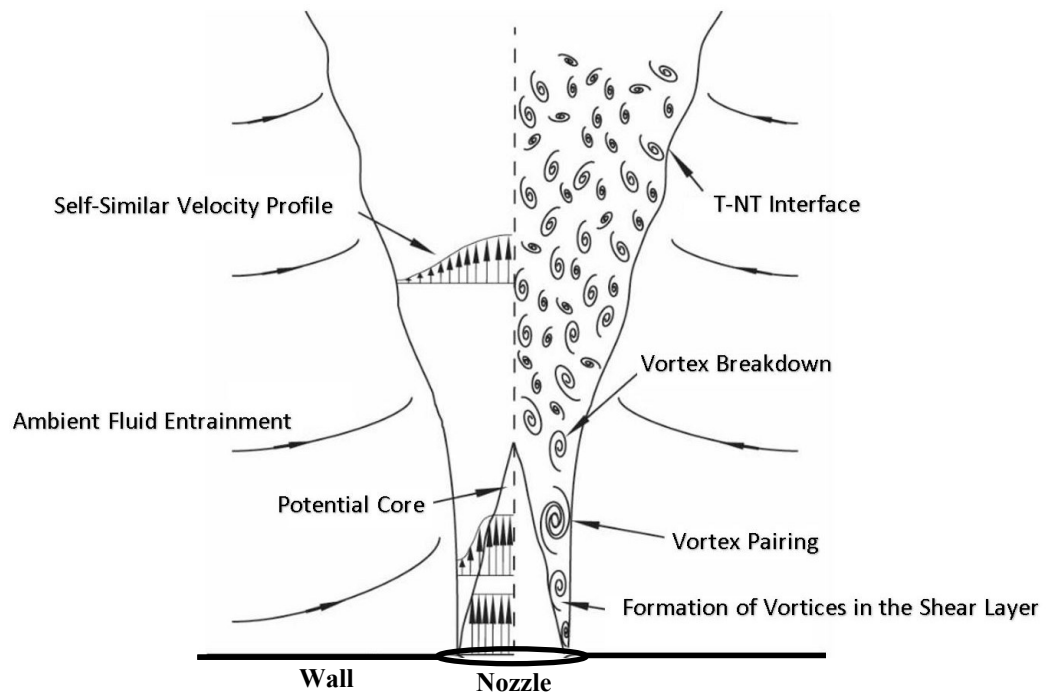


**Figure 5: Anatomy of a Jet [17]**

Above, in Figure 5, is a baffled axis-symmetric jet subjected to gravity with its key characteristic fluid structures. A dolphin blowhole is best represented as a baffled jet. As the fluid is expelled from the nozzle a potential core forms denoted as the triangular region in Figure 5 which forms a cone in three dimensions. The potential core is a result of the shear layer formed between fast moving fluid (jet) and the slow moving fluid outside the jet (zero velocity for quiescent conditions). The subsequent mixing eats away at the "core" until eventually that low turbulence core disappears. In the core, the mean velocity ( $U_{max}$ ) is roughly constant where the extent of the core typically spans 2-5 diameters axially downstream [17]. The core length and velocity decay downstream is a simple indication of whether a jet is well-mixed [37]. As the jet leaves the wall, turbulent eddies grow from the lip of the jet where a shear layer forms and propagates axially downstream. The difference in velocity gradients between the jet and the quiescent-fluid forces the shear layer to roll into the core, thus, producing toroidal vortices [17]. These toroidal vortices are among the qualitative aspects that will be explored in the flow visualization videos. At the end of the potential core the centerline velocity decreases where the primary vortices become unstable and break-up while pairing-off into smaller secondary vortices, thus, entraining more ambient fluid. The convection of primary and secondary vortices will be quantified. Finally, the small vortical structures begin to form a fully developed flow-field where a self-similar velocity profile is obtained.

### *Volumetric Flux*

This study will be using pressure measurements to calculate flow rates for the purpose of comparing the laboratory data to In-Situ data collected in both Oahu & Bermuda. Volumetric flux is a measure of a fluid's volumetric flowrate. This quantity is calculated under the assumption that no mass is lost across the control volume boundary.

$$\dot{V} = \int_{A_c} U_{mean} D_j A_c \quad (\mathbf{a})$$



$$\dot{V} = A_c U_{mean} \quad (\mathbf{b})$$

$$A_c = \frac{\pi}{4} D_j^2 \quad (\mathbf{c})$$

**Eqn. 1:**  $U_{mean}$  – centerline mean velocity,  $A_c$  – nozzle cross – sectional area,  $D_j$  – jet diameter,  $\dot{V}$  – volumetric flowrate

The formula used to calculate volumetric flowrate is shown as equation 1b. An earlier form of these equations was published around 1628 by an Italian Monk Benedetto Castelli and are still widely used in engineering disciplines.

*Momentum Flux:*

Newton’s second law can be generally applied to a fluid element in the form of equation 2a. Quantifying trajectory of jets in terms of volumetric flow rate requires the implementation of the Reynolds transport theorem.

$$\sum \vec{F} = \frac{d}{dt} \int_{sys} \rho \vec{V} dV \quad (\mathbf{a})$$

$$\sum \vec{F} = \frac{d}{dt} \int_{CV} \rho \vec{V} dV + \frac{d}{dt} \int_{CS} \rho \vec{V} (\vec{V} \cdot \vec{n}) dA \quad (\mathbf{b})$$

**Eqn. 2:**  $\rho$  – fluid density,  $\vec{V}$  – mean velocity,  $\vec{n}$  – unit vector,  $dV$  – change in volume,  $dA$  – change in area,  $\frac{d}{dt}$  – time derivative,  $\sum \vec{F}$  – sum of the forces in a system

Equation 2b represents 2a in terms of a fixed control volume where the first term of the right-hand side is the time rate of change of linear momentum and the second term is the net flow rate of linear momentum out of the control surface by mass flow. The left-hand side of equation 2b is the sum of all external forces acting on the control volume [7]. Using these relations in

conjunction with momentum flux ratio it is possible to determine a jets trajectory within a crossflow. This topic will be discussed in more depth at the end of this chapter.

### *Impulsively Started Jets*

Impulsive jets are most commonly found in mammalian respiratory functions such as dolphin chuffs, human coughs, and human sneezes where the body exerts a forceful breath of finite volume. A study conducted on zero-net-mass-flux (ZMNF) jets, also known as synthetic jets, are closely related to impulsive jets observed in the current study as they are generated using a reciprocating piston. The flow visualization shown in Figure 6 compare a ZMNF jet to an equivalent continuous jet (FOV=76D0×39D0,  $Re_0 = 10^4$ ,  $Str\# = 0.0015$ ) based on momentum flow velocity. The lines represent the relative spread of the jet. The apparent spreading rate for the ZMNF jet (top image) is  $\sim 0.13$  compared to  $\sim 0.10$  for the equivalent continuous jet (bottom image) [7].

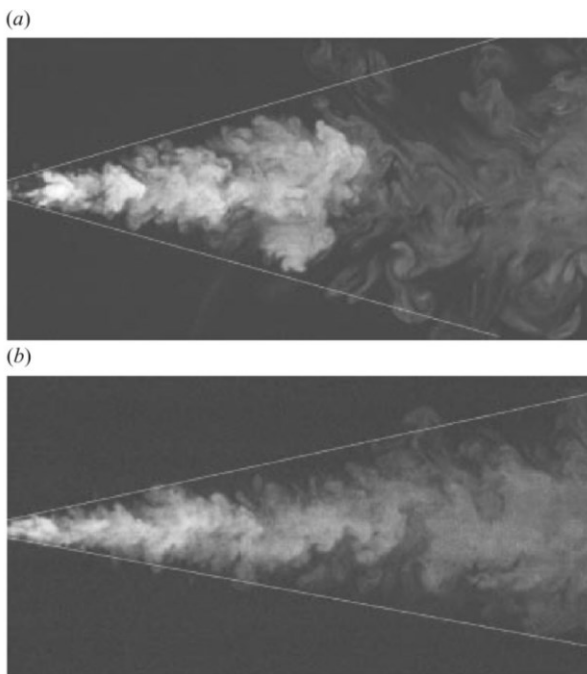


**Figure 6: ZMNF Jet (a) versus Continuous Jet (b) [7]**

Cater and Soria (2002) demonstrated that the round turbulent ZNMF jet has a spreading rate greater than an equivalent continuous jet throughout the measured domain as indicated in Figure 7 which shows the axial velocity profiles normalized by the centerline velocity @  $x/D = 60$ . The circles represent the continuous jet while the squares represent the ZNMF jet. It is inferred that the continuous jet spreads at a lower rate than the ZNMF jet. The x-axis is in terms of  $\eta$  which is a similarity variable defined as the radial coordinate non-dimensionalized by the axial location. This axial coordinate system will not be used in the current study.

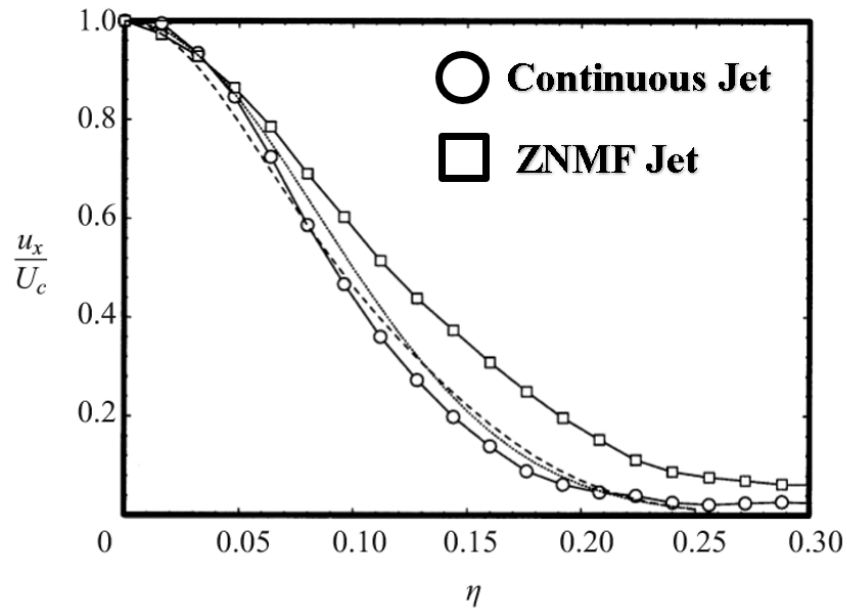


**Figure 7: Normalized Profiles of Axial Velocity @  $x/D = 60$  [7]**

The structural near-field differences of ZNMF jets are responsible for different streamwise velocity gradients and therefore different spreading and decay rates when compared to continuous jets [7].

A defining characteristic of impulsive jets, described by Johari et al. [1997], are that their initial vortex ring travels faster than the starting vortex which will be referred to as the “jet tip”. The jet tip travels at approximately one-half of the centerline velocity when compared to a steady

jet. This perhaps foreshadows that a chuff might behave differently relative to conventional jets in the far field. This study inferred that fluid near the jet tip mixes with the ambient fluid faster than the rest of the finite mass transported from the jet orifice. Abramovich and Solan's experimental data showed that the increased mixing of mass near the jet tip implied faster momentum diffusion which supports the decrease in jet-tip velocity when compared to a steady jet. The faster momentum diffusion may pose an issue when subjecting an impulsively started jet to a cross flow impacting the overall penetration of the fluid. Witze et al. also showed that the starting jet entrainment was  $\sim 30\%$  greater than a steady jet's when using a turbulent jet model [37]. The greater entrainment rate of the turbulent plume causes it to decrease in velocity axially which is why the vortex ring "outruns" the jet tip. This is evident in Figure 8 where the vortex ring propagates downstream at a quicker rate than the jet tip. This general characteristic of impulsively started jets shows the disparity between axial velocity magnitude when compared to conventional jets where the conventional jet velocity tends to be greater than the impulsively started jet. The vortex ring was observed to have less entrained mass strengthening the spatial discrepancy between it and the jet-tip. The structures that form in the plume behind the jet tip are similar to those in steady jets described earlier in this section [17]. These fluidic structures will be described in more detail during the flow visualization section in the current study. Developing a better understanding of parameters such as momentum ratio will dictate the minimum altitude a drone would need to fly in relation to a chuff to successfully capture its hormone-laden fluid.

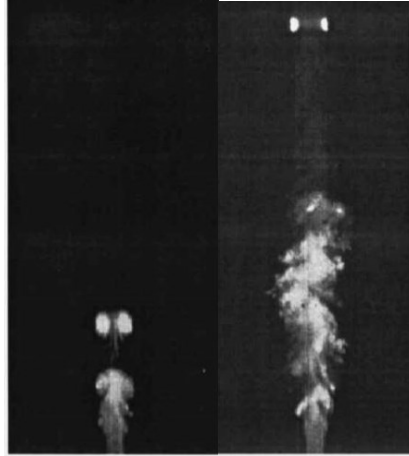


**Figure 8: Laser Induced Fluorescence Images of Impulsively Started Jets [19]**

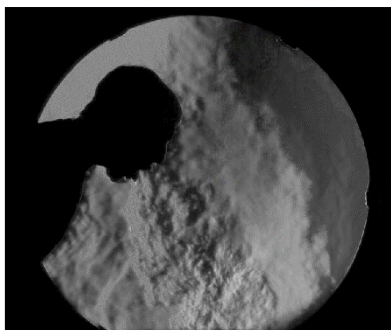
### *Multiphase-Flow*

The fact that the dolphin chuff is, in actuality, both a multi-phase flow and something that is expelled typically into a cross flow (while a dolphin is moving) is an important dynamic. While these conditions are not examined in the present work, it is instructive to discuss them briefly.

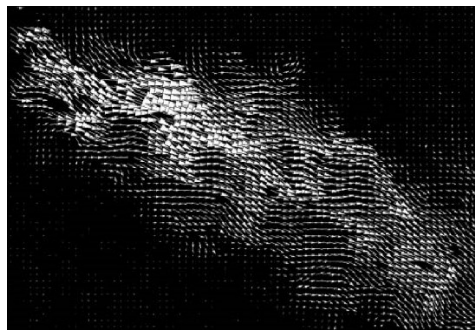
During a forceful breath exerted by a dolphin a mixture of three main fluids are expelled: air, mucus, and sea water. Multiphase impulsive flow has been studied in the past in regard to respiratory particle transport during the H1N1 and revamped due to the COVID-19 pandemic as response to the spreading of an infectious disease [25]. The present study will only focus on qualitative measures of multiphase flow from flow visualization techniques to further the understanding of impulsive species transport at higher nominal flow rates.

The impulsively started jets produced by human respiratory functions serve as an important benchmark in relation to blowfields. The existing data in this field provides important context to the nature of these biological jets in relation to conventional jets.

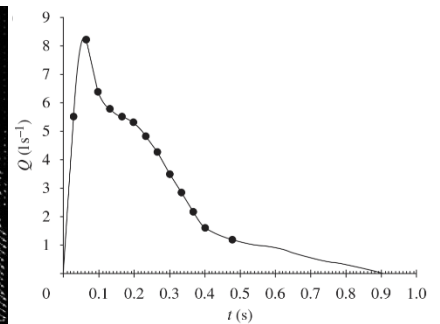
In the early 1940's Jennison et al. estimated the maximum distance spanned by droplets from a sneeze to be 2-3 feet with an initial velocity of  $\sim 150$  ft/s. Mucus droplets generated from human respiratory functions typically range from 5-20  $\mu\text{m}$  in size. Nicas et Al. (2005) show by modeling that droplets emitted during a cough or sneeze will evaporate to 50% of their initial value instantaneously. Zhu et al. (2006) measured the velocity of In-Situ coughs from an array of subjects by utilizing PIV with flour seeding. The initial velocities ranged from 19-70 ft/s  $\pm 9$  ft/s with an average velocity of 36 ft/s [29]. The abrupt release of fluid in the lungs projects an impulsively started turbulent jet from the mouth and/or nose with significant momentum. This aerosol infused jet, led by a characteristic vortex ring, is capable of penetrating large distances into the quiescent air before mixing out owing to turbulent entrainment [35]. Both coughs and sneezes were estimated to have a volume of roughly 2.5 liters from Mahajan et al.'s (1994) data with an average mouth diameter of  $\sim 30$  mm. While the tidal volume of humans is much lower than a dolphin's, the diameter of the mouth is similarly sized to a blowhole. Coughs are classified in the short duration regime similar to a fuel injector jet which is not to be confused with a very short duration regime where most of the cough would be entrained into a single vortex ring. Figure 9a shows a schlieren flow image of a 25 year-old male coughing downward illustrating the turbulent nature of the impulsively started jet produced by a cough. The typical wave-form produced by a cough is shown in Figure 9c where it is indicated that a forceful respiratory effort is biased towards the positive slope (left side) and steadily decays toward the end of the cough [35].



(a)



(b)



(c)

**Figure 9: Schlieren image of a cough directed downward by a 25-year-old male subject, revealing the character of the cough as a turbulent jet of air [35]; PIV of an In-Situ cough (b) [25]; The wave-form of a typical ‘single forced cough’ in terms of expelled airflow rate versus time, adapted from Khan et al. (2004) (c) [25]**

Wei & Li (2017) modelled coughs as a two-stage jet with three separate waveforms, a sinusoidal wave (case 5), a square wave (case 1), and the waveform provided by Khan et al. in 2004 (case 8). Figure 10 illustrates each of these cases produced by a piston cylinder apparatus in a tank utilizing blue color dye. This results of the three separated waveforms tested show little to no discernible difference in the jet tip penetration at higher flowrates. This suggests that replicating the waveform may not be as important as replicating the nominal flowrate desired. The general nature of impulsive waveforms will be discussed in more depth later in the study. Wei & Li (2017) also confirmed coughs contain key jet characteristics that are impulsively started. The cough’s jet dynamics are in agreement with characteristics described by Witze, Abramovich & Solan, and Cater & Soria who observed that these jets consist of a leading vortex (jet tip) followed by a trailing flow that penetrates the ambient fluid with less speed than a conventional jet [6, 33, & 34]. Wei & Li (2017) showed the maximum penetration for all test cases to be in the range of  $x/D = 50.6 - 85.5$  [37].

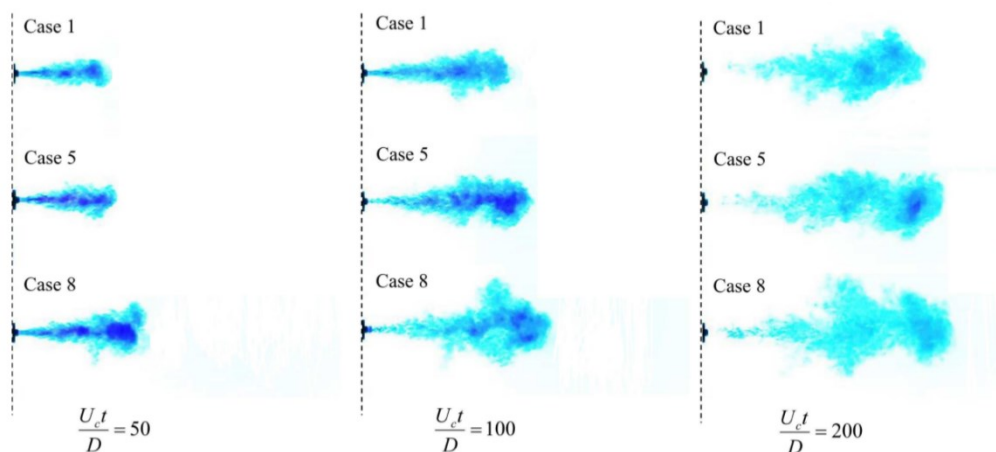


**Figure 10: Visualizations of the Turbulent Round Starting and Interrupted Jets ( $D_j = 4\text{mm}$ ) [37]**

Nishimura et al. (2013) analyzed the dynamic nature of sneeze bioparticle plumes, not only the mouth vicinity but the whole sneeze cloud, for the first time. They observed the sneeze mist mass to diffuse approximately 0.4 seconds after sneezes were initiated. In addition, the largest droplets fell with a high speed and disappeared 0.2 seconds after an In-Situ sneeze. This showed that larger particles in the flow propagate independently of the flow-field while the finer mist ( $>10\ \mu\text{m}$ ) follows the gas trajectory more closely [39]. In other words, the aerosolized particles follow a more predictable trend than the larger mucus particles. The PIV images acquired during this study are shown below in Figure 11 that shows a healthy adult male in their 20's sneezing showing the evolution of a sneeze versus time [29].

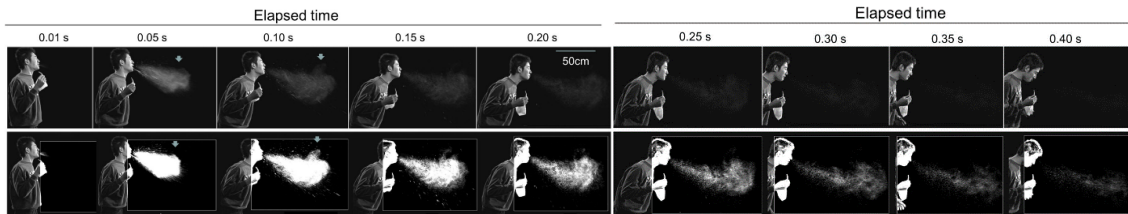


**Figure 11: Time Resolved Sneeze Evolution**

While coughs and sneezes are not completely analogous to dolphin chuffs, the study of human respiratory functions exist as an important benchmark for this new area of research.

The only existing data on jet dynamics of a dolphin blowfield, thus far, is a two-phase CFD (computational fluid dynamics) simulation performed by Dr. Aaron Alexander from the Engineering Technology department at Oklahoma State University. In order to properly simulate a blowfield the CT scan, taken by Haley O'Brien and made possible by NSF (Grant number 1725925), was modified by Dr. Alexander since the original geometry portrayed the dolphin blowhole closed. Figure 4b shows what the geometry looked like before and after the modification process [28].



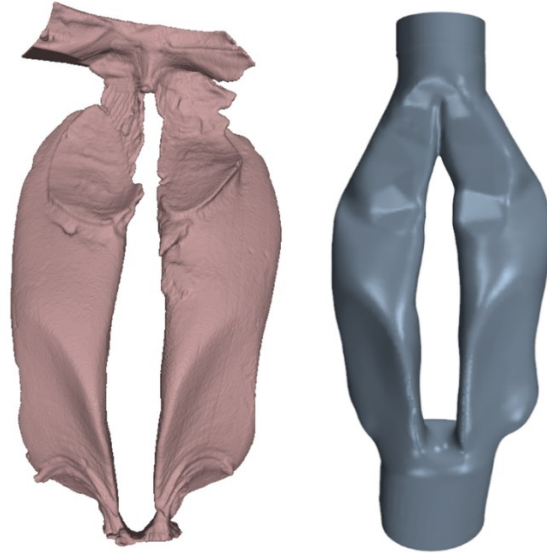


**Figure 4b: Original CT Scan (left) versus Modified CT Scan (right) [2]**

The modification process, performed by Dr. Alexander, smooths out the somewhat messy physiology into a more useable flow passage. After successfully smoothing out the geometry a STAR-CCM 14.04.013 simulation ( $k-\omega$  RANS Menter SST,  $\sim 600,000$  cells, BC's: [Mass Flow Inlet, Pressure Outlet, Stagnation Inlet Side Walls], Lagrangian multiphase w/ 0.5 mm OD water particle) was conducted using the respiratory flow rate data from Fahlman et Al. (2015). This data modelled a static dolphin (no cross flow) using flow rate parameters from a voluntary breath rather than a chuff. The data from the simulation showed particles leaving the blowhole at speeds up to  $\sim 112$  ft/s. The plume from the simulation exhibited characteristics, similar to those witnessed In-Situ, from bottlenose dolphins in human care. Dr. Alexander concluded that future CFD simulations should include head-wind induced by dolphin swimming, initiate higher jet velocities, duplicate fluid properties of dolphin mucus, and duplicate the ratio of mucus to air [2]. Using data collected from the current study in addition to these considerations, it will be possible to properly simulate blowfields in a cross flow.

## *Qualitative Characteristics of Jets in Cross Flows*

Researchers hope to capture hormone data from dolphins in the wild. This will involve tracking wild dolphin pods in open-ocean where dolphins will forcefully exhale while swimming into a cross-wind of varying magnitude. Thus, the behavior of impulsively started jets in a crossflow is critical to the CONOPS. Because this aspect was beyond the scope of this thesis a basic background of conventional jets in cross-flows will be provided below.

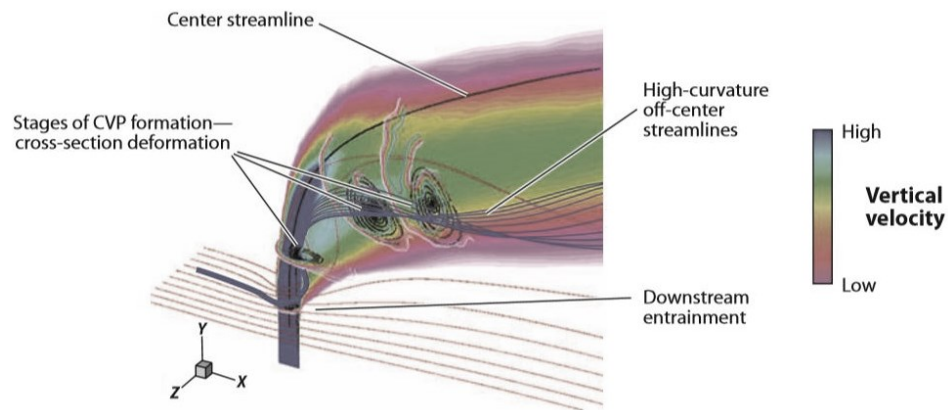


**Figure 12: Mean Flow for an Incompressible Transverse Jet [24]**

Contours of the vertical velocity for a jet subjected to a cross-flow is shown in Figure 12. The figure represents results from a DNS (direct numeric simulation) with a Reynolds number  $\sim 5,000$ ,  $r = 5.7$  (Muppidi & Mahesh 2007). The simulations were performed under the same conditions as experiments conducted by Su & Mungal (2004) to which they show good agreement. The contours of the average velocity show the jet bending in the direction of the cross-flow and increasing in width as the wake moves downstream. The jet trajectory based on the center streamline penetrates deeper into the cross flow than the trajectory based on vorticity (Fearn & Weston 1974). Note that the jet is wider on the leeward side than the windward side of the center streamline; due to these imposed boundary conditions, the cross-section of the jet evolves from its circular shape to form a counter-rotating vortex pair (CVP). CVP formation

occurs as a result of the jet vorticity modification initiated in the nearfield as a result of the cross-flow (e.g., Moussa et al. 1977, Andreopoulos & Rodi 1984, Sykes, Lewellen & Parker 1986, Coelho & Hunt 1989). These observations were made from experiments conducted at velocity ratios ranging from 2.0-6.0 and Reynolds numbers between 440-6,200. Vortex element simulations were also conducted by Marzouk & Ghoniem (2007) suggesting that the initial in-plane vortex rings generate close to the jet exit and stretch upward on the leeward side. Consequently, the vorticity is aligned in the direction of the cross-flow, hence, yielding a CVP.

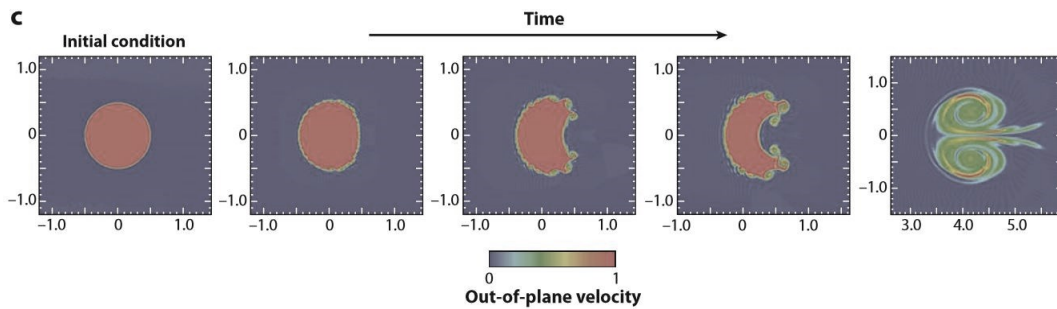


**Figure 13: Evolution of out-of-plane Velocity into CVP [24]**

Horseshoe vortices form upstream of the jet’s leading edge (windward side) and efflux downstream. These vortices form as a result of the cross-flow boundary layer encountering an adverse pressure gradient upstream of the orifice. These vortices then separate to form spanwise vortices that move around the jet as shown in Figure 13. Fric & Roshko (1994) suggested that the wake vortices originate from separation events in the cross-flow boundary layer downstream of the jet [24]. These insights will not be explored more than qualitatively and speculatively in the current study but should be further investigated in the future work.

#### *Jet Penetration into Cross Flows*

The quantitative aspects of cross-flows that will be covered in the current study will be the comparing velocity and momentum flux ratios. Both of these quantities will be compared to previous knowledge to form a better understanding of how cross-flows could tentatively prevent

chuff penetration making the acquisition of biological material more difficult. The velocity ratio and momentum flux ratio are defined below in equation 3 & 4 respectively.

$$r = \frac{U_j}{U_\infty}$$

**Eqn. 3 :**  $U_j$  – mean jet velocity,  $U_\infty$  – crossflow mean velocity,  $r$  – velocity ratio

$$J = \frac{\rho_j U_j^2}{\rho_\infty U_\infty^2}$$

**Eqn. 4 :**  $\rho_j$  – jet density,  $U_j$  – mean jet velocity,  $\rho_\infty$  – crossflow density,  $U_\infty$  – crossflow mean velocity

Previous work on jets in a cross flow exists in the field of gas turbine combustors where relations between  $r/D$  vs.  $x/D$  &  $J/D$  vs.  $x/D$  help to determine trajectory and ultimately dilution. This current study will focus on the trajectory aspect of these studies as they will give important insight as to how crossflows will impact chuffs. Plots such as Figure 14 will be replicated and serve as an approximation for predicting chuff trajectory during open-ocean swimming.

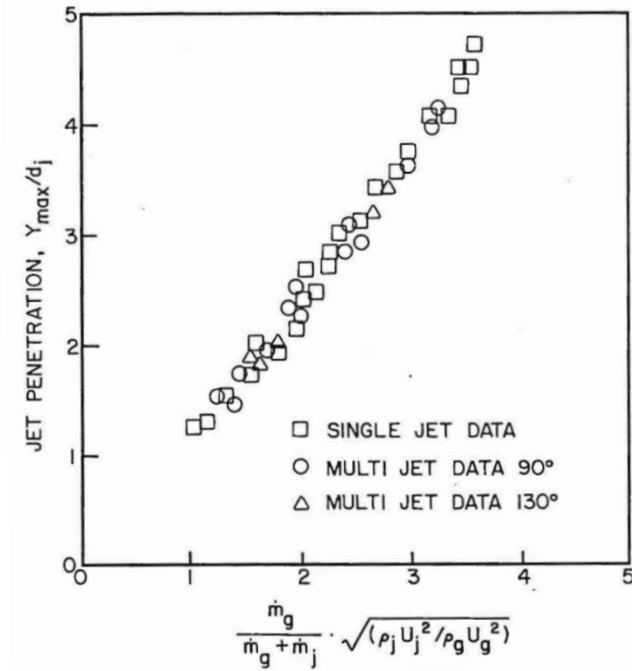


**Figure 14: Predicted Trajectories for a System of Jets Penetrating into a Circular Cylinder [22]**

As a jet penetrates a cross flow it creates a blockage where the maximum penetration is equated to the depth that the centerline velocity becomes asymptotic to the freestream flow. Using data collected and analyzed by Lefebvre equation 5 shows that jet penetration increases continually with the increase in distance downstream. The jet may attain its maximum penetration a fairly short distance downstream making equation 6 a more practical method of determining maximum penetration.

$$\frac{y}{D} = 0.82J^{0.5} \left(\frac{x}{D}\right)^{0.33}$$

**Eqn. 5:**  $J$  – mometum flux ratio,  $\frac{x}{D}$  – non dimensional radial diameter,  $\frac{y}{d}$  – non dimensional axial diameter [22]

Using the empirical formula found by Norster (1975) the current study will approximate the maximum penetration for the flow rates and nozzle geometries investigated.

$$Y_{max} = 1.15 D_j J^{0.5} \sin\theta$$

**Eqn. 6:**  $D_j$  – nondimensional jet diameter,  $J$  – momentum flux ratio,  $\theta$  – cross flow injection angle [22]

The present study will quantify the initial conditions necessary to develop impulsive simulations and provide the benchmark for continued work in multiphase and cross-flows. Understanding the manner in which jets react in a cross-flow will ultimately lead to the next stage in this study to capture chuffs via UAS at open ocean speeds of 10-40 miles per hour (depending on dolphin species) [3 & 20].

## CHAPTER III

### EXPERIMENTAL METHODS

#### *Design & Manufacturing of ChuffSim*

In order to accurately replicate an impulsive forceful breath produced by a dolphin a machine (*ChuffSim*) was designed and manufactured at Oklahoma State University. *ChuffSim* can produce an impulse at a flow rates of ~44-84 liters/second for a duration of ~0.25-0.35 seconds (depending on nozzle geometry). It achieves this by using a linear piston cylinder setup where the pistons are driven from TDC (top-dead-center) to BDC (bottom-dead-center) through use of four solenoid-valve actuated air cylinders (Figure 15). The device requires ~120 psi of compressed air @10 SCFM to power the hydraulics that compress the air in the cylinders of the apparatus. The simulator design initiates the impulse at the press of a button; tidal volume cylinder capacity is oversized (~47.2 liters) to compensate for fluid leaks. The volume expelled is controlled by adjusting the stroke length or by-passing cylinders in the system via the contraction nozzle shown in Figure 15.

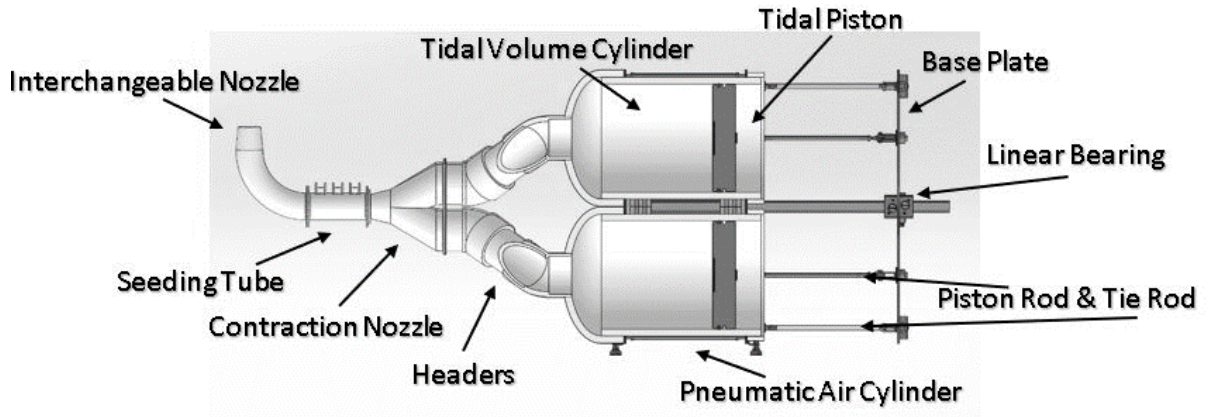


**Figure 15: ChuffSim CAD Assembly with Labels**

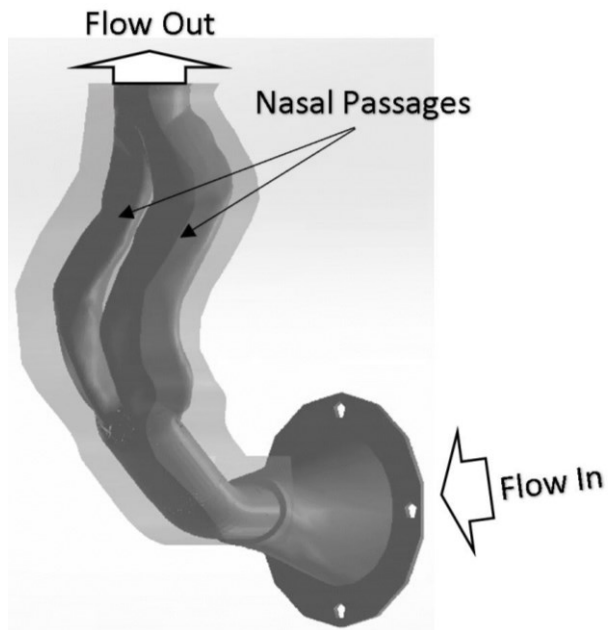


**Figure 16: Integration of CT Scan into ChuffSim**

The cylinders exhausts join into one contracting nozzle that attaches to a 3D printed geometry of a dolphin nasal passage. The nasal passage geometry was obtained through a CT scan taken of a one-year old cadaver dolphin by the Integrative Biology department at Oklahoma State University . The original CT scan went through an iterative design and modification process to get the geometry into a usable format. The geometry was scaled-up to an adult sized



nasal-passage using a 20/13 ratio based on the relative head size of the cadaver dolphin to an adult dolphin [6].

#### *Data Acquisition of ChuffSim*

In the present study two different methods were used to analyzed and quantify the blowfield. The first method uses Particle Image Velocimetry (PIV) and the second method uses an unsteady pressure transducer.

The unique jet produced by a dolphin's nasal passage can be better understood by comparing it to an equivalent round jet of the same area. In the present study, this equivalent or baseline nozzle will be referred to as the Round Conventional Nozzle (RCN) and its characteristics will be compared to the Dolphin Nasal Passage Nozzle (DNPN)-(Figure 17).

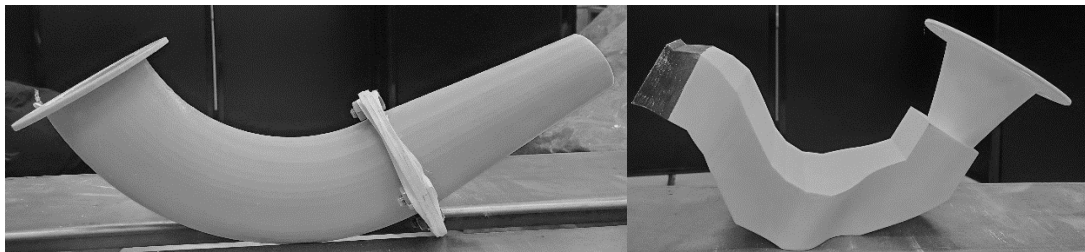


**Figure 17: 3D Printed Round Conventional Nozzle & Dolphin Nasal Passage Nozzle**

#### *Pressure & Velocity Measurements*

An Endevco Model 8507C-5 pressure transducer was calibrated using the apparatus shown in the top image of Figure 18 where a 3/8" steady jet vents compressed shop air to ambient conditions. A pitot tube coupled to a digital pressure gauge measures the dynamic pressure experienced in the potential-core of the jet. As discussed in the previous chapter, it is assumed that the fluid within the potential core is traveling at a constant velocity  $U_{\text{mean}}$ . This was used as the reference gauge pressure data for the transducer. The pressure measured by the pitot tube and pressure transducer is changed by opening or closing the pressure regulator at intervals defined by

the analog pressure gauge attached to the regulator shown in the schematic in Figure 18. This action produces a steady jet that allows the user to control the speed and make pressure readings at known pressure fields.

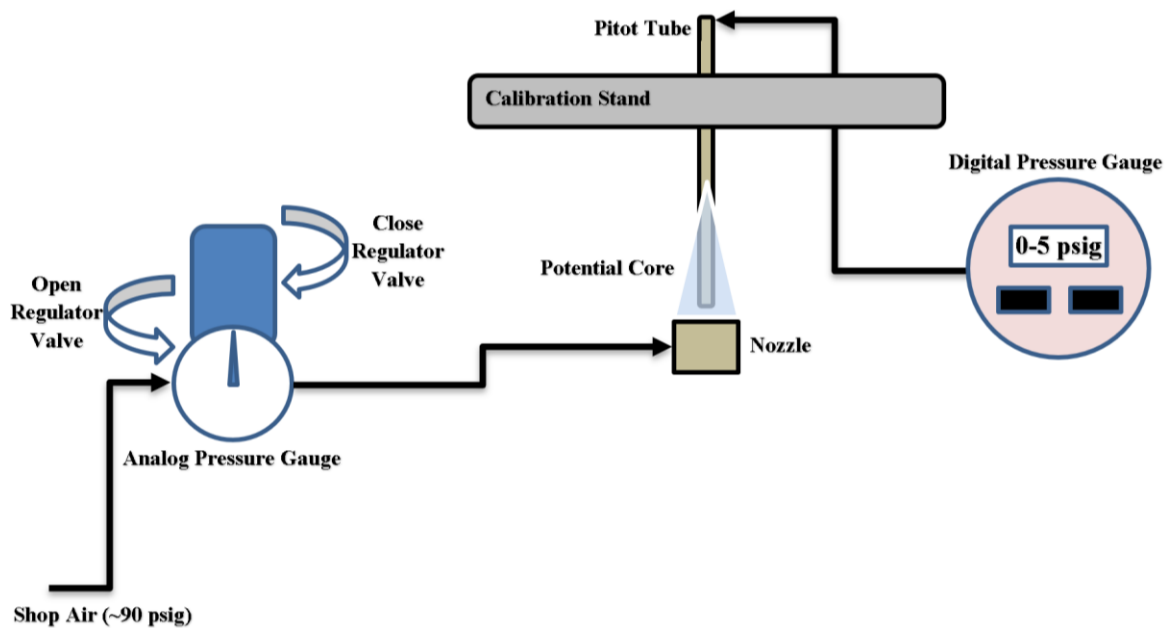
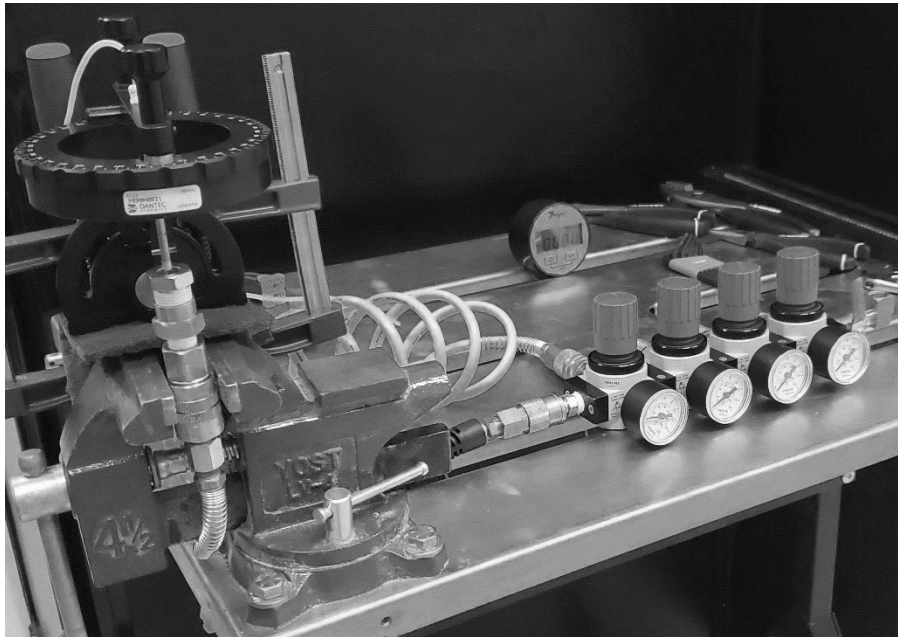


**Figure 18: Pitot Tube Calibration Apparatus**

The location of the pitot tube is the same location the pressure transducer is mounted. The surface of both measuring devices are flush to the opening of the jet as shown in Figure 18. The pressure intervals for both data sets are compared on one graph to form the calibration shown in Appendix A, Figure A1.

### *Converting Pressure to Velocity*

Isentropic equations can be used to compute (via pressure probe) velocity measurements using pressure. These equations hold true for adiabatic and reversible processes [8].

$$M = \sqrt{\left(\frac{2}{\gamma - 1}\right) * \left(\left(\frac{P_0}{P}\right)^{\left(\frac{\gamma - 1}{\gamma}\right)} - 1\right)} \quad (\mathbf{a})$$

$$T = \frac{T_0}{1 + \left(\left(\frac{\gamma - 1}{2}\right) * M\right)^2} \quad (\mathbf{b})$$

$$V = M (\gamma * R * T)^{0.5} \quad (\mathbf{c})$$

**Eqn. 7 :**  $M$  – mach number,  $\gamma$  – ratio of specific heats,  $P_0$  – measured pressure,  $T$  – total temperature,  $T_0$  – static temperature,  $R$  – air gas constant,  $P_0 =$  total pressure,  $P$  – static pressure [8]

### *Turbulence Intensity*

Using the discrete instantaneous velocity data across the nozzle a brief turbulence intensity study was conducted for both nozzle geometries. Traditionally, in engineering disciplines, calculating the Reynolds number is how a regime is classified as either turbulent or laminar. Equation 8 defines the Reynolds Number which is the ratio of inertial forces over the viscous forces in a system.

$$Re = \frac{UL}{\nu}$$

**Eqn. 8:**  $Re$  – Reynolds number,  $U$  – mean velocity,  $\nu$  – kinematic viscosity [3]

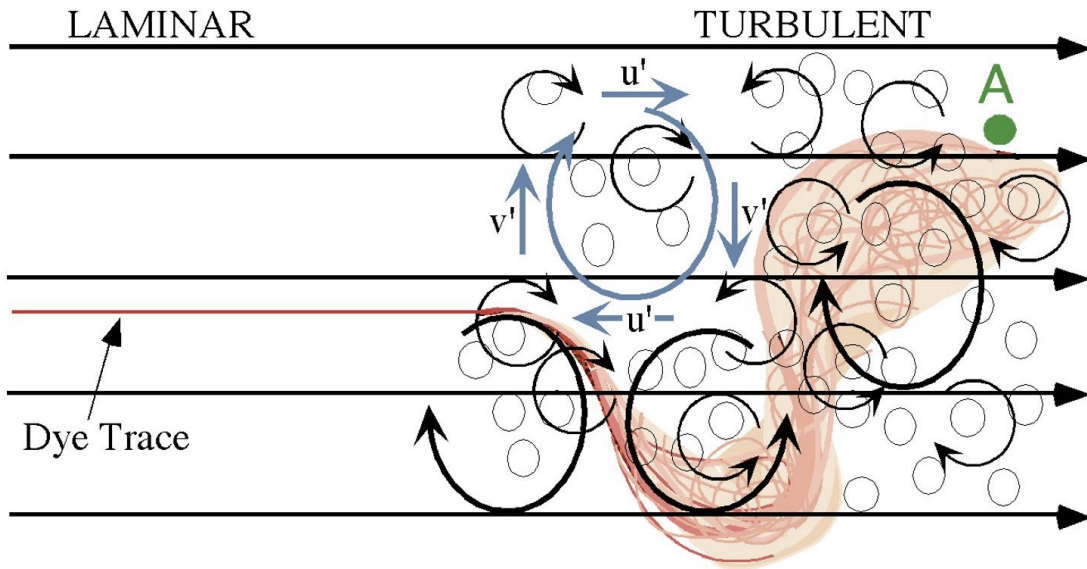


**Figure 19: Laminar versus Turbulent Flow Regimes [3]**

To obtain a better understanding of turbulence nature within a flow-field the use of Figure 19 is helpful. For the turbulent flow section eddies of many sizes are super-imposed throughout the mean flow as indicated by the dye trace on the right side of the image. Note that the dye trace jumps across streamlines due to the perturbations of fluid velocity normal to the streamlines “ $v$ ”.

$$\bar{u} = \frac{1}{N} \sum_{1}^{N} u_i \quad (\mathbf{a})$$

$$\bar{v} = \frac{1}{N} \sum_{1}^{N} v_i \quad (\mathbf{b})$$

**Eqn. 9:**  $N$  – number of velocity points,  $u_i$  – instantaneous 'streamwise' velocity,  $v_i$  – instantaneous 'streamwise normal' velocity [3]

The turbulent eddies in a flow field create fluctuations in a fluid's instantaneous velocity. For a turbulent flow the velocity trace includes both a mean ( $\bar{u}$ ,  $\bar{v}$ ) and fluctuating ( $u'(t)$ ,  $v'(t)$ ) shown in Equations 9a & 9b and 10a & 10b respectively for both the streamwise component 'u' and streamwise normal component 'v'.

$$u(t) = u'(t) + \bar{u} \quad (\mathbf{a})$$

$$v(t) = v'(t) + \bar{v} \quad (\mathbf{b})$$

**Eqn. 10:**  $\bar{v}$  – mean 'streamwise normal' velocity,  $\bar{u}$  – mean 'streamwise' velocity,  $u'(t)$  – instantaneous 'streamwise' velocity fluctuation,  $v'(t)$  – instantaneous 'streamwise normal' velocity fluctuating

This study is only concerned with velocity fluctuations in axial direction. Because the turbulent fluctuations are considered "random-like" they can be characterized by using the statistical concept of variance to quantify the turbulence intensity. Equation 11a and 11b are used to calculate turbulence strength and turbulence intensity using values from equations 9 and 10 from discrete velocity points ( $u_i$  &  $u'_i$ ) obtained through the velocity grid survey of each nozzle's blowfield.

$$u_{rms} = \sqrt{\frac{1}{N} \sum_{i=1}^N (u'_i)^2} \quad (\mathbf{a})$$

$$Turbulence Intensity = \frac{u_{rms}}{\bar{u}} \quad (\mathbf{b})$$

**Eqn. 11:**  $u_{rms}$  – root mean squared velocity [3]

The subscript “rms” in equation 7a stands for root-mean-square which is defined as the standard deviation of the set of the “random” velocity fluctuations present in a flow. Using these equations, a statistical analysis of the mean axial velocity fluctuations will be calculated in the fourth chapter.

### *Blowfield Self-Similarity*

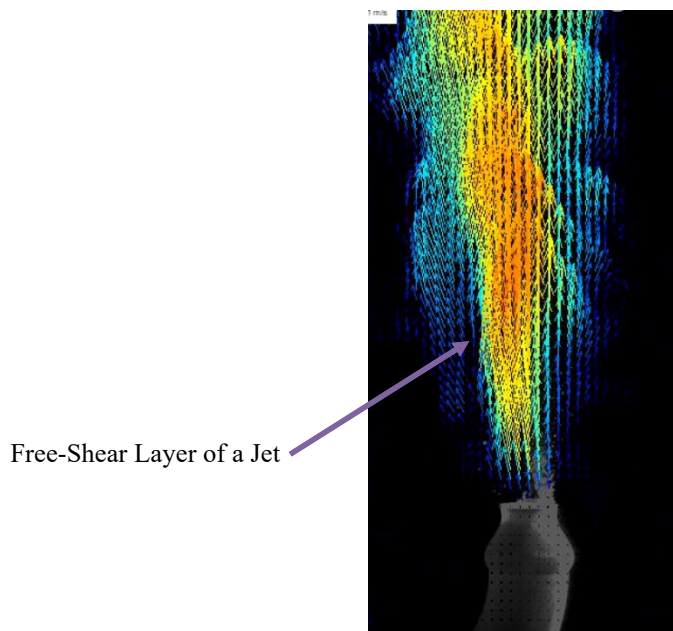


**Figure 20: Example of a Free Shear Layer in a Jet**

For the case in this study a boundary does not exist, rather, a free-shear layer exists between the moving jet and the quiescent fluid as shown in Figure 20. The mean velocity profiles obtained through the grid survey are normalized by the maximal plane velocity to emphasize that the mean and turbulent profiles within a blowfield are self-similar. In other words, both profiles have the same shape regardless of external flow magnitude ‘ $U_\infty$ ’. From self-similarity, there is a general rule of thumb that the turbulence level increases with the freestream velocity ( $u_{rms} \propto U_\infty$ ). In addition, when the turbulence level increases the laminar sub-layer thickness decreases.

This increases the vertical transfer of momentum across the free-shear-layer by a fluid [3]. Self-Similarity profiles will be plotted in Chapter Four using mean velocity values across the y & z planes for both nozzle geometries.

### *Pressure Measurement Technique*

The set-up to acquire gauge pressure data is used to characterize the velocity field over the nozzle, depicted in Figure 18, where the pressure transducer is surveying the origin of the DNPN @  $x/D = 0$ . The survey was conducted for both the RCN and the DNPN @  $x/D$ 's of 0-4 to produce velocity profiles across the extent of each plume (Figure 24). An example of data acquired from the unsteady pressure transducer is in Figure 21 where the gauge pressure was converted into units of velocity using the isentropic relations for Mach number (M), Temperature (T), and Velocity (V) using equations 9a, 9b, and 9c. An example of the data taken by the pressure transducer and converted into units of velocity is illustrated below (Figure 21).

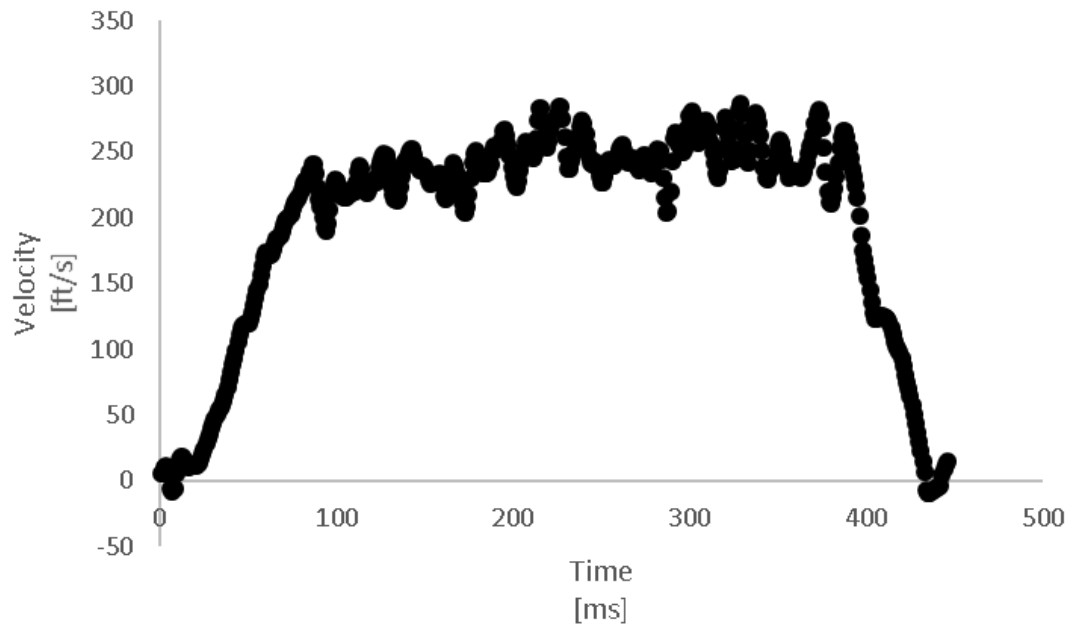


**Figure 21: DNPN Centerline Velocity Trace @  $x/D = 0$**

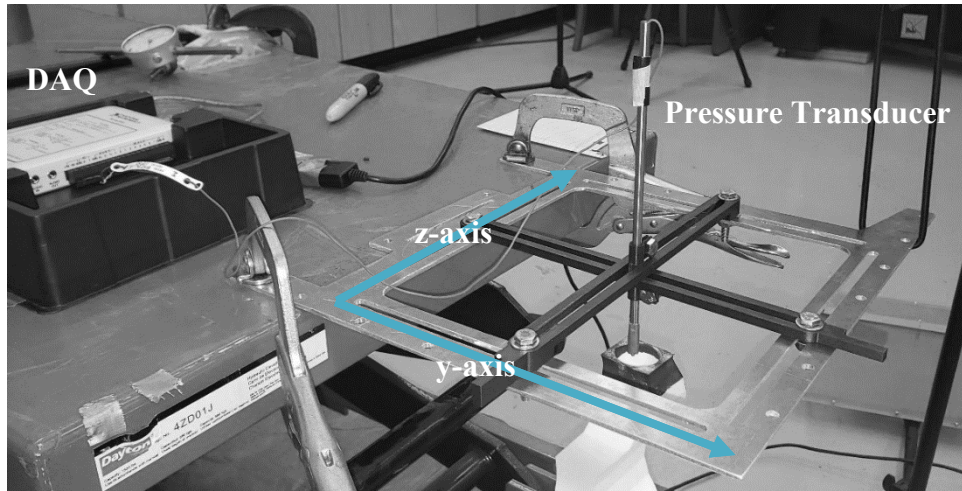


**Figure 22: Pressure Transducer Grid-Survey Apparatus**

Figure 22 shows the apparatus used to traverse axial planes for the Control Nozzle and DNPN nozzle geometries. The platform that the apparatus is clamped to can traverse the  $x/D$  axis and the black slide rules traverse the  $y$  and  $z$  axis. Figure 23 illustrates the  $y$ - $z$  plane with respect to the origin of the DNPN. In the orientation shown the dolphin head would reside at the bottom of the field of view and the tail at the top.

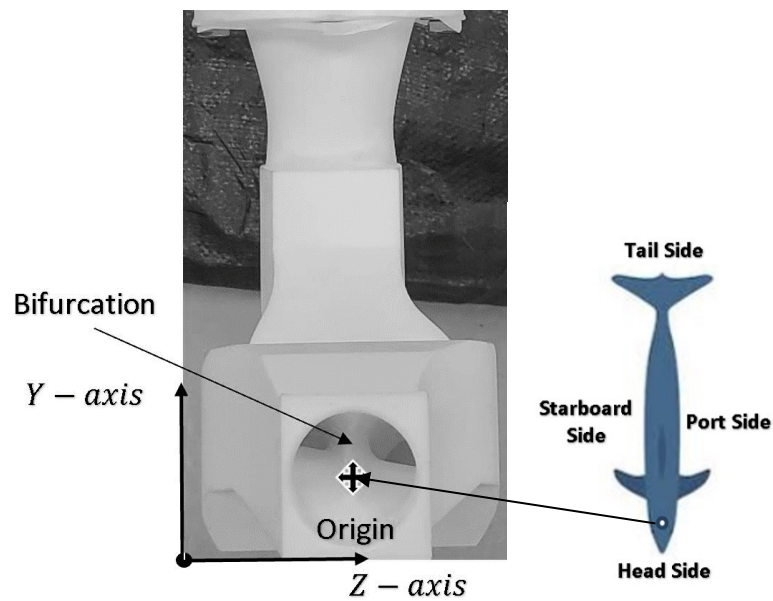


**Figure 23: Coordinate System for Grid-Survey**



Each logged run from the pressure transducer consists of first filling the 30-gallon tank with a small compressor to ensure ChuffSim air cylinders receive the proper flow rate. Next, the transducer is warmed-up through the Labview signal testing interface to ensure accuracy from the single-point unsteady probe. Once the tank is full (~135 psig) the Labview program is manually triggered to record 10 seconds of data (10,000 data points). Seconds after data logging is initiated the ChuffSim solenoid switch is thrown and the pressure data is acquired. The data is opened and checked to ensure quality and then saved as an LVM file with the y-z plane coordinate. Next, the transducer coordinate is changed via the slide-rule style axis. The x-axis position is controlled using a pneumatic scissor-lift table with infinite adjustments between two set points. The x-axis is only changed once there are a sufficient amount of points to characterize the plane. Each coordinate is reconfirmed using dial calipers for the y, z, and x axis. Because the system only emits a finite volume of fluid per chuff, the machine must be reset for each data point. This consists of manually pulling the baseplate from BDC to TDC to reset the volume for another chuff. After two runs the 30-gallon tank is refilled to increase ChuffSim's repeatability. The coordinate patterns used to survey each x/D plane consisted of jogging the pressure transducer across different radial planes at discrete points until achieving two separate zero-velocity values as shown in Figure 24; this would indicate that the edge of the blowfield was achieved. The grid-survey procedure was necessary to ensure better velocity-field resolution when plotting each velocity plane. This is not to be confused with a grid-dependency study. This method was repeated for x/D planes 0-4 for both the Control Nozzle and the DNPN.

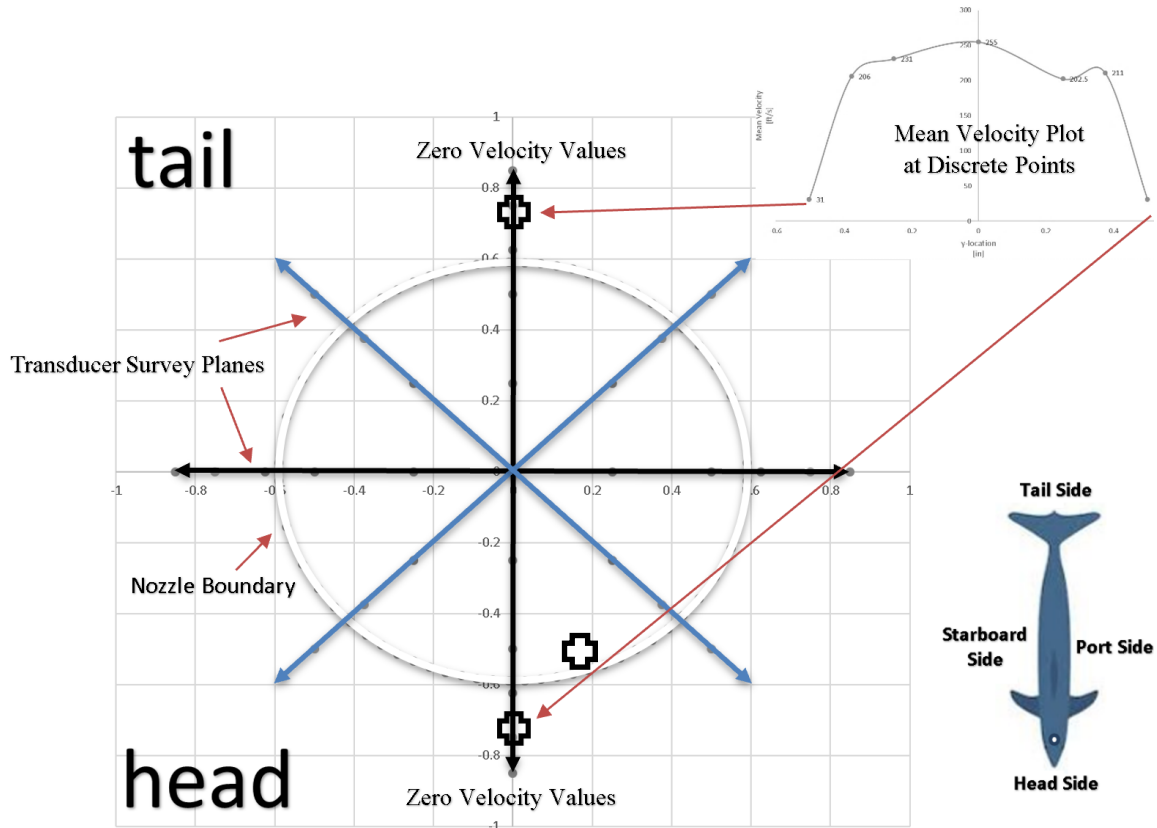


**Figure 24: Grid-Survey Methodology with Velocity Profile Example**

*Jet Centerline Measurements*

Velocity measurements are made axially downstream in the x-axis to show trend of maximum plane velocity decay. Maximum plane velocity is determined using the same method described for the grid-survey for 18 separate planes for the RCN and the 12 planes for the DNP. The maximum velocity at each plane was plotted against  $x/D$  and normalized by the overall maximum velocity.

Figure 25a & 25b shows the calculated uncertainty associated with the current study's method of obtaining flow rate. The details for this calculation are in shown in Appendix F.

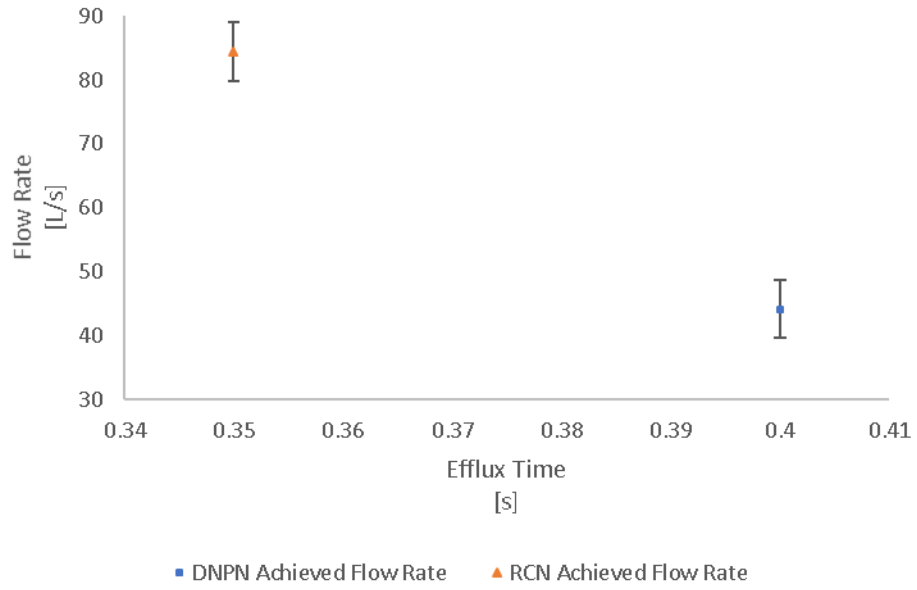


**Figure 25a: Calculated Flow Rate Uncertainty for 95% Confidence Interval**

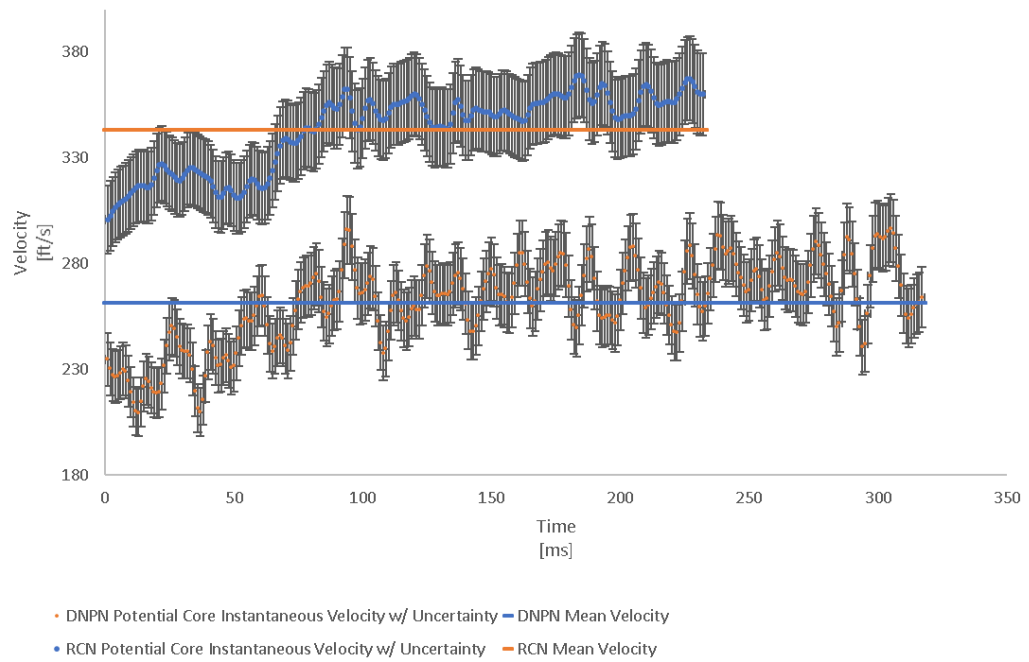


**Figure 25b: Calculated Velocity Uncertainty for 95% Confidence Interval**

### *Flow Visualization/Instantaneous Velocity with PIV*

To validate the transducer velocity measurements PIV is used as a second method to observe the blowfield. These data give insights to both qualitative and quantitative characteristics of a flow-field using optical sensors to observe a two-dimensional plane of fluid and a Fast Fourier Transform (FFT) algorithm to post-process the images in form of particle displacement. The two-dimensional time-resolved PIV was conducted using a single high-speed CMOS camera. This camera had a spatial resolution of 1280 x 800 pixels, maximum frame rate of 5000 frames per second at full resolution, and a pixel size of 20 x 20 micrometers. An AF Nikkor 50mm/1.4D lens was attached to the camera, and its aperture was set to 1.4. An Nd:YLF single cavity diode pumped solid state laser (527 nm wavelength) with 1 kHz maximum repetition rate and 0.5 mm beam so diameter was used as the illumination source. The beam was passed through a diverging-converging lens combination and a horizontal laser sheet of ~3 mm in thickness was developed using a 10 mm focal-length cylindrical lens. Black Diamond© uncut chalk of variable diameter and fine water mist were used as seeding particles suspended in air; the seeding tube shown in Figure 14 is responsible for injecting fluid into the flow and the chalk was added into the orifice of the nozzles and sucked into ChuffSim by manually pulling the baseplate from BDC to TDC. Homogeneous seeding was not obtained during testing which lead to insufficiently resolved PIV sessions. Particle sizes produced by the misting nozzles in the seeding tube ranged from 30-100  $\mu\text{m}$  where chalk particles fell in a range of 50-8000  $\mu\text{m}$ . Finally, the camera and laser were controlled by a high-speed controller and were connected to a computer utilizing LaVision's DaVis 8.3.0 software for frame-grabbing purpose. PIV image acquisition was triggered via operator due to ChuffSim's inability to trigger autonomously (through switch thrown by operator). A diagram of the connectivity between these components is shown in Figure 26. The data was analyzed in both MATLAB using the PIVlab toolbox and DaVis.

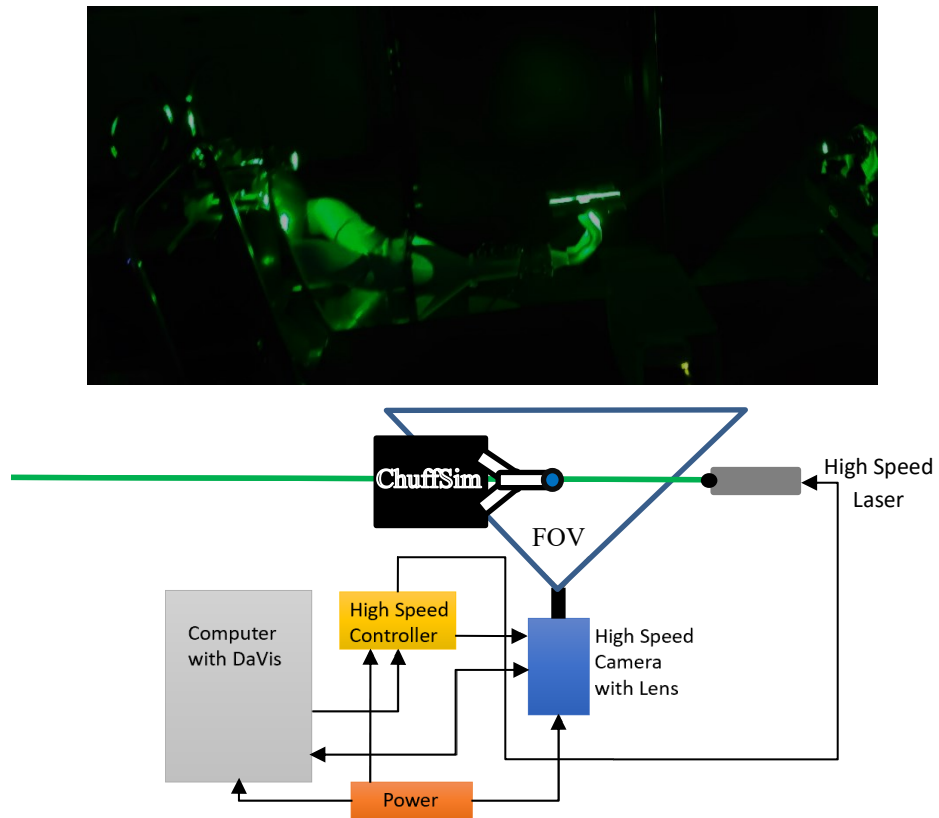


**Figure 26: PIV acquisition set-up**

*Dolphin In-Situ PIV*

Comparison of the simulated dolphin chuff is made with In-Situ PIV measurements made on actual dolphin under human care. These tests were conducted at Dolphin Quest© of Bermuda where dolphins allowed researchers to observe forceful breaths while recording with a high-speed camera. The high-speed CMOS Phantom camera and AF Nikkor 50mm/1.4D lens used during the ChuffSim PIV were also used in Bermuda. To film the extent of the chuffs without a laser and high-speed controller the native PCC software was used to trigger and capture the impulsive jets. An acrylic box was constructed to protect the high-speed camera while on the docks during recording. A Toughbook (Panasonic, Tokyo, Japan) laptop was used to control the PCC camera software.

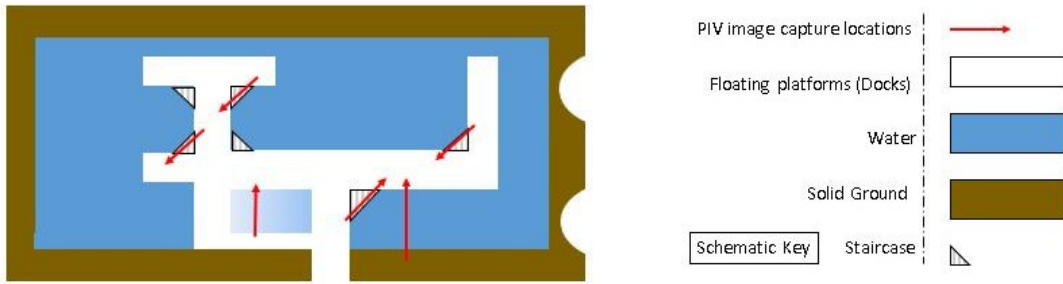


**Figure 27: Top View of Dolphin Quest Dockyard [28]**

Acquiring good quality videos in this humid environment on live animals is far from trivial. Figures 27 & 28 show an aerial view of the docks that the In-Situ PIV took place. To make things more difficult these tests took place during normal Dolphin Quest operation which involves Dolphin Trainers feeding, instructing dolphins, and helping guests interact with the animals willing to participate in activities.

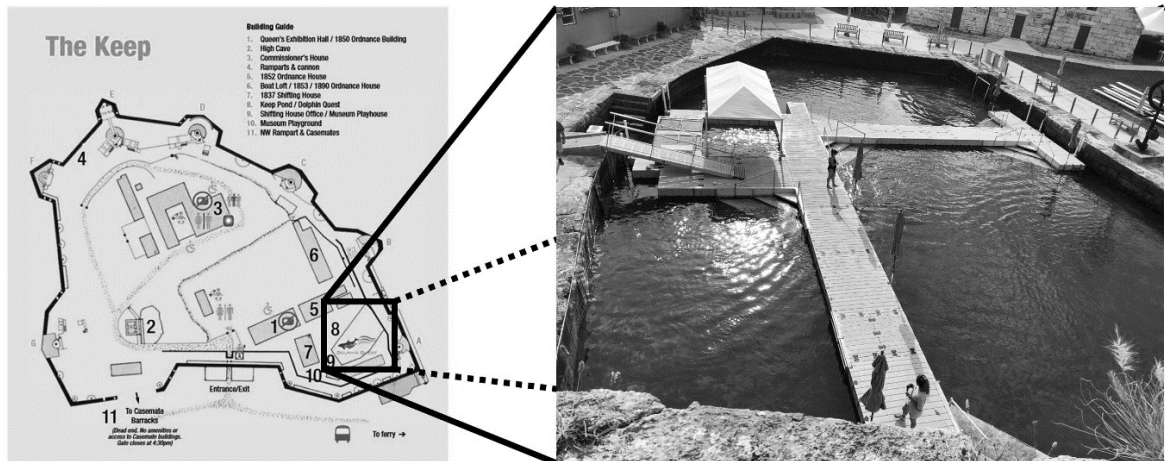


**Figure 28: Dolphin Quest Bermuda Dockyards [28]**

Because of these testing obstacles only two or three windows were available for testing each day: before Dolphin Quest opened, during lunch, and after operating hours. The first procedure was for an operator to focus the camera on a dolphin fan while inside the acrylic box and calibrate the field of view. This didn't guarantee accuracy since the dolphins still moved

slightly due to its imbalance on the platform. Figure 29 illustrates the camera placed normal to the dolphin's blowhole (~10 ft away). Two people held a black backdrop to increase the contrast of the shot in natural lighting. In addition, the backdrop also contained a calibration reference for PIV post-processing. Next a trigger was set on the PCC application to account for reaction time of logistics in the test plan. The frame rate used 4500 frames per second to insure proper particle displacement in the image pairs. It was anticipated with the ~140 liters/second would lead to potential-core velocities upwards of ~650 ft/s in theory. The operator of the camera initiates recording, the signal was then asked of the trainer to prompt the dolphin to chuff. After the chuff was completed the operator trims the video and then all personnel cleared the dock.

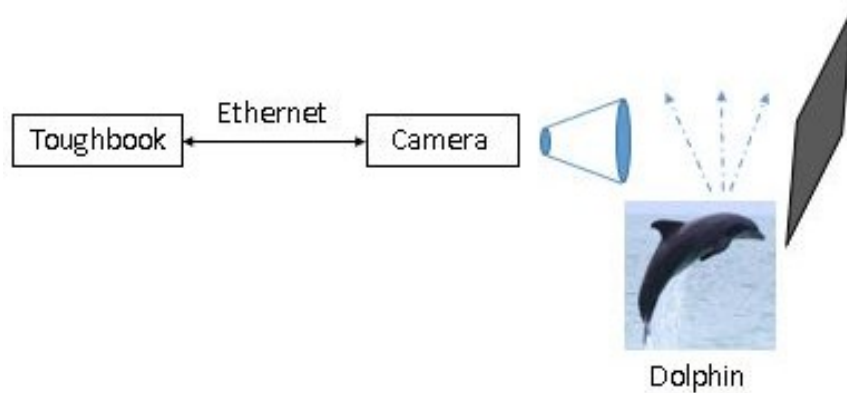


**Figure 29: Dock-Side PIV set-up [28]**

The three dolphins willing to participate in this study were Cooper (male-9), Caliban (female-26), and Cirrus (female-45). More information on these animals are available in Appendix E, Figure E1 [28].

The field of view shown in Figure 30 represents the field of view from the best resolved frames from each of the matrices (~16" x ~30").

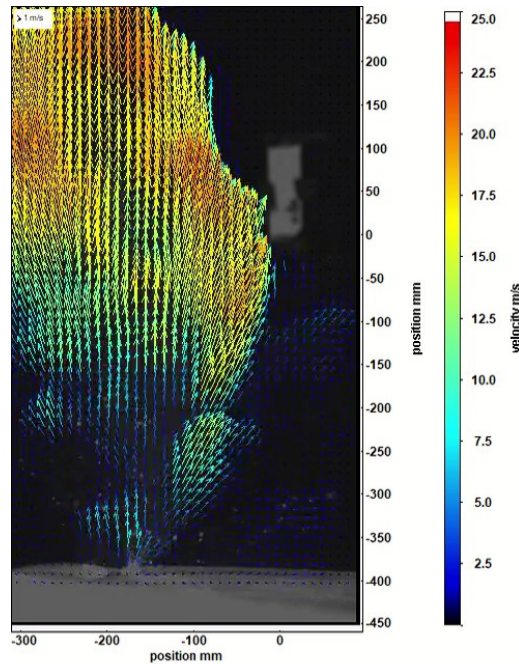


**Figure 30: In-Situ PIV Field of View from Caliban @ 4500 fps**

In this image it can be noted that the head of the dolphin is out of the FOV to the left while the tail is off to the right. All of the most successfully resolved videos for the three participants used a PIV time series, adaptive 32x32, 24x24, 50% overlap, 2 passes FFT software used to process the ChuffSim PIV data. The resolved data from Caliban's, Cooper's, and Cirrus's data showed a maximum velocity of 88, 88, and 72 feet per second respectively. The resolved PIV also did not show a trend consistent with jet theory. The exit from the blowhole did not have the highest velocity nor did the core seem present in the flow. This was most likely caused from capturing the full three-dimensional blowfield from the lack of a laser plane. Another contributing factor was the high concentration of particles near the blowhole's exit prevented Davis (Lavision's Software) from validating vectors.



Nevertheless, these data are still helpful in qualitatively defining characteristics in the extent of the dolphin's impulsive jet. The ChuffSim device was sized using data from that showed Atlantic bottlenose dolphin had a maximum expiration rate of ~140 liters/second. In order to observe the flowrate for a longer duration the simulator volume was oversized (~47 liters) [13].

### *Laboratory Flow Visualization*

The qualitative flow visualization used the same Phantom camera as in the Bermuda and ChuffSim PIV studies. The frame rate of this films was 2500 fps with a field of view of 12 (y/D) x 10 (x/D) using the same PCC software used in Bermuda. The videos were trimmed in the same manner as the Bermuda study; all videos were recorded in 3840 x 2160p resolution. The starboard-side and the head-side plane were the two different angles utilized. Crushed chalk was used as seeding, for each take ¼ of a cup of chalk was added into the orifice and manually sucked into the device by the user pulling the base plate from BDC to TDC to evenly mix the chalk throughout the device.

The second set of extent videos used the Samsung Galaxy S9 camera for a larger field of view at an isometric-angle of 45 degrees offset between the starboard plane and the tail-side plane. The frame rate of this camera is ~960 fps possible with the rolling shutter on this phone with a FOV of 26 (y-z/D) x 50 (x/D). The resolution is limited to 720 x 1080p in this high frame rate mode and can only record ~0.4 seconds of video in real-time. The videos were initiated using an on-screen trigger that initiates when it detects movement in a user-defined area in the FOV.

### *Blowfield Splatter Tests*

The last portion of experimental work is the splatter tests conducted on both nozzle geometries. The study consisted of black poster boards with adhesive being held 4 feet above (by two-people) each nozzle during a chuff to obtain a cross-section of the static flow (no cross-flow).



**Figure 31: Splatter Test Example**

The seeding used for visualization on the board was blue glitter for the best contrast. The seeding method is similar to that of the flow visualization videos. Figure 31 shows how each of the splatter tests were conducted. All operators wore N95 masks to ensure safety during all tests.

## CHAPTER IV

### RESULTS & DISCUSSION

#### *Velocity Data*

To quantify the blowfield above the RCN and the DNPN a grid survey was conducted with a pressure probe in planes ranging from  $x/D = 0-4$  diameters. Both nozzles have a diameter of 30mm (1.18in) with a 90-degree bend in relation to the pistons orientation making it analogous to a dolphin's respiratory system layout as shown in Figure 14 in Chapter 3. The two-dimensional velocity-fields are illustrated in Figure 32 for the RCN (left) and DNPN (right) in a three-dimensional format using MATLAB's CurveFit tool. The CurveFit tool used a linear interpolation method to obtain the topographical planes shown.

The RCN blowfield has a classical top hat profile typical of axis-symmetric jets, the peak velocity shown for the potential core is  $\sim 380$  ft/s at a peak flowrate of 79 liters/s. The core length spans outwards to approximately 3.5 diameters downstream. This is illustrated in Figure\_ which shows the comparison of normalized velocity decay versus the normalized x-axis (axial direction). The Dolphin Nasal Passage blowfield is reminiscent of a well-mixed jet as indicated by the rapid decay of velocity in the near-field. The DNPN peak potential-core velocity is  $\sim 282$  ft/s at a flowrate of 39 liters/s.

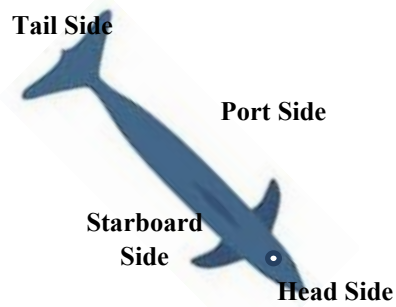
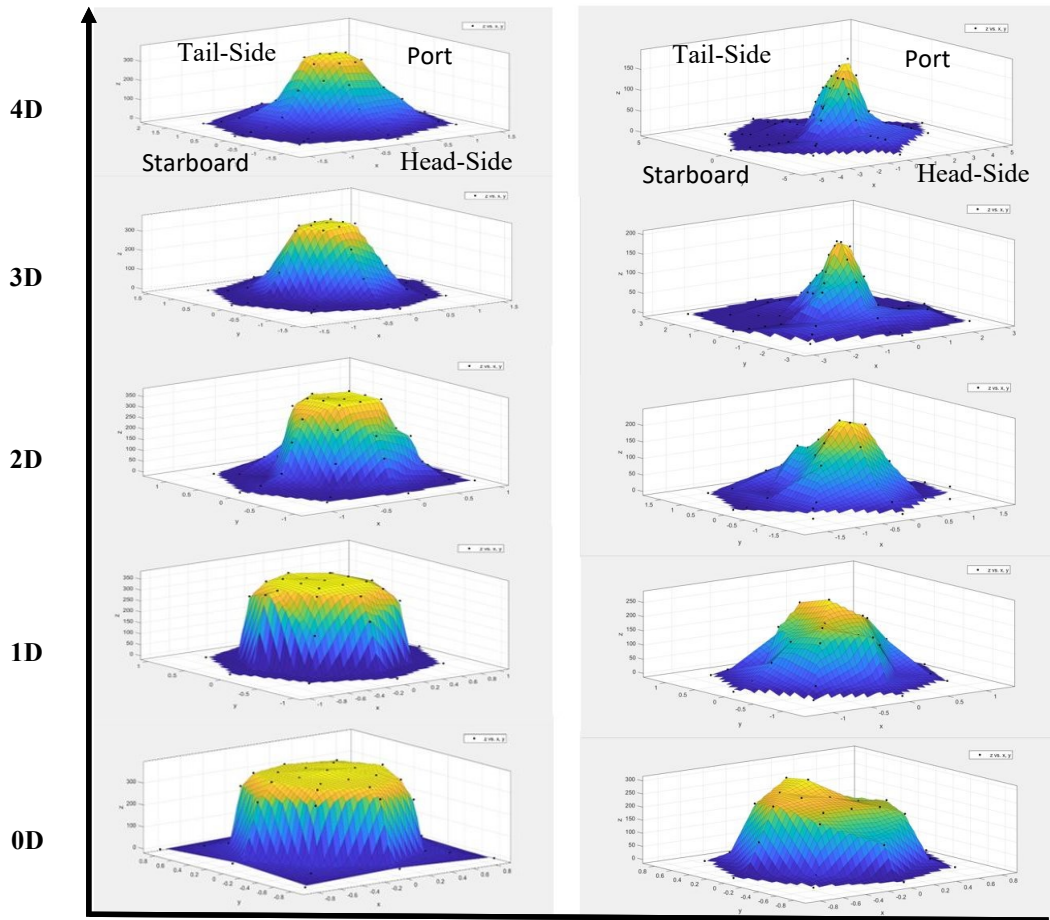


**Figure 32: Control Nozzle versus Dolphin Nasal Passage Velocity Evolution for  $x/D = 0-4$**

The three-dimensional representation of the DNPN velocity contour across  $x/D$  planes 0 - 4 indicate that the peak velocity evolves from the tail-side/leeward-side at  $x/D = 0$  to the head-

side/windward-side at  $x/D = 4$ . This is most likely the consequence of the 90-degree bend due to the fluid's momentum being conserved in the original direction of motion. This observed velocity evolution from the tail-side to the head-side is not reciprocated by the RCN. This is supported in the extent videos shown later in the discussion section. The DNPN potential core exists for approximately 1 diameter where it steeply decays in comparison to the Control Nozzle in Figure 33.

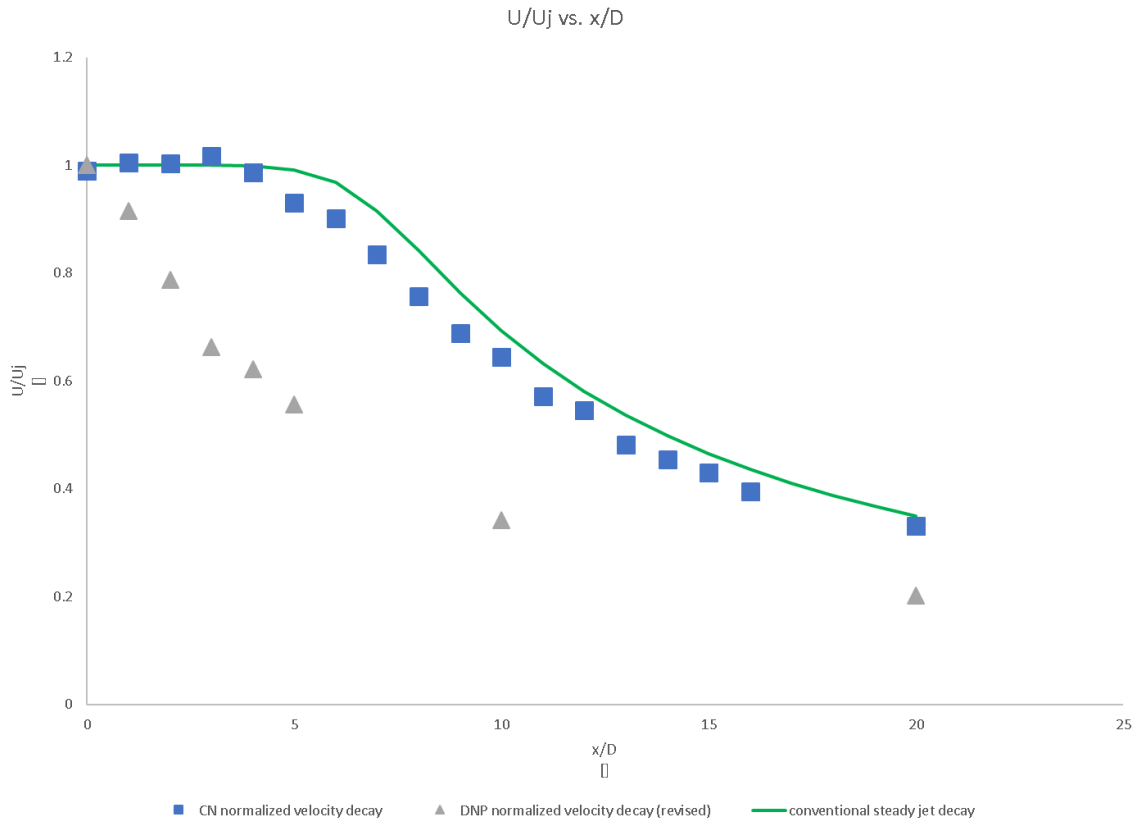
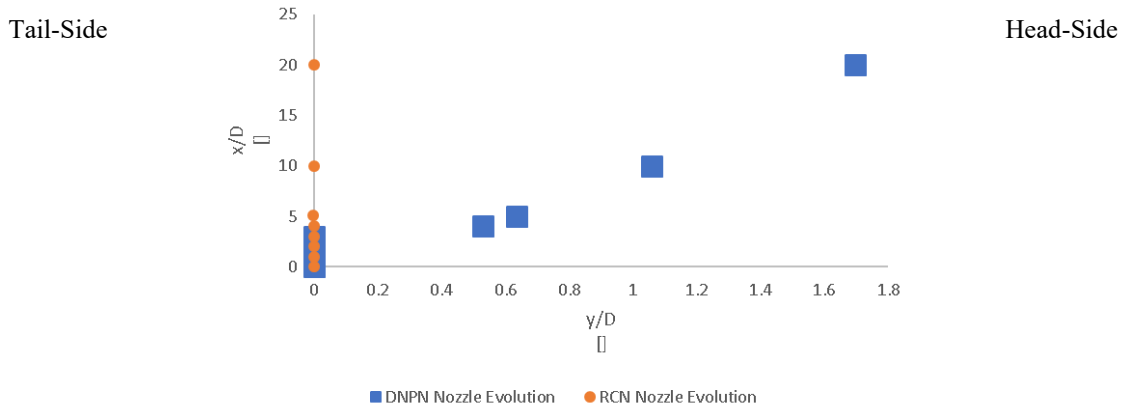


**Figure 33: Normalized Velocity Decay versus  $x/D$  [14]**

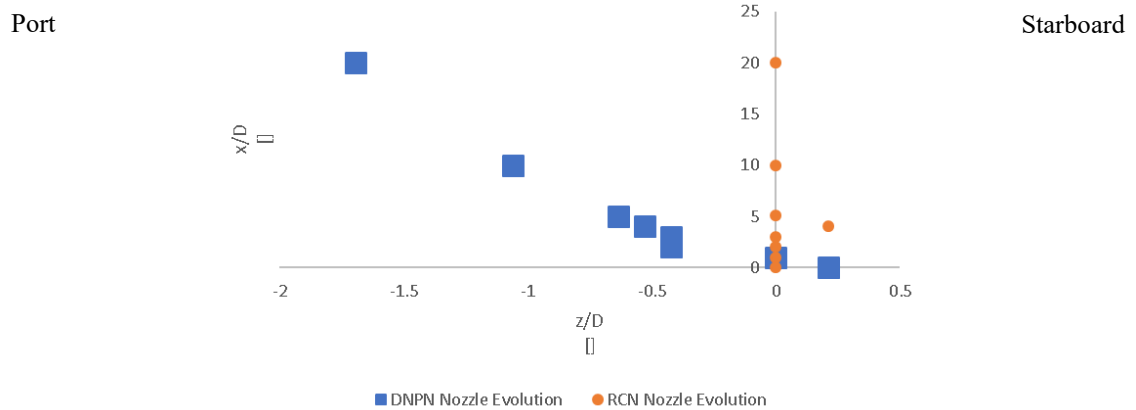
The velocity decay survey for the RCN was trivial in comparison to the DNPN, the quasi-grid-survey that was conducted to determine the location of the max plane velocity was not necessary for most  $x/D$ 's. The line plotted represents work done by VonGlahn (1984) where the jet decay is represented by the empirical formula shown below:

$$\frac{U}{U_j} = \left[ 1 + \left( \frac{x}{6D(1 + M_j)^{0.5}} \right)^8 \left( \frac{T_j}{T_0} \right)^2 \right]^{-0.125}$$

Where  $\frac{T_j}{T_0} = 0.99$  and  $M_j = 0.345$  for the line plotted, this trend follows very closely to the RCN showing that an impulsively started conventional nozzle behaves similarly to a steady conventional nozzle. The max axial plane velocity occurred at the origin with a spatial standard deviation of  $\pm 0.125$  inches in both the y & z axes. Figure 34a & 34b shows a plot representing the location of the max plane velocity obtained during the quasi-grid-survey conducted. Figure 34a depicts the DNPN velocity biasing toward the dolphin head-side while Figure 34b shows the blowfield biasing towards the port-side of the dolphin.



(a)



(b)

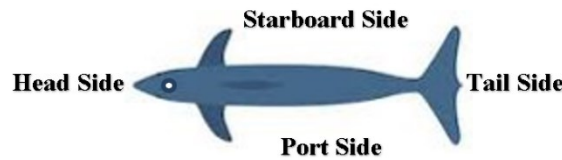


**Figure 34: Normalized  $x/D$  versus Normalized  $y/D$  (a) &  $z/D$  (b) Position of Max Plane Velocity**

The trend from Figure 34a is not surprising since the overall jet movement towards the head-side was predicted from the 90-degree bend. Figure 34b's trend is speculated to be from the artificially CAD-made orifice impeding the port-side nasal passage more than the starboard-side nasal passage. The orifice of the DNP is supposed to be analogous to the blowhole of a dolphin which was found to be more oval shaped rather than perfectly circular. This was determined post experimentation and will be implemented in the future work. Figure 36 shows the average shape of a Bottlenose Dolphin blowhole, the oval shape is biased in width from port to starboard to accommodate for the nasal passages joining back together after splitting.

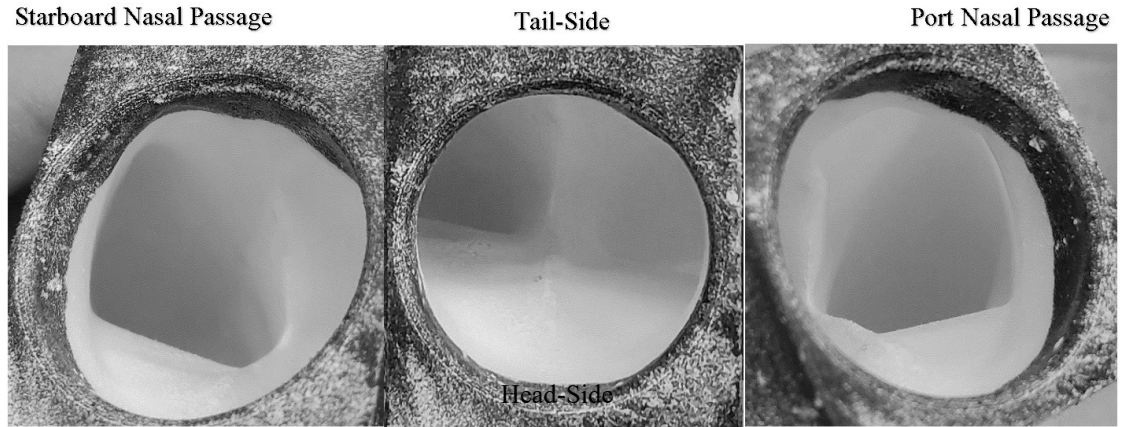


**Figure 35: Detailed View of DNPN Orifice**

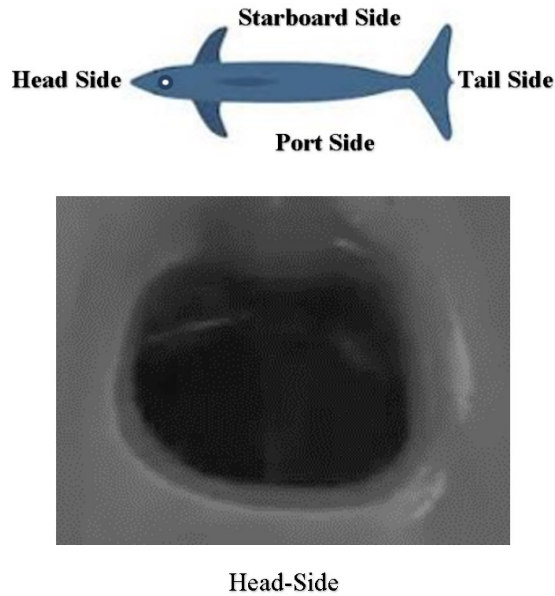


**Figure 36: Dolphin Blowhole Shape [9]**

The blockage effect of the artificially made orifice is better described in Figure 37 where the image shows the starboard and port side nasal passages and their respective flow vectors. The port-side vector is visually more obstructed than the starboard-side vector with respect to the direction of each mean flow. In other words, the port-side vector is impeded by the exit lip of the orifice where the starboard vector does not. This is speculated to result with the trend illustrated in Figure 37b because the starboard-side nasal vector is going to influence the port-side of the



blowfield and vice versa for the port-side nasal vector. Subsequently, the head and tail side nasal passages both follow a similar streamline line directing the flow vector as shown in Figure 37. While the nasal passages are not perfectly symmetric they do give insight to how the fluid behaves when isolating the flow in the z-plane. The non-isotropy of the DNPN plume may be arbitrary in this case, however, it is very likely that a dolphin in real life will have a random skew to its chuffs as well. The direction of flow in this plane is supported later in the flow visualization sections for Extent Filming and PIV realizations. Changing the orifice exit geometry will effectively change the extent of the jet and therefore the velocity evolution profile. For the purpose of characterizing this special impulsive jet the data obtained with the perfectly round orifice will suffice for a general understanding of the mechanics. For future work it is recommended that the CAD geometry of the DNPN is altered to more adequately represent a dolphin's blowhole.

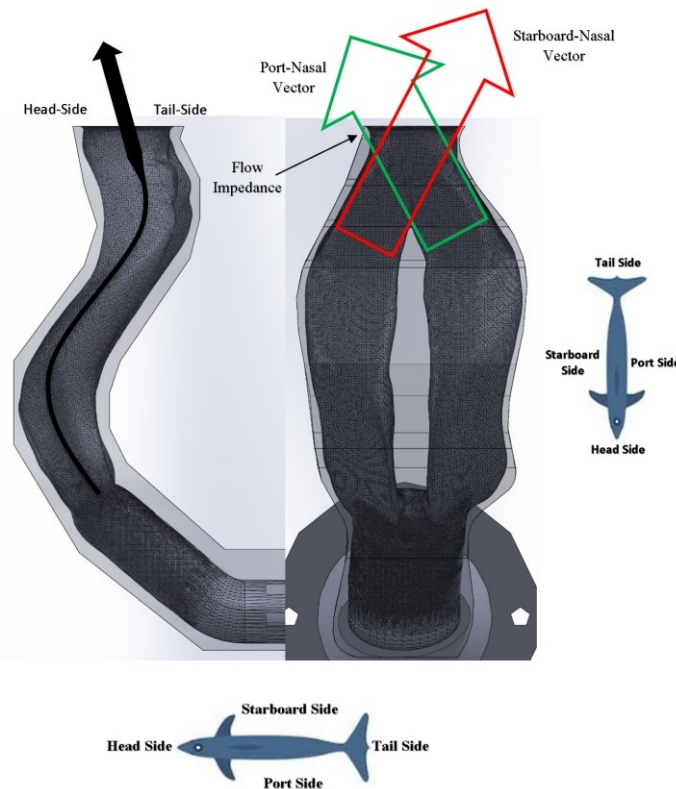
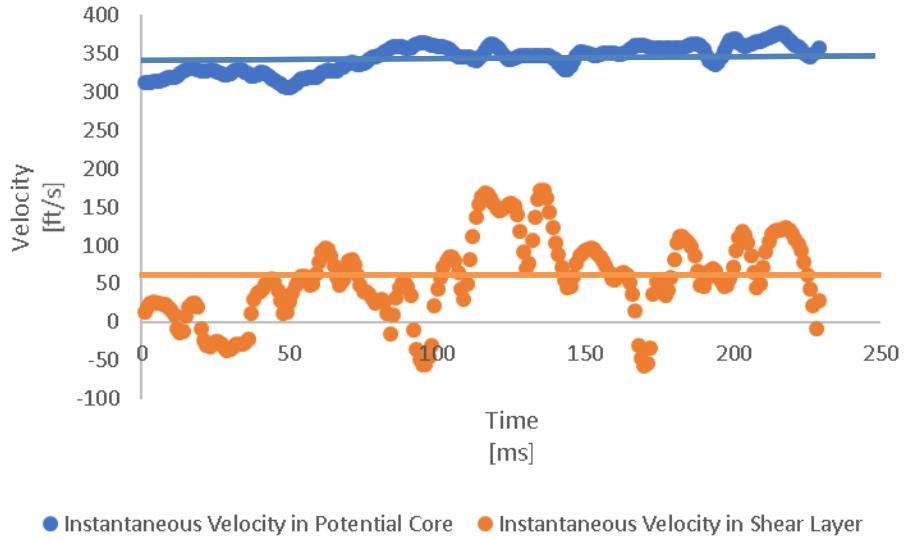
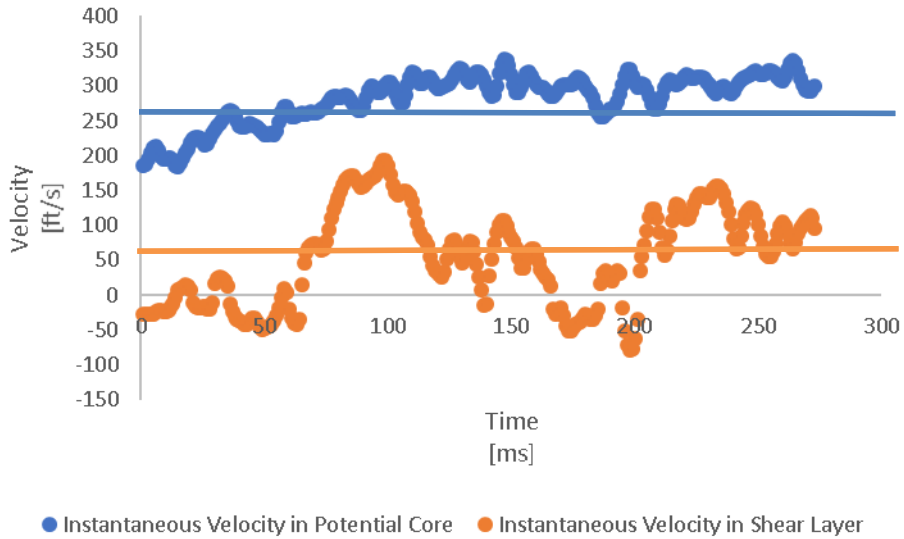


**Figure 37: DNPN SolidWorks CAD with Free-Handed Flow-Vectors**

*Turbulence Intensity Data*



(a)



(b)

**Figure 38: Mean Velocity in Potential Core vs. Mean Velocity in Shear Layer for RCN (a) & DNP (b)**

The Endevco unsteady-instantaneous-pressure transducer allowed the capability to perform a turbulence intensity study from its ability to document discrete time dependent velocity



The first observation of these data was the turbulence intensity for both the DNP and RCN were much greater than 1 (100%) along the y and z planes where the velocity is very small moving towards the edge of each velocity profile. This is because turbulence intensity is defined as the turbulence strength ( $U_{rms}$ ) divided by the mean velocity ( $\bar{u}$ ) and when the mean velocity reaches a value less than 1 at a discrete point in the shear-layer where the perturbations of velocity are large ( $U_{rms}$ ) the turbulence intensity becomes very large. It is statistically possible to obtain a value greater than 1 since in theory the perturbations of velocity are not actually random. This does not validate the trends displayed, in some cases there are only one or two outlier points that suggest the turbulence is very high. For instance, Figure 40b indicates the turbulence intensity is greater than 500 % on the head-side of the RCN @  $y/D = -0.85$  where the normalized mean velocity = 0.013. While the calculated value is correctly derived the single point does not necessarily represent the turbulence trend of the figure as a whole.

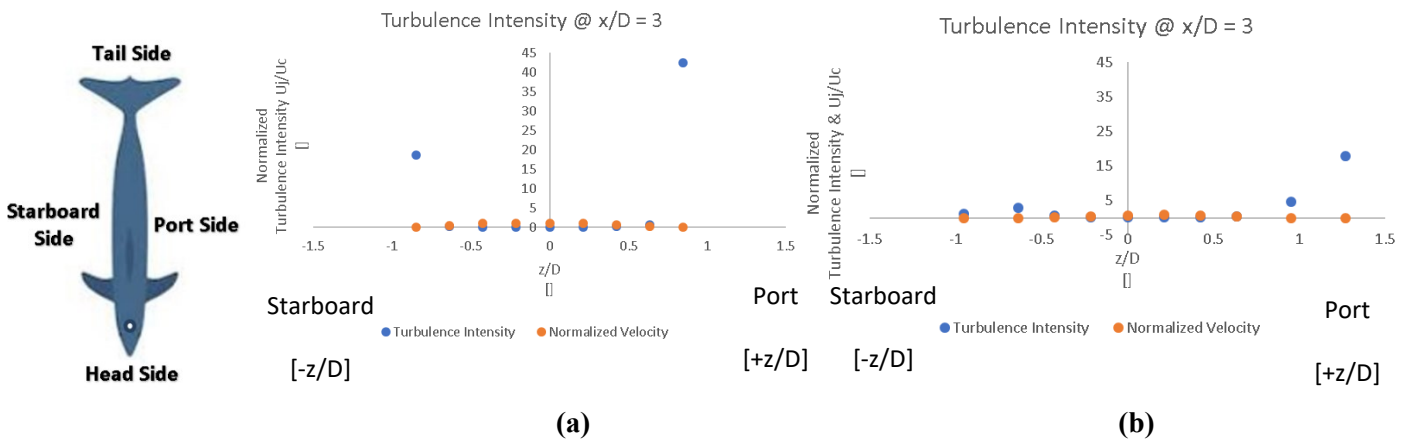


**Figure 40: Y-plane Turbulence Intensity plots RCN (a) & DNP (b) @  $x/D = 3$**

This is the same case for both the DNP and RCN in the y-plane where the turbulence intensity reaches as high as 20,000-45,000 % towards the edge of the velocity profile. These values are so high that the normalized velocity profile is intangible with respect to the turbulence intensities plotted.

The lack of integrity from these data may indicate that not enough points were used to form the velocity profiles from the grid-survey. This was mainly due to the overall motion of the ChuffSim device while performing an artificial chuff where the nozzle would move  $\sim\pm 0.1$  inches with respect to the probe position. From this motion the smallest increment from one-point to another never exceeded 0.125 inches making it difficult to characterize the shear-layer, hence, the inadequate representation of shear character in the lower planes ( $x/D = 0-2$ ).

*Self-Similarity Plots*

Along the path to the classical method of jet characterization the next step was to conduct a self-similarity study. The profiles are made-up of normalized mean velocity points with respect to non-dimensional  $y/D$  and  $z/D$  positions. Both the  $y$  &  $z$  plane plots in Figure 41a and Figure 42a show typical axisymmetric jet self-similar profiles with no discernible bias in either axis.

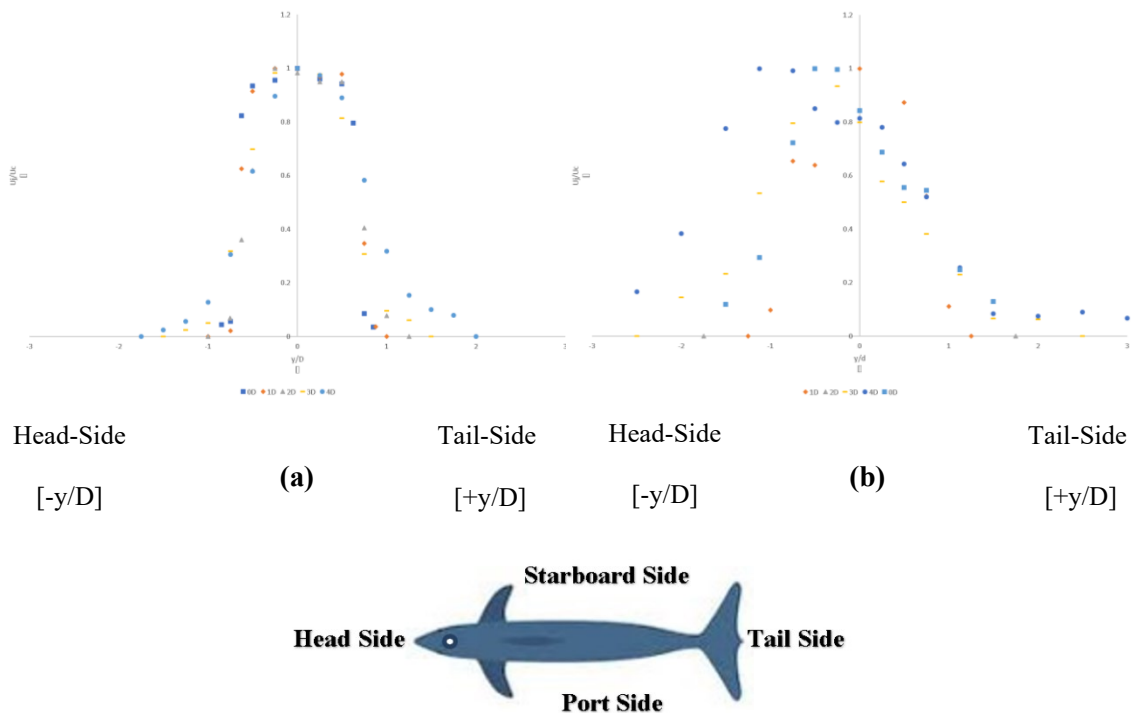


**Figure 41: Z-plane Self-Similarity plots RCN (a) & DNP (b) for  $x/D = 0-4$**

This shows that an impulsive axis-symmetric jet still follows similar trends to steady-jets and is supported by the qualitative videos taken from the extent of this nozzle. The DNP Figure 41b & Figure 42b shows the normalized velocities trending in the head-side and port-side supporting a greater transport of momentum in these directions.

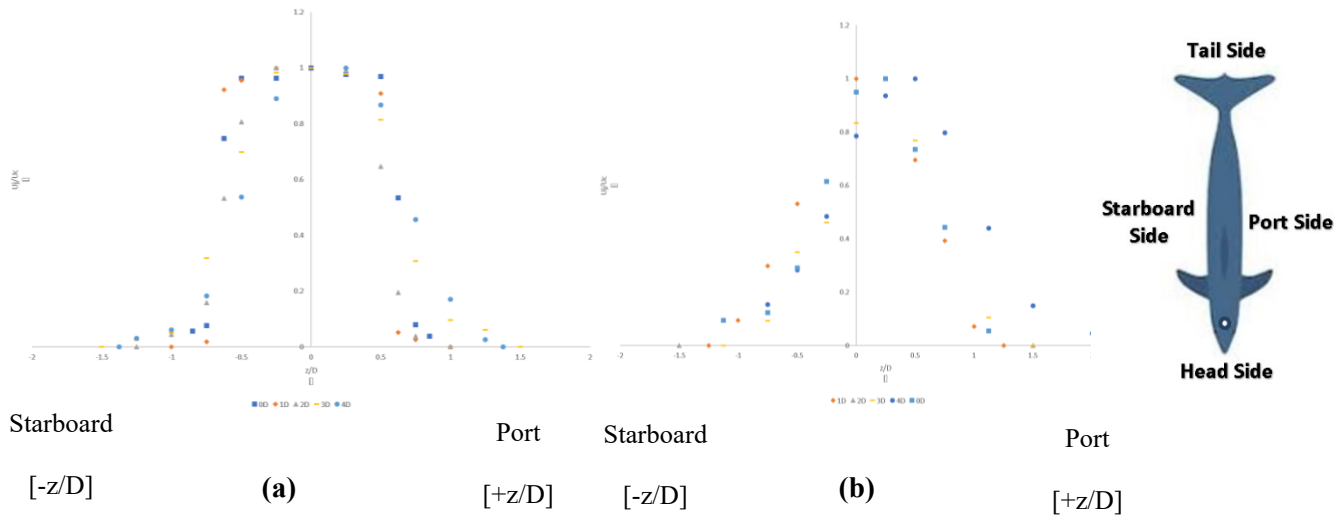


**Figure 42: Y-plane Self-Similarity plots RCN (a) & DNP (b) for  $x/D = 0-4$**

Earlier, the blockage effect was hypothesized as the reason for the port-side bias while the 90-degree bend explained the dolphin head-side bias of velocity observed in these two planes. The blockage effect is assumed to be from human error while the head-side/wind-side bias is going to be present in the flow from dolphins' innate respiratory geometry.

#### *ChuffSim PIV Data*

The pressure transducer data was validated from ChuffSim using PIV, Figure 43 shows sequential frames taken from the best time-resolved data set. The graphs above these images are the velocity profiles taken at  $x/D = 3$  where the blue corresponds to the instantaneous velocity in

this plane and the static red curve represents the average-velocity captured by the unsteady pressure transducer at  $x/D = 3$ .

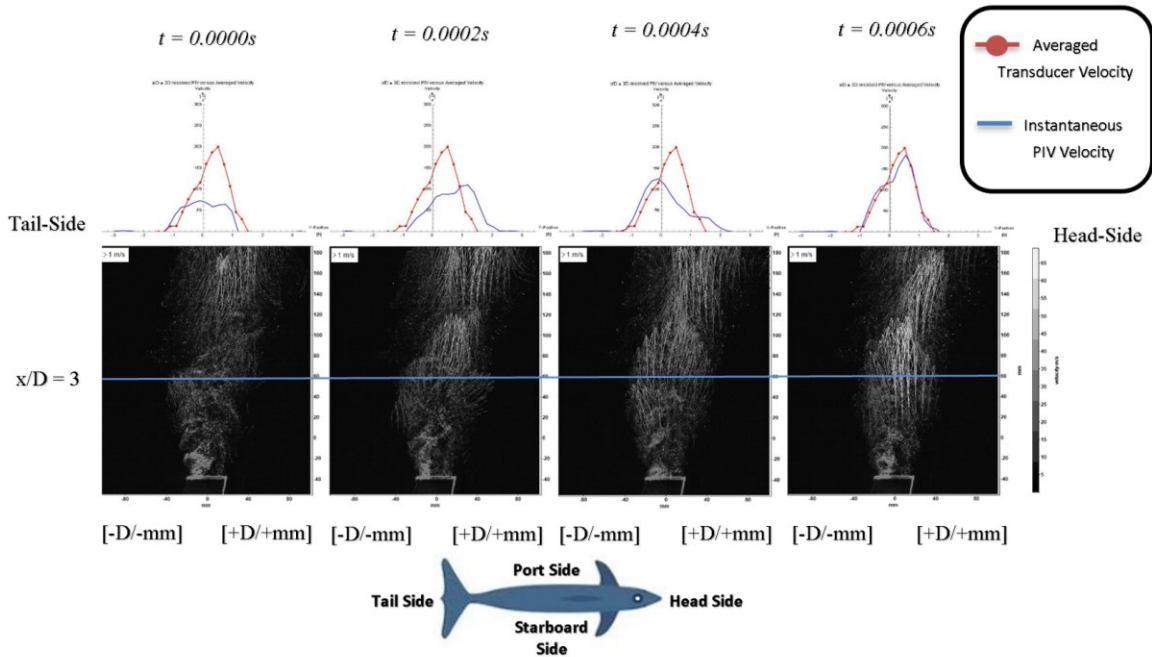


**Figure 43: DNPV Instantaneous PIV comparison to Averaged Unsteady Pressure Transducer Velocity (top) Time-Resolved Instantaneous PIV (bottom)**

The blue line represents where the velocity data is taken from with respect to the field of view.

This sequence shows a portion of the PIV data sets that were partially resolved from the sufficient intermittent seeding. One of the largest differences between the pressure transducer and PIV data was that the PIV data represents multiphase flow (fine water particles and chalk entrained in air) while the transducer only surveyed single-phase flow (air). Nonetheless, these data provide validation for the transducer measurements from approximately 800 frames that are semi-resolved. In addition, the PIV also provide observations of fluid-structures in the blowfield much like in the extent videos but with a smaller field of view. In the future, the use of background-oriented schlieren (BOS) imaging is recommended since seeding proved to be nontrivial for the PIV. The particles clump together at the orifice creating too-much noise for resolving the potential core where the particle displacement is the greatest in the blowfield.

### *Flow Visualization*

Impulsive blowfields are a newly studied concept in the field of fluid mechanics. While they may follow similar characteristics of forceful human respiratory functions, the observed flow rates from dolphin chuffs are on an order of magnitude ten times higher than that of a human's. Because of this, it is important to document the discrepancies qualitatively between blowfields and other jets of this nature. It can be noted that the seeding in these tests were non-isotropic from start to end of a chuff, hence, the disparity between the DNPN starboard and head-side extent is because they are taken from different instances in the chuff that best describe their character. The total quantity of chalk added to each flow was the same in each nozzle case.

The control nozzle forms a directive and highly concentrated plume at the initiation of the chuff. The dolphin nasal passage forms a wider plume with visibly more fine and large-scale turbulence in the fully developed portion of the extent. In the RCN starboard-side view noticeably more mass is concentrated towards the head-side indicated by the lighter contrast on the right side of the image. However, the plume of jet maintains itself in the middle of the field of view suggesting no bias from the 90-degree bend. On the contrary, the DNPN plume is shifted as a result of the bend as supported earlier. This is also shown in the Bermuda PIV snapshot back in the experimental section (Figure 44) where the blowfield follows this head-wise trend. Toroidal vortices are observed to form as they roll-up the shear-layer from the base of the jet.



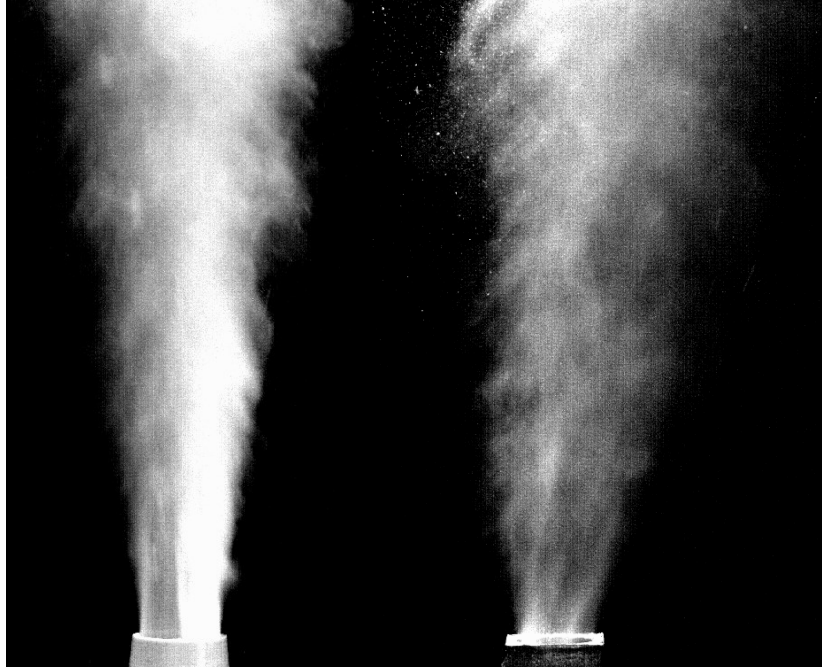


**Figure 44: RCN (left) & DNP (right) Starboard-Side Extent**



This is observed for both the DNP and RCN in both planes illustrated in Figures 44 & 45 but much more prevalent in the actual videos. While the vortex pairing is evident in both planes it is best portrayed in the Head-Side plane where the blowfield tends to have more symmetry. The well-mixed nature of the DNP is best shown in this plane where the extent is much wider than the RCN's.

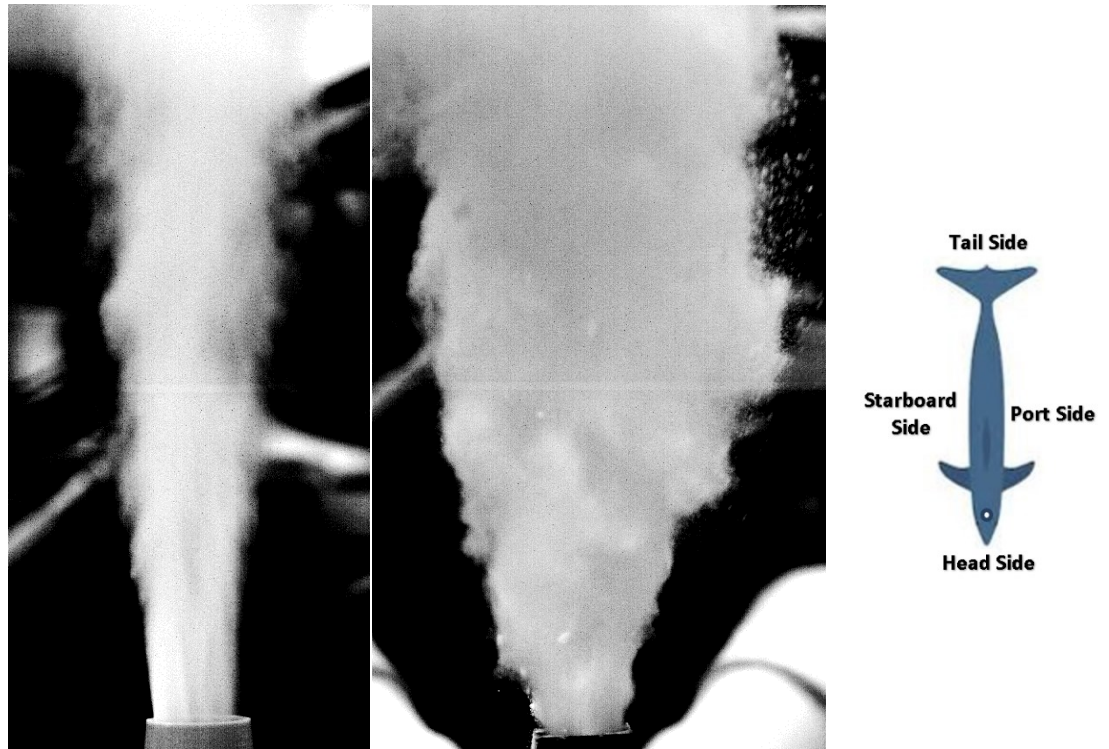


**Figure 45: RCN (left) & DNP (right) Head-Side Extent**

Throughout the duration of these impulsive jets both geometries exhibit a quasi-steady state as long as the piston is moving. If the seeding is adequate it is possible to see the starting vortex at the impulsive start, the vortex ring propagates downstream at a higher speed than the jet-tip as supported by Witze et Al. and Abramovich & Solan where it was observed that all impulsively started jets shared this characteristic. The speed difference is speculated to be from the vortex rings' marginal mass-entrainment in comparison to the jet tip's entrainment as it travels downstream. The spreading rate of these jets is shown to be greater than a conventional jet from their higher entrainment rates. The greater entrainment rate decreases the axial velocity faster than steady jets as well which adds to the difficulty of the overall problem of capturing mucus.

### *Blowfield Splatter Results*

To tie back to the motivation of designing a UAS capable of capturing the fluid efflux from these plumes, it is useful knowledge to know how large the target available to the drone is in addition to the depth of penetration. This will help in quantifying the margin of error the system will be operating in while tracking and surveying multiple blowfields within a pod. To quantify this area a splatter test was conducted to analyze the radius evolution in the far-field to estimate the static-jet cross-section greater than 4 feet above the nozzle. Due to the constraint of the facility's low ceiling (~10 ft) and difficulty trapping particles on the poster-board these tests were only conducted at a height of 4 feet.

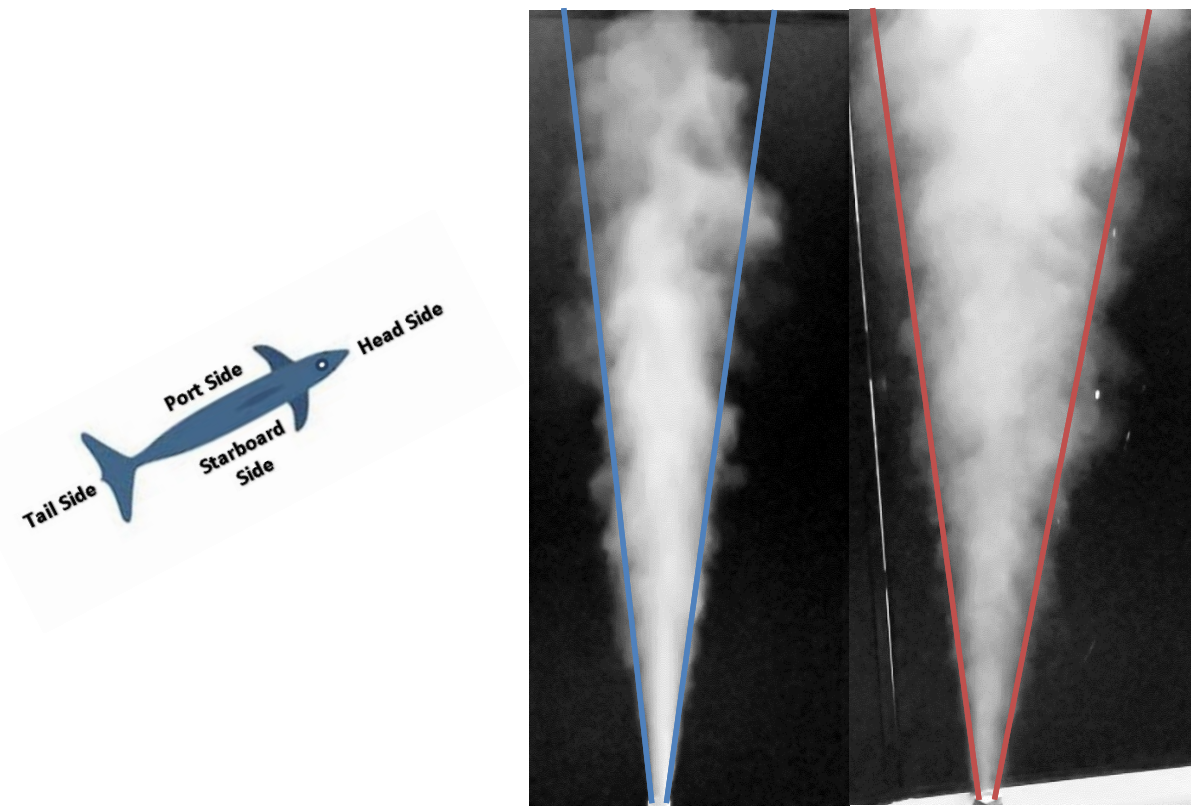


**Figure 46: RCN (a) & DNP (b) Extent Larger FOV**

Figure 46 shows the larger field of view of both the RCN and DNP extents at a third angle, the lines on these images give an idea how wide the mean radius of each splatter will be.

Note that this is assuming the dolphin is stationary while performing a chuff and the penetration and cross-sectional area of the jet wake is subject to change with an additional cross-wind boundary condition.

Figure 47 illustrates the cross section of each impulsive jet 4 feet above the nozzle. Using the MATLAB application PIVlab each image was calibrated with a known length and the radius was measured in three different axes and averaged. The directivity of the RCN is shown in the left image of Figure 47 where the glitter is highly concentration towards the center of the cross-section of the splatter. The DNPN splatter shows the wider spread of glitter across the cross-section with less visible particulates. This is speculated to be from the adhesives inability to capture particles at lower pressure gradients which is to be expected from a well-mixed jet.

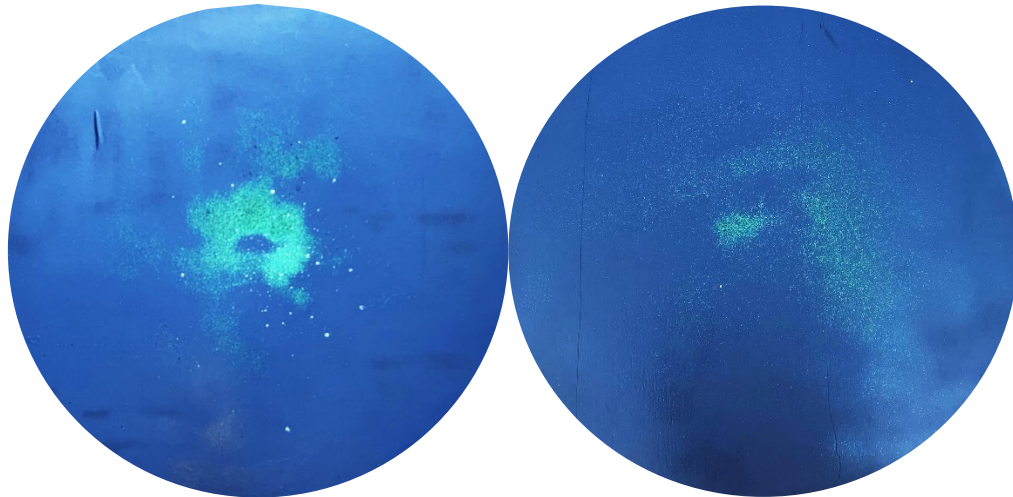


**Figure 47: Splatter Tests 4 feet above RCN (left) and DNPN (right)]**

The radius of the RCN splatter was found to be 3 inches at 4 feet while the DNPN's radius was 9 inches. The white splatters on the RCN test are chalk leftover from the flow visualization videos and are approximately 2-3mm in size. Next, videos of the extent hitting the ceiling were also taken and measured in MATLAB application PIVlab using the measurement and calibration tool. Appendix D, Figure D1 shows the frames selected to measure the cross-section at the facility

ceiling for both nozzle geometries. The measured radii for the RCN and DNPN at 10 feet were 17 inches and 20 inches respectively. Using these data points a plot was made to approximate the radius at different heights.

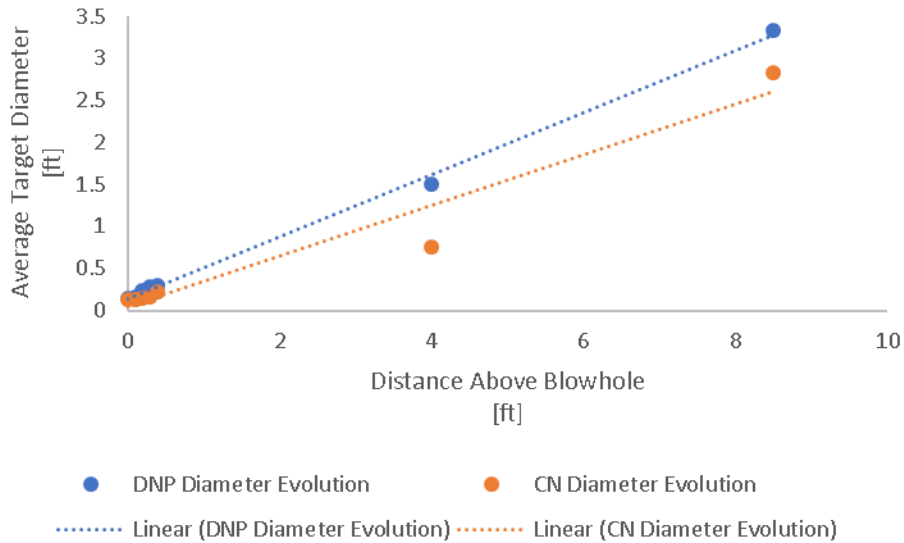


**Figure 48: Diameter Evolution versus x-axis for DNPN & RCN**

The data points clustered towards the left side of the Figure 48 correspond to averaged measured radii from the grid-survey study. The trend for the DNPN radius evolution is shown as a relatively close approximation when adding the 4 ft splatter and ceiling impact data points. While the RCN impact radius measured at the ceiling matches the overall trend the outlier in this data set is the splatter radius measured at 4 feet. The trend still suggests a faster spreading rate from the DNPN when compared to the RCN, it also suggests that statically the DNPN chuff has the ability to penetrate the ceiling of the facility at 10 feet. This is a promising finding since the flowrate studied (44.1-80.4 liters/second) is approximately half of the maximum flow rate achieved in literature (~140 liters/s).

### *Comparison of Respiratory Data*

Existing flow rate data from dolphins blowfields were obtained in a study conducted by Andreas Fahlman et. Al (2015) using a special pneumotachometer. The pneumotachometer has a special orifice to adapt to the curvature of a dolphin's head to mitigate fluid leaks. Appendix C, Figure C3 shows how the test setup was used to acquire these data.

The instantaneous flowrate versus time of a maximal respiratory effort (chuff) in the Andreas study is shown below in Figure 49 where the flow rate peak takes the shape of an impulse biased towards the negative slope (right). In this study data from 163 spontaneous breaths and 45 maximal effort breaths (trained chuffs) were collected from 6 male bottlenose dolphins at Dolphin Quest, Oahu in 2013. It was observed that the tidal volume of the animals was significantly higher during chuffs. It can also be shown that the voluntary breath takes the shape of an impulse biased towards the positive slope of the impulse shown on the left of Figure 49. Flows for the exhalations were more variable, with a rapid rate of change, a less consistent plateau in the impulse than for inhalations, and a rapid decrease towards the end of a chuff. The duration of the expiratory phase was significantly shorter than the inspiratory phase (Expiratory:  $0.31 \pm 0.04s$ , Inspiratory:  $0.43 \pm 0.05s$ ) [13].

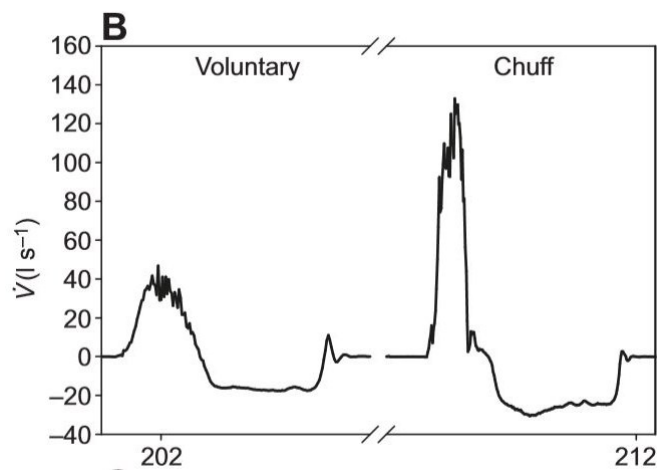


**Figure 49: Flow Rate Trace of Voluntary (left) versus Maximal Respiratory Effort (right)**

[13]

It is difficult to put Figure 49 into context with regard to the pressure data collected in the current study due to the lack of a time scale. For instance, Figure 50 shows an example of raw data collected from ChuffSim @  $\{y/D = 0, z/D = 0, x/D = 0\}$  from the RCN geometry case.

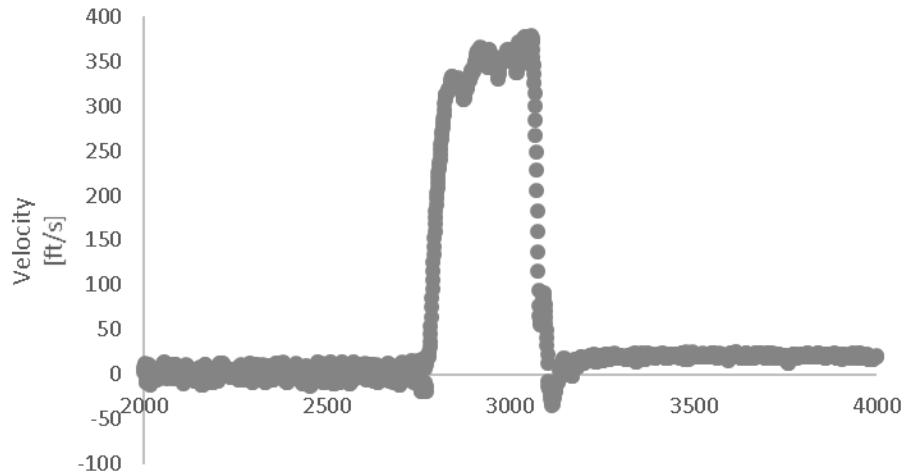


**Figure 50: Example of Velocity Trace from RCN Potential Core**

While it may be known that the x-axis refers to milliseconds in this instance, from previous graphs, the fact still remains that without indicating exact time scales it is very difficult to compare the flow rate data from the 2017 Fahlman study to the current study data. Nonetheless, Figures 51 & 52 show the instantaneous flow rate versus time for the DNPN and RCN respectively at the origin  $\{y/D = 0, z/D = 0\}$  of each nozzle @  $x/D = 0$ . When comparing the two mechanical chuffs to the In-Situ chuff there is a slight bias of the peak flow rates toward the negative slope of each impulse (most noticeable for the RCN). As discussed earlier in this chapter, the DNPN flow rate shows larger perturbations in the freestream flow rate in comparison to the RCN showing the presence of a more turbulent blowfield. Both Figure 51 & 52 show a slight bump at the bottom of each negative slope, this was most likely a consequence of the ChuffSim motion with respect to the transducer.

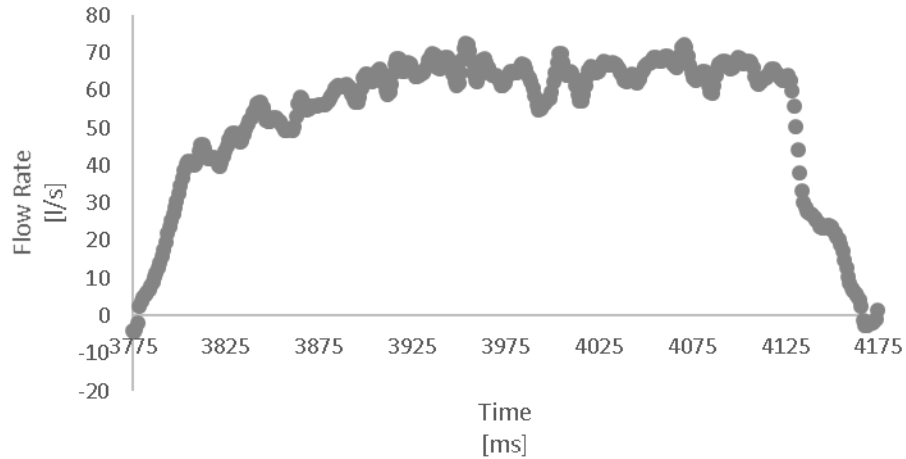


**Figure 51: DNPN Instantaneous Origin Flow Rate versus Time @  $x/D = 0$**

The time duration of these chuffs were 0.40 seconds for the DNPN and 0.35 seconds for the RCN which are similar to the times described in literature (Fahlman et. Al, 2017) 0.26-0.31 seconds. Using efflux times and the averaged flowrates the total volume of fluid expelled (tidal volume) from each nozzle geometry can be calculated. The tidal volume for each nozzle is ~29.4 liters for the RCN and ~15.4 liters for the DNPN showing a total loss fluid of 17.6 and 31.6 liters respectively.

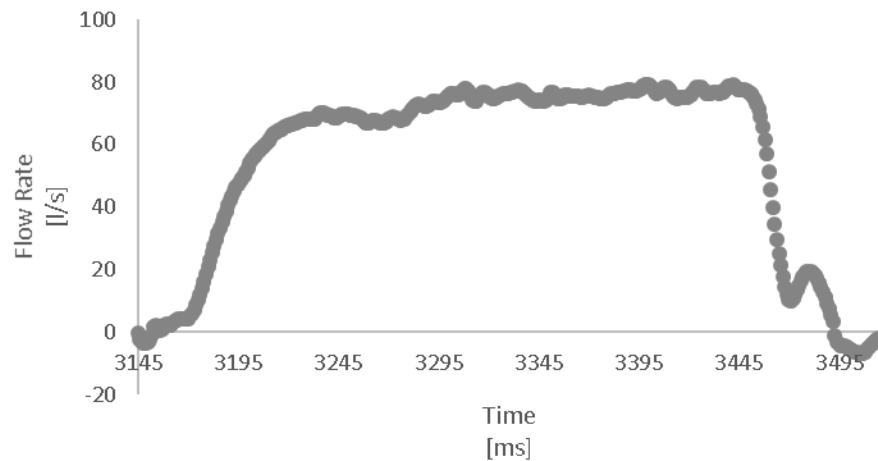


**Figure 52: RCN Instantaneous Origin Flow Rate versus Time @  $x/D = 0$**



This loss of fluid is speculated to be from fluid leakage out of the piston cylinder gap during each mechanical chuff. These volumes expelled are slightly outside the range described in Andreas' study found in Appendix C, Figures C1 and C2 (~9-18 liters).

While the volume of fluid expelled by ChuffSim is greater than the average tidal volume of dolphins in the study it still gives a reasonable analogy of a blowfield and its basic characteristics.

#### *Results from Bermuda In-Situ PIV*

The existing data describes both voluntary breathing and maximal breathing rates for a set of dolphins. The forceful breath described as a chuff is considered to have an efflux time less than one second. More specifically, a chuff happens in less than a tenth of a second which was not previously suggested in any existing dolphin study.

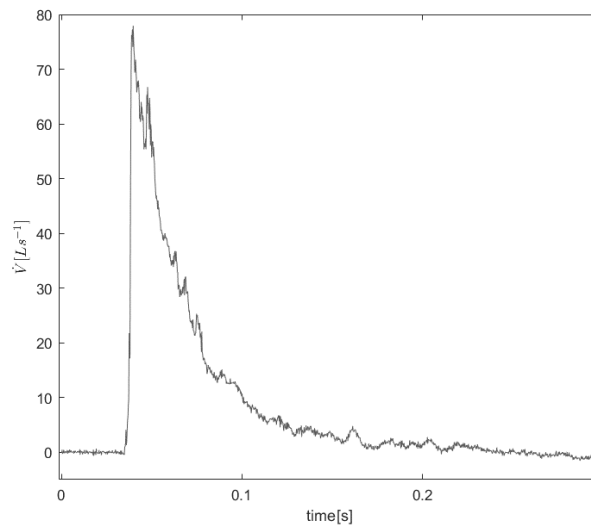


**Figure 53: Bermuda PIV Volumetric Flow Rate Plot [28]**

Figure 53 shows the instantaneous flow rate taken from an In-Situ PIV realization from Bermuda taken at  $x/D = 6.7$  above the blowhole. The dolphin orientation within the field of view is as illustrated in the figure underneath. This plane is analogous to the ChuffSim z-plane that was surveyed during the current study. The image shows the peak flow rate (~80 liters/second) biased towards the positive slope of the impulse showing similarity to a voluntary breath rather than a

chuff; it shows that the chuff happens in ~0.1 seconds which is almost three times less than what is suggested. This can also be supported mathematically by dividing the average tidal volume (~14 liters) from Andreas's study by the hypothesized efflux time (~0.1 seconds) :

$$\text{Maximal Respiratory Effort} = \frac{14 \text{ liters}}{0.1 \text{ second}} = 140 \frac{\text{liters}}{\text{second}}$$

This shows that a flow rate of ~140 liter/second can only be achieved if it occurs in a shorter time than previously described. The tidal volume of the dolphin chuff in Figure 54 can be approximated by roughly taking the area under the curve and multiplying the result by  $\pi$ .

$$\text{Tidal Volume} = 0.5 * \sim 0.1 \text{ seconds} * \sim 78 \frac{\text{liters}}{\text{second}} * \pi = 12.3 \text{ liters}$$

The approximated volume is ~12 liters which is reasonable when comparing it to the Oahu data. Because this flow rate data was taken above the orifice, entrainment of ambient fluid occurs, meaning that this calculated figure (~12 liters) is an over-estimated volume. In addition, this calculation is assuming that a dolphins blowfield is axis-symmetric, which thus far, it has been proven to be non-axis-symmetric. However, for the purpose of approximating the tidal volume it is sufficient.

Figure 54 shows the velocity profiles taken from In-Situ PIV that was performed in Bermuda. The velocity profiles correspond to three different dolphins of different background, gender, and age (Appendix E).

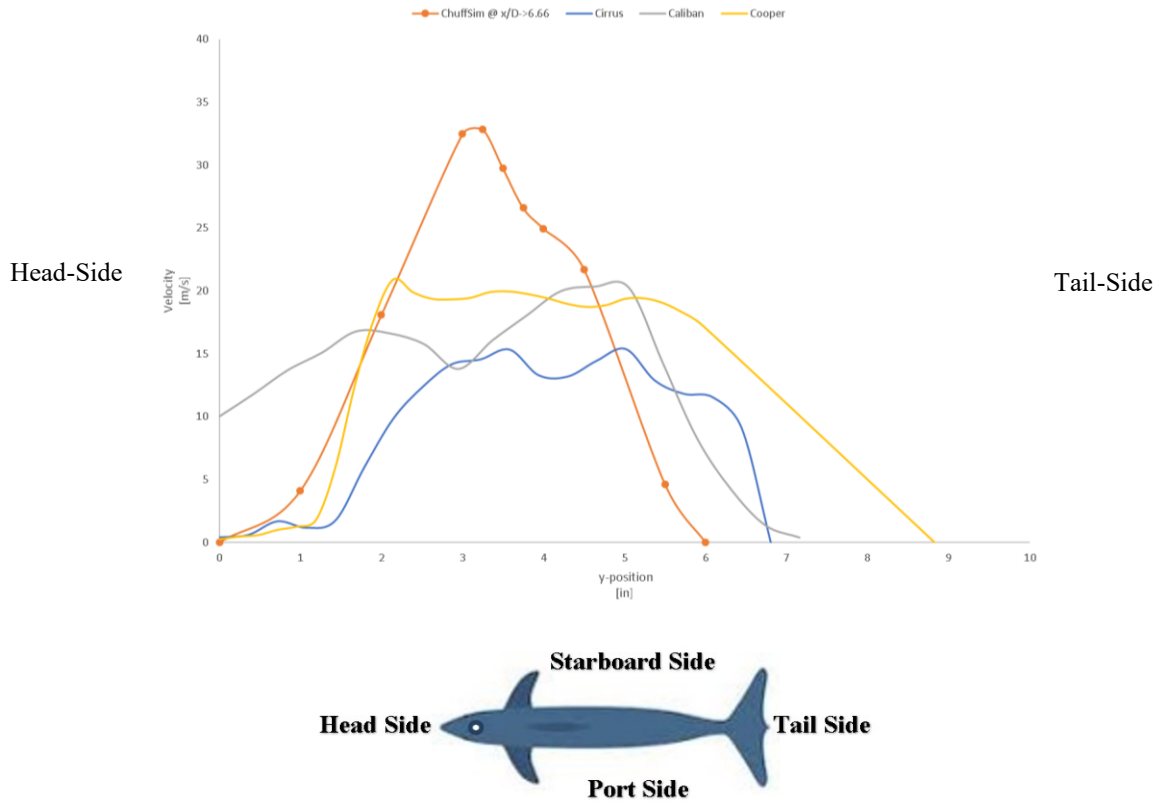


**Figure 54: ChuffSim Averaged Velocity and Bermuda In-Situ PIV Comparison**

An axial distance of  $x/D = 6.7$  was the location the velocity profiles were taken from and compared to the ChuffSim velocity profile. The ChuffSim data represents the averaged transducer velocity taken at  $x/D = 6.7$  above the ChuffSim orifice using the DNPN nozzle geometry. The DNPN velocity profile is shown as more directional than the nature blowfields indicating that their plumes are coherently more mixed than the DNPN. This would make resolving the potential-core of these plumes difficult due to its short length supported back in Figure 33 (velocity decay plot). Another difference that may have affected the DNPN extent was the absence of a blowhole flap which could alter the blowfields spreading rate. All of the velocity profiles follow a similar head-side and tail-side slope but with vastly different peaks. This is most likely because the PIV data from Bermuda was only partially resolved like the ChuffSim PIV data. The DaVis software seemed to hit a threshold of particle velocity it could resolve most

likely from the three-dimensional effects and improper seeding of the blowfield. An interesting take-away from these videos was the clumping nature from large particles of mucus and their behavior within the blowfield. The mucus would clump near the rim of the orifice during the quasi-steady state portion of the chuff while breaking off from the lip. Once the clumps break-off they begin to accelerate up through the jet-extent and outwards from the blowfield. These mucus particles exhibit a viscoelastic nature and have no predictable trajectory due to their random formation in and around the blowhole. The concentration of mucus is observed to be greatest above the blowhole's bifurcation.

The last portion of this study will discuss the benefits of continuing research of blowfields with respect to cross-flows. The head-wise bias of a blowfield may have interesting implications when subjected to a cross-flow. During open ocean swimming the head-side of the dolphin would tentatively be under the cross-flow condition parallel to the  $y/D$  axis (assuming atmospheric conditions are quasi-quiescent). Because of this, the blowfield is operating at an injection angle greater than 90 degrees with respect to the cross-wind illustrated in Figure 55 which could facilitate an increase in axial plume penetration. Counter-rotating vortex pairs (CVPs) occur as a result of jet vorticity modification imposed by the cross-flow where in-plane vortex rings generate close to the exit and travel upward on the leeward side (tail-side). The velocity ratio of the freestream cross-flow to the potential-core velocity is  $\sim 11.1$  assuming the 650 ft/s (velocity from 140 liter/second flow rate through 30 mm orifice) is achieved in the potential core with a 40 mile per hour cross-wind. Horseshoe vortices form in tandem to CVPs as a result of the cross-flow boundary layer that encounters an adverse pressure gradient, similar to trailing vortex formation on airfoils, forming spanwise vortices that move around the jet [24]. The study of (CVP) formation from a dolphin nasal passage will lead to better blowfield penetration predictions during use of a UAS.

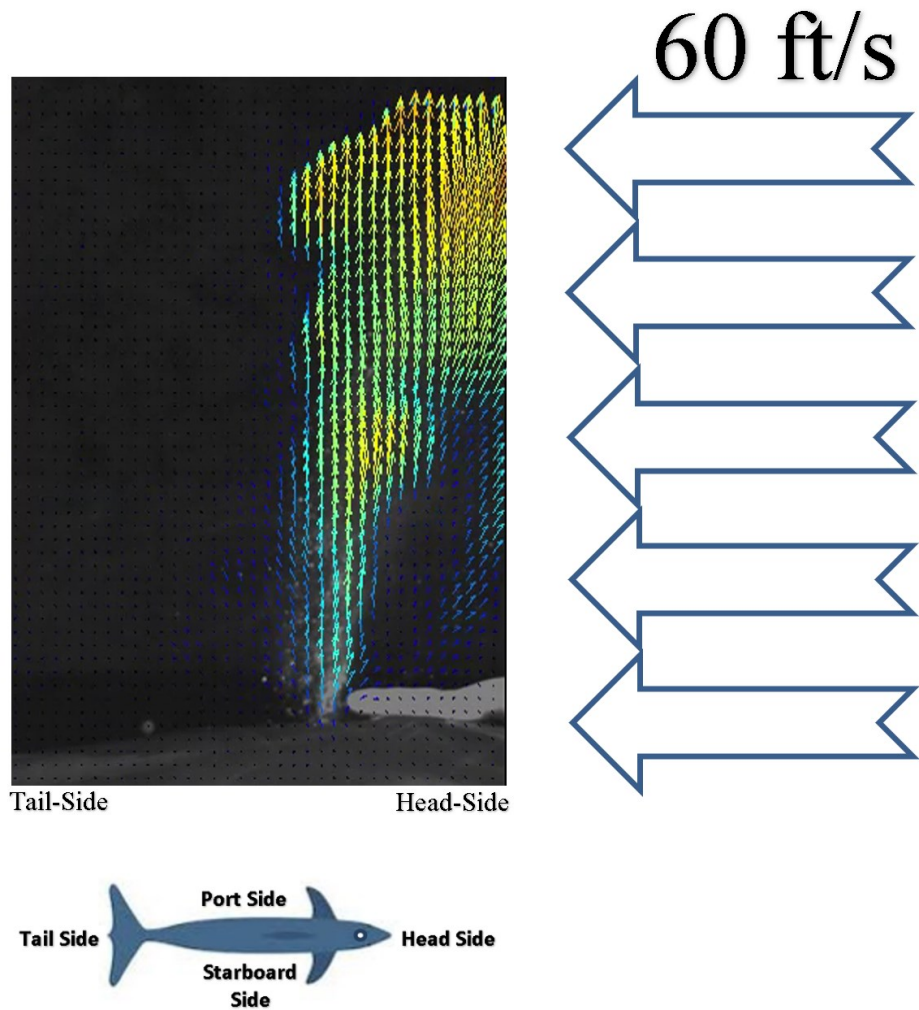


**Figure 55: Cross-Flow Illustration**

*Jet Penetration in Cross Flow*

Understanding the impact a cross-flow has on a jet is crucial for determining chuff location after it is injected into the blowfield. Figure 56 shows a depiction of a static In-Situ chuff impacting a researcher in the face approximately 5 feet from the dolphin's blowhole. The static penetration distance is supported by the blowfield penetration statistics from ChuffSim where the plume generated by the machine is videoed impacting the ceiling at roughly 10 feet above the

blowhole. This is informative, but, not sufficient for designing a UAS that will tentatively operate in the open-ocean.



**Figure 56: Dolphin Chuff Blowing Researcher's Hair [28]**

While no cross-flow analyses were conducted with ChuffSim, the penetration of a chuff was approximated in a cross-flow with the use of Norster's  $Y_{max}$  equation introduced in Chapter 2. In Figure 57,  $Y_{max}/D$  is plotted against the momentum flux ratio for both nozzle geometries for cross-winds ranging from 10 – 40 mph [25].

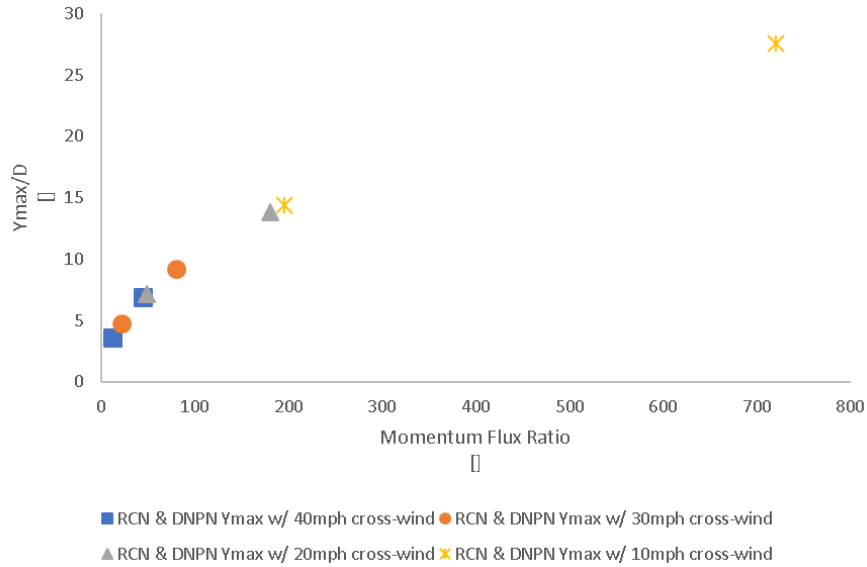


**Figure 57: Ymax/D vs. Momentum Flux Ratio for Jets in a Cross-Flow**

The Ymax/D variable corresponds to the current study's x/D direction not to be confused with the z-plane. Because of the RCN's higher flow rate, its data point in Figure 57 is attributed to the larger Ymax/D point for each cross-flow. The maximum penetration distance is 6.9-27.6D for the RCN and 3.6-14.4D for the DNPV showing greater penetration by the RCN due to its higher velocity blowfield. Because these flowrates achieved in the current study are lower than those presented in previous work the estimated maximum case would achieve a penetration range of 11.4-45.5D for cross-winds varying from 10-40 mph. This is assuming a potential-core velocity of ~650 ft/s, which would give a tentative UAS flight range of 1.1-4.5 feet above the blowhole. The figure shown and the maximum penetration distances discussed above are lower numbers than anticipated. It is very likely that Norster's equation does not apply to the high end of momentum flux ratios described in this section (10-700). This is because the momentum flux ratios that are typically used for combustor dilution holes range from 5-50 making the equation used in this plot inapplicable unless proven otherwise in a laboratory setting.

## CHAPTER V

### CONCLUSION

#### *Answering Research Questions*

In this thesis, a mechanical dolphin exhalation was successfully designed, manufactured, and tested. The ChuffSim simulated a blowfield for two different nozzle geometries: a conventional round nozzle and a dolphin nasal passage nozzle. These two nozzles were analyzed and compared throughout the duration of this study.

The DNPN velocity plots had characteristics of a well-mixed nozzle in comparison to the RCN. This behavior was also supported by the velocity decay plot that illustrated a stark decay for the DNPN contrary to the RCN. The RCN showed that impulsively started conventional round nozzles behave similarly to steady conventional round nozzles which was illustrated on the velocity decay plot where the RCN closely followed the Vonglahn trend line. The RCN and DNPN achieved nominal flowrates of 44.1 & 84.4 liter/s with tidal volumes of 29.4 & 15.4 liters respectively. The calculated RCN tidal volume fell outside the range of tidal volumes tested In-Situ by Fahlman et Al. (2017) where the calculated tidal volume for the DNPN fell within the range presented in text (9-18 liters) [13]. The DNPN showed to have both a head-side and port-side bias induced by the 90 degree bend and the nasal passage streamlines within the nozzle. Neither of these trends were reciprocated by the RCN. This shows the possibility of non-self-similar blowfields in the wild. The DNPN potential core has a higher turbulence level when compared to the RCN due to the DNPN's restrictive passages. The nuances of both blowfields



are witnessed qualitatively in the video footage from each nozzle. Both nozzle geometries showed qualitative aspects similar to their steady jet counterparts where the DNPN achieved a larger spreading rate and the RCN had a more concentrated plume. A maximal respiratory effort is redefined to have an efflux time less than what is suggested in literature ( $\sim 0.1$ s). This specification is important in determining tidal volumes of chuffs and should be better documented in the future. Blowfields were found to penetrate  $3.6\text{-}14.4D$  for the DNPN &  $6.9\text{-}27.6D$  for the RCN when subjected to a range of cross-winds (10-40 mph). Due to the large values on the high end of the momentum flux ratios approximated (10-700) the Norster  $y_{max}$  equation was determined to be inapplicable to the current study.

### *Limitations*

Performing PIV both In-Situ and in the laboratory setting suffered from insufficiently resolved data. Each had its own caveat, from the complicated In-Situ logistics to poor seeding in the laboratory setting, both suffered from large particle displacement in and near the potential core. These in addition to large seeding particles inhibited researchers from tailoring a FOV capable of resolving blowfield footage. In a laboratory setting it is recommended to use a shadowgraphy technique as it has proven to yield robust results when resolving vector flow fields that are innately difficult to seed. In addition to these issues, the machine motion from TDC to BDC would move the nozzles with respect to the origin. This increases the spatial uncertainty for each measurement described during the grid-survey and velocity decay survey of ChuffSim. Efforts to more effectively secure the machine in the future will be necessary for mitigating the error associated with this motion.


### *Future Work & Recommendations*

The future work in this area should consist of studying blowfields subjected to crossflows. In addition to this, a more accurate representation of a dolphin's blowhole should be

implemented to the exit of the DNPN to achieve a more analogous blowfield. A new method of In-Situ blowfield measurements should be practiced in replacement of optical velocimetry due to complicated logistics. The blowfield splatter tests outlined in this study proves to be a promising new method of blowfield measurement and requires less logistics to perform multiple tests. The tests at different planes can provide insights to the evolution of dolphin chuffs that will ultimately lead to a CONOPS design choice.

The current study contains preliminary data to supplement the design of a UAS, however, there are other aspects of the design that need to be investigated further before pursuing a design choice. Among the aspects that need further studying are the type of noise that dolphins are irritated by as well as the shape and size of the craft. Biologists infer that wild dolphins are very easily spooked and need to be approached with caution. Failure in doing so will prove to be counter productive since this projects main goal is to monitor and reduce dolphin stress in the wild. Lastly, the study of multiphase blowfields and determining concentration of mucus in a blowfield will be crucial for designing a UAS capable of capturing chuffs in the wild. This thesis will serve as the qualitative and quantitative genesis of blowfield research and will continue to be applicable to the field of impulsively started turbulent jets.

## REFERENCES

- [1] Abernethy, R. B., Benedict, R. P., & Dowdell, R. B. (1985). *Journal of Fluids Engineering*, 161-164.
- [2] Alexander, A. (2019). Two-Phase Computational Fluid Dynamics Simulations of Dolphin Blowhole Expulsion Jets [1-15].
- [3] Basics of Turbulence. (n.d.). Retrieved July 08, 2020, from <http://web.mit.edu/1.061/www/dream/SEVEN/sevenpage.htm>
- [4] Bitter, R., Mohiuddin, T., & Nawrocki, M. (2006). *LabVIEW: Advanced programming techniques*. Crc Press.
- [5] Bruno Cozzi, S. H. (2017). *Anatomy of Dolphins*. San Diego, USA: Sara Tenney.
- [6] Cassali, G. E., Coghe, A., & Araneo, L. (2001). Near-Field Entrainment in an Impulsively Started Turbulent Gas Jet. *AIAA Journal*, 1113-1122.
- [7] Cater, E. J., & Soria, J. (2002). The evolution of round zero-net-mass-flux jets. *Journal of Fluid Mechanics*, 167-200.
- [8] Çengel, Y. A., & Cimbala, J. M. (2018). *Fluid mechanics: Fundamentals and applications*.
- [9] [@coralworldvi]. (April,3, 2020). "!! Sound on !! Not only do dolphins use their blowholes to breathe air, but they also can make noises from it. In fact, dolphins have no vocal chords at all so every noise a dolphin makes comes right from their blowhole! Watch as Sonny demonstrates a respiration and a vocalization!". Retrieved from <https://www.instagram.com/p/B-7hynIDYIn/?igshid=1xy9gmdeztr6g> .
- [10] Cozzi, B., Huggenberger, S., & Oelschläger, H. H. (2017). *Natural History and Evolution of Dolphins: Short History of Dolphin Anatomy*. Retrieved 7 7, 2020, from <https://sciencedirect.com/science/article/pii/B9780124072299000014>
- [11] Cylinder, M. (2012). *Design Engineering Guide*. Actuant Corp.
- [12] Davitian, J., Megerian, S., Alves, L., & Karagozian, A. R. (2006). Control of Transverse Jet Shear Layer Instabilities. *American Institute of Aeronautics and Astronautics*.
- [13] Fahlman, A., Loring, S. H., Levine, G., Rocho-Levine, J., Austin, T., & Brodsky, M. (2015). Lung mechanics and pulmonary function testing in cetaceans. *The Journal of Experimental Biology*, 2030-2038.

- [14] Fahlman, A., Moore, M. J., & Garcia-Parraga, D. (2017). Respiratory function and mechanics in pinnipeds and cetaceans. *The Company of Biologists*, 1761-1771.
- [15] Glahn, U. H. (1984). On some flow characteristics of conventional and excited jets. *American Institute of Aeronautics and Astronautics*.
- [16] Gupta, J. K., Chen, Q., & Lin, C.-H. (2009). Characterizing exhaled airflow from breathing and talking. *Indoor Air*, 31-39.
- [17] Hassan, S. H., Guo, T., & Vlachos, P. P. (n.d.). Flow field evolution and entrainment in a free surface plunging jet.
- [18] Jabbal, M., Wu, J., & Zhong, S. (2006). The performance of round synthetic jets in quiescent flow. *The Aeronautical Journal*, 385-393.
- [19] Johari, H., Zhang, Q., Rose, M. J., & Bourque, S. M. (1997). Impulsively Started Turbulent Jets. *AIAA Journal*, 657-662.
- [20] Jorgsen, Finn, Ekman. How To Measure Turbulence With Hot-Wire Anemometers. Hotwire2.pdf (2002). <http://web.iitd.ac.in/~pmvs/courses/mel705/hotwire2.pdf>. PDF download.
- [21] Kline, S. J., and F. A. McClintock. "Describing Uncertainties in Single-Sample Experiments." *Mechanical Engineering*, Vol. 75, No. 1, January 1953: 3-8.
- [22] Lefebvre, A. H., & Ballal, D. R. (2010). Gas Turbine Combustion: Alternative Fuels and Emissions 3rd ed. Boca Raton: Taylor & Francis Group, LLC.
- [23] List, E. J. (n.d.). Turbulent Jets and Plumes. *Annual Review of Fluid Mechanics*, 189-212.
- [24] Mahesh, K. (2004). The Interaction of Jets with Crossflow. *The Annual Review of Fluid Mechanics* .
- [25] Margason, R. J. (1993). Fifty Years of Jet in Cross Flow Research. *NASA Ames Research Center*.
- [26] Meg VanSciver, Shelly Miller & Jean Hertzberg (2011) Particle Image Velocimetry of Human Cough, *Aerosol Science and Technology*, 45:3, 415-422, DOI: [10.1080/02786826.2010.542785](https://doi.org/10.1080/02786826.2010.542785)
- [27] Moffat, R. J. (1982). Contributions to the Theory of Single-Sample Uncertainty Analysis. *Journal of Fluids Engineering*, 250-258.
- [28] Ngo, A. (2019). PIV Hotwash [1-15].

- [29] Nishimura H, Sakata S, Kaga A (2013) A New Methodology for Studying Dynamics of Aerosol Particles in Sneeze and Cough Using a Digital High-Vision, High-Speed Video System and Vector Analyses. *PLoS ONE* 8(11): e80244. doi:10.1371/journal.pone.0080244
- [30] Novick, A. S., Arvin, J. R., & Quinn, R. E. (1980). Development of a Gas Turbine Combuster Dilution Zone Design Analysis. *J. Aircraft*, 712-718.
- [31] O'Brien, D, Haley. (2018, July). CT Scan.
- [32] Smith, B. L., & Glezer, A. (1998). The formation and evolution of synthetic jets. *Physics of Fluids*, 2281-2297.
- [33] Smith, S. H., & Mungal, M. G. (1998). Mixing, structure and scaling of the jet in crossflow. *Journal of Fluid Mechanics*, 83-122.
- [34] Stone, James R., and Daniel J. McKinzie Jr. "Acoustic excitation: A promising new means of controlling shear layers." (1984).
- [35] Tang, J. W., Liebner, T. J., Craven, B. A., & Settles, G. S. (2009). A schlieren optical study of the human cough with and without wearing masks for aerosol infection control. *Interface Focus*, 727-734.
- [36] (D.1) Thielicke, W. and Stamhuis, E.J., 2014. PIVlab – Towards User-friendly, Affordable and Accurate Digital Particle Image Velocimetry in MATLAB. *Journal of Open Research Software*, 2(1), p.e30. DOI: <http://doi.org/10.5334/jors.bl>
- [37] Wei J, Li Y (2017) Human Cough as a Two-Stage Jet and Its Role in Particle Transport. *PLoS ONE* 12(1):e0169235.doi:10.1371/journal.pone.0169235.
- [38] Witze, P. O. (1980). The Impulsively Started Incompressible Turbulent Jet.
- [39] Yang, S., Lee, G. W., Chen, C.-M., Wu, C.-C., & Yu, K.-P. (2007). The Size and Concentration of Droplets Generated by Coughing in Human Subjects. *Journal of Aerosol Medicine*, 484-494.
- [40] 8507C\_DS\_082219.pdf (2019). [https://buy.endevco.com/ContentStore/MktgContent/Endevco/Datasheet/8507C\\_DS\\_082219.pdf](https://buy.endevco.com/ContentStore/MktgContent/Endevco/Datasheet/8507C_DS_082219.pdf). PDF download.

## APPENDICES

## APPENDIX A

### A.1 Piezoresistive Transducer Calibration Procedures

Figure A1 shows the Labview interface used to acquire pressure transducer data. Calibration of this pressure transducer (shown in Figure A2) converts the pressure data into velocity data. The data was then saved as a .lvm file in a directory. Each run logged 10 seconds worth of data and wrote the file to a new folder for organization purposes. The DAQ assistant corresponds to a student owned myDAQ device with both analog and digital inputs/outputs.

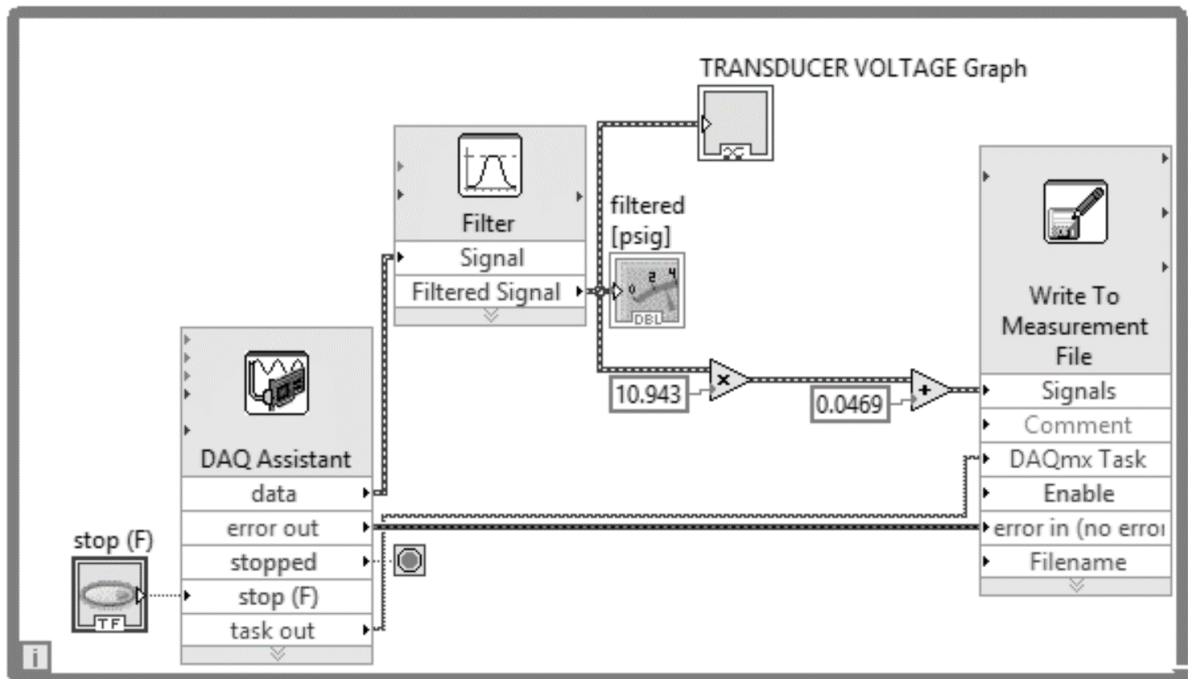
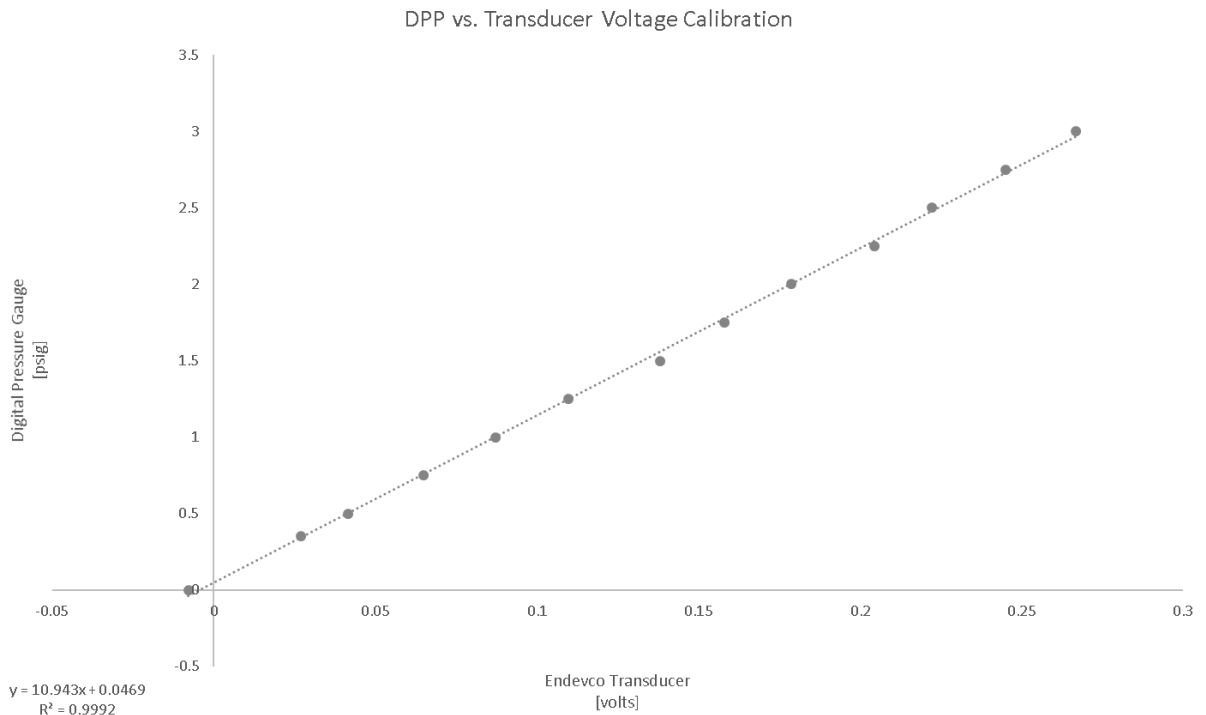


Figure A1: Labview Calibration and Logging Program [4]

The signal obtained from the piezoresistive pressure transducer (Endevco 8507C-5) was run through a Filter Module shown above. The filter selected in this module was a Butterworth Second order low-pass filter to decrease the noise generated by the system during use. These filters typically remove electronic noise from the signal and prevents folding back of the spectra (aliasing). The filter should be as steep as possible for unsteady signals such as the signals processed in the current study. [20]



**Figure A2: Digital Pitot Tube Gauge Pressure vs. Endevco Pressure Transducer Voltage**

The transducer used in the current study is a piezo-resistive pressure transducer with the capability of measuring unsteady flow regimes. This section contains additional information to supplement the calibration process outlined in the Experimental Methods section. The calibration runs for the pitot tube are in units of gauge pressure where the Endevco pressure transducer is in



units of volts. The equation used in the NI Labview program to calibrate and log the voltage signal in terms of gauge pressure is:

$$Gauge\ Pressure = 10.943 * [Transducer\ Voltage] + 0.0469$$

#### **Eqn. A1 Calibration Equation**

The calibration is verified each week to ensure accuracy of the transducer due to the fluctuations of ambient conditions throughout testing. The periodic calibration checks yielded no discernible differences in the equation above, the only changes made during each day of testing was zeroing the scale as consequence of changing atmospheric pressure conditions. The Labview program back panel is shown in Figure A1. The Endevco pressure transducer used a sampling rate of 1 kHz and is capable of sampling gauge pressure from 0-5 psig (datasheet in Appendix A, Figure A3). [40]

## APPENDIX B

### B.1 Unsteady Pressure Transducer Specifications used in the Current Study

This is a section of the manufacturer’s data sheet. Figure B1 shows the physical characteristics of both the four-arm bridge and the external size of the transducer. The four-arm bridge is the manner that electrical voltage is measured in terms of gauge pressure within a system. Appendix A shows the methods that transducer voltage corresponded to gauge pressure for the current study. The general characteristics for the piezo-resistive pressure transducer used in the current study is found underneath the “- 5” column in Figure B2.

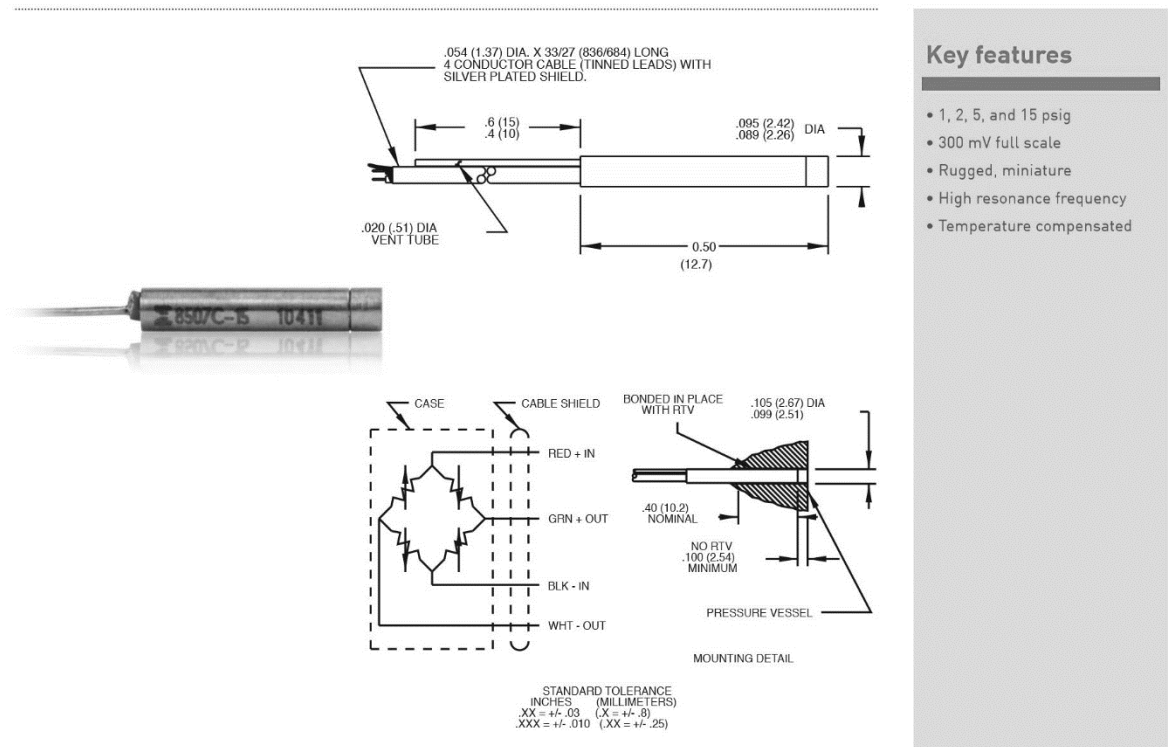


**Figure B1: Endevco Pressure Transducer Size Specification Sheet [40]**

## Specifications

The following performance specifications are referenced at +75°F [+24°C], 100 Hz and 10 Vdc unless otherwise noted. Calibration data, traceable to National Institute of Standards and Technology (NIST), is supplied.

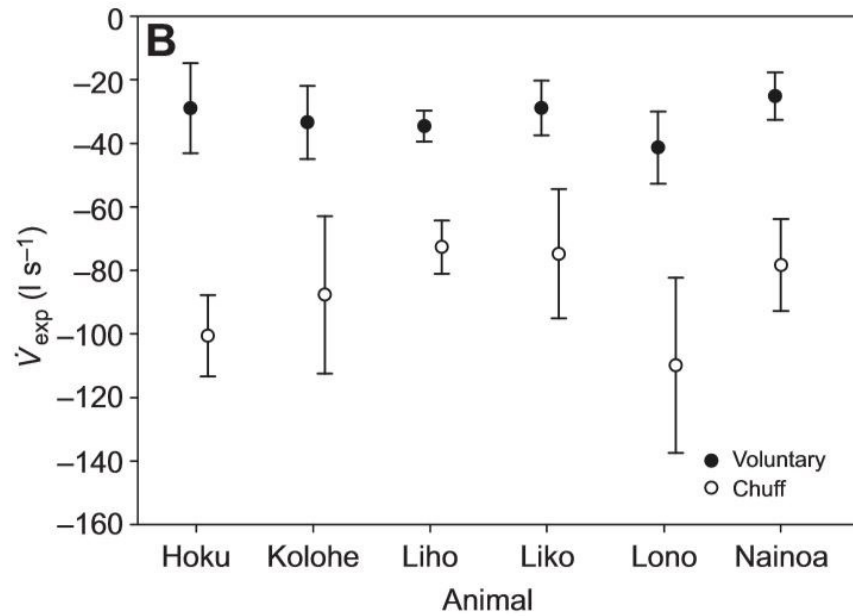
	Units	8507C-1	-2	-5	-15
Range [1]	psig	0-1	0-2	0-5	0-15
Positive sensitivity	mV/psi	200 ±50	100 +50/-20	60 ±20	20 ±7
Combined: Non-linearity, Non-repeatability,					
Pressure hysteresis	% FSO RSS max	1.5	1.5	0.75	0.50
Non-linearity, independent	% FSO typ	1.0	1.0	0.50	0.20
Non-repeatability	% FSO typ	0.1	0.1	0.1	0.05
Pressure hysteresis	% FSO typ	0.1	0.1	0.1	0.1
Zero measurand output	mV max	±10	±10	±10	±10
Zero shift after 3x range	±% 3x FSO max	0.2	0.2	0.2	0.2
Thermal zero shift					
From 0°F to 200°F [-18°C to +93°C]	±% FSO max	3	3	3	3
Thermal sensitivity shift					
From 0°F to 200°F [-18°C to +93°C]	±% max	4	4	4	4
Resonance frequency	Hz typ	55,000	70 000	85 000	130 000
Non-linearity at 3x range	% 3x FSO	2.5	2.5	2.0	1.0
Photoflash response	Equiv. psi	0.01	0.01	0.03	0.1
Warm-up time	ms	1	1	1	1
Acceleration sensitivity	Equiv. psi/g	0.0002	0.0002	0.0002	0.0002
Burst pressure (diaphragm/reference side)	psi	20/20	40/40	100/50	150/50
<b>Electrical</b>					
Supply voltage	10.0 Vdc recommended, 18 Vdc maximum				
Electrical configuration	Active four-arm piezoresistive bridge				
Resistance					
Input	2000 ±800 ohms				
Output	1500 ±600 ohms				
Isolation	100 megohms minimum at 50 volts; leads to case, leads to shield, shield to case				
Noise	5 microvolts rms typical, dc to 50 000 Hz; 50 microvolts rms maximum, dc to 50 000 Hz				
<b>Mechanical</b>					
Case, material	Nickel - iron alloy				
Cable, integral	Four conductor No. 36 AWG Teflon® insulated leads, braided shield, PVC jacket				
Dead volume (+) port	0.00005 cubic inches (0.0008 cc)				
Mounting	Bond into #38 drill hole [2.6 mm] using an RTV such as DOW CORNING Silastic® 738; [RTV not permitted within 0.10 inch [2.5 mm] of unit's face.]				
Weight	0.3 gram [cable weighs 3.6 grams/meter]				
<b>Environmental</b>					
Media	Internal seals are epoxy and are compatible with clean dry gas media. Media in (+) measurand port is exposed to nickel-iron alloy, silicon, ceramic, Parylene C, and epoxy. Media in (-) measurand port is exposed to the above and RTV silicone coating.				
Temperature	-65°F to +225°F [-54°C to +107°C]				
Vibration	1000 g pk				
Acceleration	1000 g				
Shock	10 000g, 100 microsecond haversine pulse				
Humidity	Isolation resistance greater than 100 megohms at 50 volts when tested per MIL-STD-202E, Method 103B, Test condition B.				

**Figure B2: Endevco Pressure Transducer General Specification Sheet [40]**

## APPENDIX C

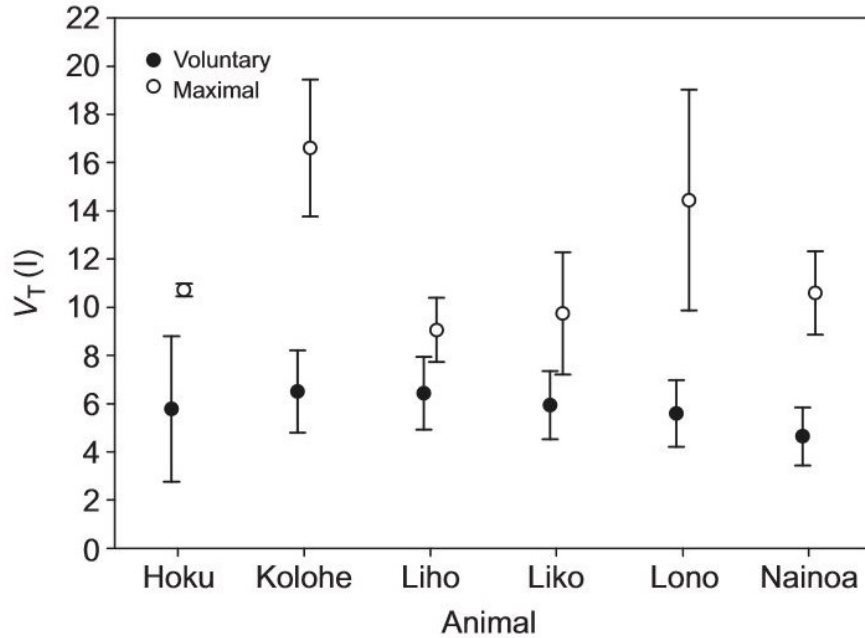
### C.1 Existing Dolphin Flow Rate Data

The flow rates and tidal volumes for both maximal and voluntary breaths, obtained during the Fahlman study (2015), are displayed in Figures C1 & C2. Figure C1 displays each Dolphin Quest Oahu dolphin with their subsequent flow rate data with uncertainty bars.



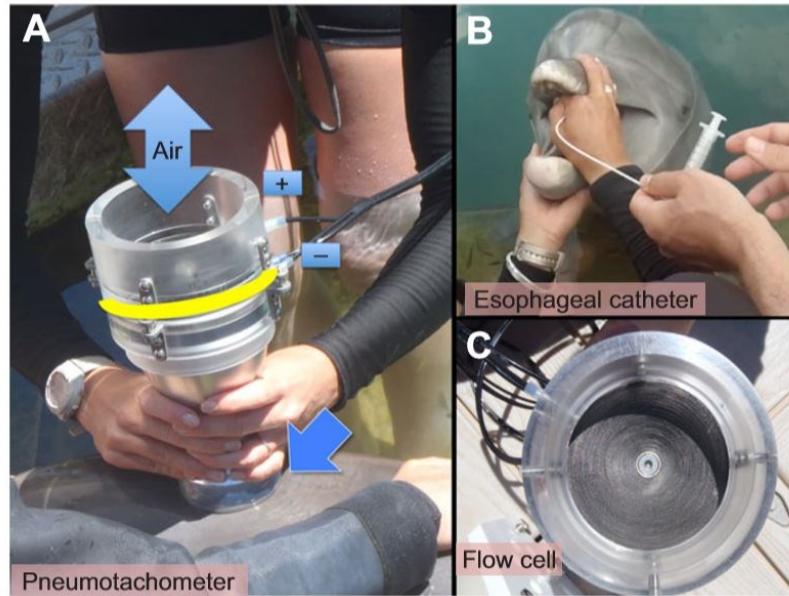
**Figure C1: Voluntary & Forceful Exhalation Flow Rates [14]**

Figure C2 shows the tidal volumes with uncertainty bars for each animal willing to participate in the study. The “chuff” data is considered the maximal/forceful effort while the voluntary is considered the baseline respiratory effort.



**Figure C2: Tidal Volume of Voluntary & Maximal Respiratory Efforts [14]**

Figure C3-a displays the pneumotachometer and how it was used in relation to the animals in order to obtain the data found in Figures C1 & C2. The bidirectional arrow shows where the air exits the device. The darker blue arrow in the bottom of the image points to where a silicone ring seals the interface between the device and the dolphin to mitigate leakage. The “+” & “-“ signs show each of the differential pressure transducer connections. Figure C3-b shows the insertion of esophageal catheter (this data was not applicable to the current study). Figure C3-c illustrates the Merriam flow cell used in the customized pneumotachometer. This flow cell measures deflection in terms of voltage similar to the method used in the current study but on a much larger scale.



**Figure C3: Pneumotachometer Apparatus and Test Set-up [14]**

## APPENDIX D

### D.1 Measurement of FOV (field of view) for Flow Visualization

PIVlab is an opensource application for MATLAB designed to perform Digital Particle Image Velocimetry (DPIV) for quantitatively mapping flows. One particular function, the measuring tool, was used from this program to digitally measure the FOV of hand chosen frames. These hand chosen frames were taken the instant before a plume hit the ceiling (illustrated in Figure D1). This data was used in Figure 48 that outlined the jet diameter evolution axially downstream from the RCN and DNP.



Figure D1: MATLAB PIVlab Measure Tool [36]

## APPENDIX E

### E.1 Additional Dolphin Info from Current Study

Figure E1 displays Dolphin Quest Bermuda dolphin specs willing to participate in the current study. Cooper, Caliban, and Cirrus all participated in the In-Situ blowhole PIV sessions giving unprecedented information of blowfield characteristics both quantitatively and qualitatively.

## Dolphins Information

Cooper	Caliban	Cirrus
<ul style="list-style-type: none"><li>• <i>Tursiops truncates</i> (common bottosenose dolphin)</li></ul>	<ul style="list-style-type: none"><li>• <i>Tursiops truncates</i> (common bottlenose dolphin)</li></ul>	<ul style="list-style-type: none"><li>• <i>Tursiops truncates</i> (common bottlenose dolphin)</li></ul>
<ul style="list-style-type: none"><li>• Age – 9</li></ul>	<ul style="list-style-type: none"><li>• Age – 26</li></ul>	<ul style="list-style-type: none"><li>• Age – 45</li></ul>
<ul style="list-style-type: none"><li>• Born in human care</li></ul>	<ul style="list-style-type: none"><li>• Born in the human care</li></ul>	<ul style="list-style-type: none"><li>• Born in the wild</li></ul>
<ul style="list-style-type: none"><li>• Male</li></ul>	<ul style="list-style-type: none"><li>• Female</li></ul>	<ul style="list-style-type: none"><li>• Female</li></ul>
<ul style="list-style-type: none"><li>• Father is Nimbus</li></ul>	<ul style="list-style-type: none"><li>• 9ft long</li></ul>	<ul style="list-style-type: none"><li>• Former Navy</li></ul>
<ul style="list-style-type: none"><li>• Mother is Caliban</li></ul>		<ul style="list-style-type: none"><li>• Likes long swims along the beach</li></ul>

**Figure E1: General Bermudian Dolphin Information [25]**



## APPENDIX F

### F.1 Uncertainty in Piezo-Resistive Pressure Transducer Measurements

Variable	Expanded Uncertainty for 95% Confidence Interval	Units []
DNPV & RCN Distance Measurements	0.25 ± 0.004	[in]
DNPV Velocity	180 ± 5.0	[ft/s]
RCN Velocity	351 ± 10.0	[ft/s]
DNPV Flow Rate	39 ± 4.0	[liters/s]
RCN Flow Rate	75 ± 4.0	[liters/s]

**Table F1: Expanded Uncertainties for 95% Confidence Intervals**

#### Uncertainty in Velocity Calculation

In the current study, calculating velocity from measured gauge pressure requires calculating both Mach number and temperature from isentropic relations (equation 7a, 7b, and 7c).

$$\pm F = \left[ \left( \frac{dF}{dx_1} \right)^2 (\varepsilon_1)^2 + \left( \frac{dF}{dx_2} \right)^2 (\varepsilon_2)^2 \right]^{1/2}$$

#### **Eqn. F1 Standard Uncertainty [21]**

Using equation F1 outlined by Kline and McClintock (1953), uncertainty for the velocity calculation is quantified assuming a worst-case 2 percent transducer standard error for the largest delta pressure (~1.25 psig) measured in the RCN blowfield. More specifically this standard error is represented in the Mathematica code below as ± 0.07 psig because the full-scale calibration spanned from 0-3.5 psig over the transducer 300 mV scale. The max velocities taken from the

DNPN and RCN data are displayed respectively with the standard uncertainties  $180 \pm 5$  ft/s &  $351 \pm 10$  ft/s. Figure F1 illustrates the calculation on the next page:

```

In[329]:= Clear["Global`*"]

In[330]:=
   $\gamma = 1.4;$ 
   $t_{not} = 530; (* \text{ degree R } *)$ 
   $r_{air} = 1716; (* \frac{\text{ft lbf}}{\text{R slug}} *)$ 
   $p = 14.7; (* \text{ psi } *)$ 
   $p_{not} = \delta p + p;$ 

In[335]:=
  
$$\text{mach}[\delta p_] := \sqrt{\left(\frac{2}{\gamma - 1}\right) \left(\left(\frac{p_{not}}{p}\right)^{\frac{\gamma - 1}{\gamma}} - 1\right)};$$

  
$$\text{temp}[\delta p_] := \frac{t_{not}}{1 + \left(\frac{\gamma - 1}{2}\right) \text{mach}[\delta p]^2};$$

  
$$\text{vel}[\delta p_] := \sqrt{(\gamma * r_{air} * \text{temp}[\delta p])} \text{mach}[\delta p];$$


In[338]:=
   $dvdp = D[\text{vel}[\delta p], \delta p];$ 
   $dvdp // \text{Simplify}$ 

Out[339]=
  
$$\frac{5916.46}{(14.7 + \delta p)^{0.714286} \sqrt{-1 + 0.46396 (14.7 + \delta p)^{0.285714}} \left(8.62143 + 1. (14.7 + \delta p)^{0.285714}\right)^{3/2}}$$


In[340]:=  $\delta p = 1.25; (* \text{ delta pressure from transducer } *);$ 

In[341]:=
   $v = \text{vel}[\delta p]; (* \text{ ft/s } *)$ 
   $v // N$ 

Out[341]= 386.635

In[342]:=
   $\epsilon v = 0.07; (* \text{ psig } *)$ 
   $dvdpeval = dvdp /. \delta p \rightarrow 1.25;$ 
   $\text{velunc} = \sqrt{dvdpeval^2 * \epsilon v^2}; (* \text{ ft/s } *)$ 
   $\text{velunc} // N$ 

Out[343]= 10.4681

In[344]:= (* percent error with 2 percent transducer standard error *)

  
$$\frac{\text{velunc}}{v} * 100$$


Out[344]= 2.70748

```

**Figure F1: Mathematica Code for Uncertainty in Velocity Calculation**

### Uncertainty in Measured Distances Across Nozzle Orifice

When distances were used in equation 8, from the experimental methods section, for flowrate calculation the smallest increment of measurement would attribute to the largest portion of distance measurement uncertainty. Dial calipers are used to measure distances across each the DNPN and RCN orifice. The smallest increment of measurement was  $0.25 \pm 0.002$  in, for a confidence of interval of 95% the expanded uncertainty would be  $0.25 \pm 0.004$  in while the relative standard uncertainty is 0.008.

### Uncertainty in Flow Rate Calculation

Calculating flowrate utilizes equation 1 (a, b and c) which is a function of distance and velocity. Uncertainty in the flow rate calculation uses both the distance and velocity uncertainties in measurement shown in the Mathematica code in Figure F2. The same methodology from equation f1 was utilized to quantify the uncertainty. The standard uncertainties in flow rates for both the DNPN and RCN are  $39 \pm 2$  liters/second and  $75 \pm 2$  liters/second respectively. In order to get the total expanded uncertainty for a 95% confidence interval the standard uncertainties must be multiplied by 2 giving  $39 \pm 4$  liters/second and  $75 \pm 4$  liters/second for the DNPN and RCN respectively. Both the DNPN and RCN have approximately the same standard uncertainty and expanded uncertainty due to the distance uncertainty holding the weight in this calculation.

```

In[647]:= (* flow rate uncertainty *)
In[648]:= edist = .002/12; (* convert to feet from inches *)
          ac[d_] :=  $\frac{\pi}{4} d^2$ ;
          vdot[umean_, d_] := umean ac[d];
In[652]:= dvdotdd = D[vdot[umean, d], d];
          dvdotdd // Simplify
Out[653]=  $\frac{d \pi \text{ umean}}{2}$ 
In[654]:= dvdotdu = D[vdot[umean, d], umean];
          dvdotdu // Simplify
Out[655]=  $\frac{d^2 \pi}{4}$ 
In[656]:= d1 =  $\frac{1.18}{12}$ ; (* diameter of orifice in feet for both RCN and DNPN *)
          RCN = 351; (* RCN average velocity across orifice in ft/s *)
          DNPN = 180; (* DNPN average velocity across orifice in ft/s *)
          vdotunc =  $\sqrt{(\text{dvdotdd} * \text{edist})^2 + (\text{dvdotdu} * \text{velunc})^2}$  /. d -> d1;
          (* uncertainty in terms of umean *)
          vdotunc // Simplify
Out[659]=  $\sqrt{0.00632 + 6.62733 \times 10^{-10} \text{ umean}^2}$ 
          RCNunc = vdotunc /. umean -> RCN;
          RCNunc * 28.3 // N (* RCN flowrate uncertainty in  $\frac{\text{liters}}{\text{s}}$  *)
Out[661]= 2.26429
          DPNunc = vdotunc /. umean -> DNPN;
          DPNunc * 28.3 // N (* DNPN flowrate uncertainty in  $\frac{\text{liters}}{\text{s}}$  *)
Out[663]= 2.25363
          RCNvdot = vdot[351, d1] * 28.3 // N (*  $\frac{\text{liters}}{\text{s}}$  *)
Out[664]= 75.4371
          DPNvdot = vdot[180, d1] * 28.3 // N (*  $\frac{\text{liters}}{\text{s}}$  *)
Out[665]= 38.6857

```

**Figure F2: Mathematica Code for Uncertainty in Flow Rate Calculation**

## **F.2 Piezo-Resistive Pressure Transducer Uncertainty in Calibration Method**

Quantifying the uncertainty due to the calibration process, outlined in Experimental Methods section, starts with quantifying the possible sources of error. The standard errors for: the analog

pressure gauge, digital pressure gauge, and piezo-resistive pressure transducer are 3%, 1%, and 2% (worst case) respectively. The pressure transducer worst case standard uncertainty was outlined by the factory calibration sheet but specified the standard uncertainty could vary from 0.1-2 percent full scale [40]. Using these values, the total uncertainty in the calibration is calculated and shown in Figure F3. The total standard error is 3.7% while the total expanded uncertainty is ~7.5 % for a 95% confidence interval.

```

In[742]:= (* Uncertainty in Calibration Process *)
In[743]:= uanalog = 0.03; (* analog pressure gauge standard uncertainty in percentage *)
          udigital = 0.01; (* digital pressure gauge standard uncertainty *)
          utransducer = 0.02; (* pressure transducer worst case standard uncertainty *)
In[746]:=
          utotcalib =  $\sqrt{uanalog^2 + udigital^2 + utransducer^2}$ ;
          utotcalib * 100 // N(* total standard calibration uncertainty *)
Out[747]= 3.74166
In[748]:= utotcalib * 100 * 2 // N(* total expanded uncertainty for a 95% confidence interval *)
Out[748]= 7.48331

```

**Figure F3: Mathematica Code for Uncertainty in Calibration**

VITA

CJ Barton

Candidate for the Degree of

Master of Science

Thesis: CHARACTERIZATION OF THE IMPULSIVE JET PRODUCED  
FROM A DOLPHIN'S BLOWHOLE

Major Field: Mechanical and Aerospace Engineering

Biographical:

Education:

Completed the requirements for the Master of Science in Mechanical and Aerospace Engineering at Oklahoma State University, Stillwater, Oklahoma in December, 2020.

Completed the requirements for the Bachelor of Science in Mechanical Engineering at the University of Tulsa, Tulsa, Oklahoma in 2018.

Experience:

Unmanned Systems Research Institute (USRI)-OSU, Research Engineer;  
Dolphin Research;  
Bermuda Summer 2018-2019 Acquired acoustic data with marine biologists to drive a UAV design a UAV design for sampling Dolphin saliva to determine stress levels in the wild. Research included thesis work that involved taking PIV measurements of a Dolphin's blowhole. Kaman KMAX Helicopter Wake-Vortex Research; Stillwater, OK Spring 2019 Scale model of an intermeshed helicopter drivetrain was designed to study the rotor's wake pattern using Particle Image Velocimetry methods. Findings were published to AIAA SciTech forum. Engine Dyno/Propulsion Lab Research Assistant;  
Summer 2018 Implemented knowledge of vibration isolation for dynamometer refinement and increased accuracy of measurements. Used computational software for two-stroke engines to generate expected power output of engines tested.